ADVANCED STEEL CONSTRUCTION

An International Journal

Volume 3 Number 1

March 2007

CONTENTS

Technical Papers

ADVANCED STEEL CONSTRUCTION

an International Journal

ISSN 1816-112X

Volume 3 Number 1

March 2007

Editors-in-Chief

S.L. Chan, *The Hong Kong Polytechnic University, Hong Kong*

W.F. Chen, *University of Hawaii at Manoa, USA*

R. Zandonini, *Trento University, Italy*

Cover: Full scale test for a pre-tensioned truss system under wind pressure. Courtesy of RED Consultant Limited

General Information
Advanced Steel Construction, an international journal

Aims and scope

The International Journal of Advanced Steel Construction provides a platform for the publication and rapid dissemination of original and up-to-date research and technological developments in steel construction, design and analysis.   Scope of research papers published in this journal includes but is not limited to theoretical and experimental research on elements, assemblages, systems, material, design philosophy and codification, standards, fabrication, projects of innovative nature and computer techniques.   The journal is specifically tailored to channel the exchange of technological know-how between researchers and practitioners.   Contributions from all aspects related to the recent developments of advanced steel construction are welcome.

Instructions to authors

Submission of the manuscript.   Authors may submit three double-spaced hard copies of manuscripts together with an electronic copy on a diskette or cd-rom in an editable format (MS Word is preferred).   Manuscripts should be submitted to the regional editors as follows for arrangement of review.

Asian Pacific , African and organizing editor :	Professor S.L. Chan
American editor :	Professor W.F. Chen
European editor :	Professor R. Zandonini

All manuscripts submitted to the journal are highly recommended to accompany with a list of four potential reviewers suggested by the author(s).   This list should include the complete name, address, telephone and fax numbers, email address, and at least five keywords that identify the expertise of each reviewer.   This scheme will improve the process of review.

Style of manuscript

General.   Author(s) should provide full postal and email addresses and fax number for correspondence.   The manuscript including abstract, keywords, references, figures and tables should be in English with pages numbered and typed with double line spacing on single side of A4 or letter-sized paper.   The front page of the article should contain:

  a)   a short title (reflecting the content of the paper);
  b)   all the name(s) and postal and email addresses of author(s) specifying the author to whom correspondence and proofs should be sent;
  c)   an abstract of 100-200 words; and
  d)   5 to 8 keywords.

The paper must contain an introduction and a conclusion.   The length of paper should not exceed 25 journal pages (approximately 15,000 words equivalents).

Tables and figures.   Tables and figures including photographs should be typed, numbered consecutively in Arabic numerals and with short titles.   They should be referred in the text as Figure 1, Table 2, etc.   Originally drawn figures and photographs should be provided in a form suitable for photographic reproduction and reduction in the journal.

Mathematical expressions and units.   The Systeme Internationale (SI) should be followed whenever possible.   The numbers identifying the displayed mathematical expression should be referred to in the text as Eq. (1), Eq. (2).

References.   References to published literature should be referred in the text, in the order of citation with Arabic numerals, by the last name(s) of the author(s) (e.g. Zandonini and Zanon [3]) or if more than three authors (e.g. Zandonini et al. [4]).   References should be in English with occasional allowance of 1-2 exceptional references in local languages and reflect the current state-of-technology. Journal titles should be abbreviated in the style of the Word List of Scientific Periodicals. References should be cited in the following style [1, 2, 3].

Journal: [1] Chen, W.F. and Kishi, N., "Semi-rigid Steel Beam-to-column Connections, Data Base and Modelling", Journal of Structural Engineering, ASCE, 1989, Vol. 115, No. 1, pp. 105-119.

Book: [2] Chan, S.L. and Chui, P.P.T., "Non-linear Static and Cyclic Analysis of Semi-rigid Steel Frames", Elsevier Science, 2000.

Proceedings: [3] Zandonini, R. and Zanon, P., "Experimental Analysis of Steel Beams with Semi-rigid Joints", Proceedings of International Conference on Advances in Steel Structures, Hong Kong, 1996, Vol. 1, pp. 356-364.

Proofs. Proof will be sent to the corresponding author to correct any typesetting errors.   Alternations to the original manuscript at this stage will not be accepted.   Proofs should be returned within 48 hours of receipt by Express Mail, Fax or Email.

Copyright. Submission of an article to "Advanced Steel Construction" implies that it presents the original and unpublished work, and not under consideration for publication nor published elsewhere.   On acceptance of a manuscript submitted, the copyright thereof is transferred to the publisher by the Transfer of Copyright Agreement and upon the acceptance of publication for the papers, the corresponding author must sign the form for Transfer of Copyright.

Permission. Quoting from this journal is granted provided that the customary acknowledgement is given to the source.

Page charge and Reprints. There will be no page charges if the length of paper is within the limit of 25 journal pages. A total of 30 free offprints will be supplied free of charge to the corresponding author.   Purchasing orders for additional offprints can be made on order forms which will be sent to the authors.   These instructions can be obtained at the Hong Kong Institute of Steel Construction, Journal website: http://www.hkisc.org

The International Journal of Advanced Steel Construction is published quarterly by non-profit making learnt society, The Hong Kong Institute of Steel Construction, c/o Department of Civil & Structural Engineering, The Hong Kong Polytechnic University, Hung Hom, Kowloon, Hong Kong.

VOLUME 3   NUMBER 1   **MARCH 2007**

Technical Papers

EFFECTS OF GEOMETRIC PARAMETERS ON MEAN WIND PRESSURE ON GABLE ROOFS OF LOW-RISE BUILDINGS

Y. Quan[1,*], Y. Tamura[2] and M. Matsui[3]

[1] COE Researcher, Department of Architecture, Tokyo Polytechnic University, Japan
*(Corresponding author: E-mail: quanyong@arch.t-kougei.ac.jp)
[2] Professor, Department of Architecture, Tokyo Polytechnic University, Japan
[3] Associate Professor, Department of Architecture, Tokyo Polytechnic University, Japan

ABSTRACT: A series of pressure measurement wind tunnel tests were carried out on low-rise buildings in a simulated suburban wind field. The effects of roof pitch, height/breadth ratio and depth/breadth ratio of gable-roofed low-rise buildings on mean wind pressure coefficients on their roofs for winds parallel or perpendicular to the ridges were discussed. Two new equations of mean wind pressure coefficients, which may be useful for design purpose, were fitted with the test data for various building shapes and the errors of those equations were analyzed carefully. The calculated results with the equations were compared with present wind tunnel test data and literature in detail.

Keywords: low-rise building, gable roof, wind load, wind pressure, wind tunnel test, fitted equation

1.   INTRODUCTION

The majority of structural damage in windstorms has been incurred by low-rise buildings, especially family dwellings that were non-engineered and lacking in maintenance (Homes [1]). For example, Typhoon No. 19 in 1991 (Typhoon 9119) caused severe damage to low-rise buildings over almost all of Japan. The insurance payout for losses caused by this typhoon reached 567.5 billion yen, which at that time was the largest in the world for losses caused by a natural disaster. According to a damage investigation, most wind damage to low-rise buildings was restricted to their envelopes, and in particular to the roof sheathing. This indicates that improvement in the wind resistance to building envelopes can result in a significant reduction in overall economic losses (Uematsu [2]).

Over the last twenty years, a lot of research has been carried out on wind loads on low-rise buildings with gable roofs. Stathopolous [3] and Stathopolous, Surry and Davenport [4] carried out an exhaustive parametric study on wind pressure that led to North American codification. The work by Holmes [5] and other studies reported by Holmes [6] provided the basis for the Australian codification. The studies of Kamei & Maruta [7], Ueda, Tamura and Fujii [8] and Maruta et al. [9] improved the Japanese standard [10]. With the appearance of more and more wind tunnel test data and full-scale measurement data, load standards have been continually revised. In order to make them easy to use for engineers, load standards often provide a simple calculating method that can yield wind loads in most practical cases. However, the calculated results given by such simple calculating methods are often not very precise. For example, most standards offer a single mean wind pressure coefficient for the whole windward gable roof of a building for wind flowing across the roof ridge, where in fact the mean wind pressure coefficient varies with location. The values near the eaves are often much larger than those at other locations, as shown in Figure 4.

In order to make a wind-load database of low-rise buildings, a series of wind pressure measurement wind tunnel tests have been carried out on low-rise buildings in the Atmospheric Boundary Wind Tunnel in the Tokyo Polytechnic University. Contours of average, maximum, minimum and RMS values of the wind pressure coefficients on the roof and walls of such buildings have then been

drawn using this wind tunnel test data, which were disclosed on the website of the Wind Engineering Research Center, Tokyo Polytechnic University (http://www.wind.arch.t-kougei.ac.jp/info_center/weic.html). Based on those test data, the present study attempts to obtain relatively simple and precise equations of mean wind pressure coefficients on gable roofs of low-rise buildings with different geometric parameters.

2. PRESSURE MEASUREMENT WIND TUNNEL TESTS

Pressure measurement wind tunnel tests on low-rise buildings were executed in the Boundary Layer Wind Tunnel, 2.2m wide by 1.8m high, in the Tokyo Polytechnic University, Japan. The length scale, velocity scale and time scale are 1/50, 1/5 and 1/10, respectively.

2.1 Wind Field

Since a lot of low-rise buildings are located in suburban areas, the suburban terrain corresponding to terrain categories III in AIJ [10] is chose as the tested wind field. It is simulated with turbulence generating spires, roughness elements and a carpet arranged on the upstream floor of the test section. The exponent of the mean wind profiles of this simulated wind field is 0.20 and the turbulence intensity at the mean height of the roofs of most test models, about 150mm, is about 0.24. The simulated result is shown in Figure 1.
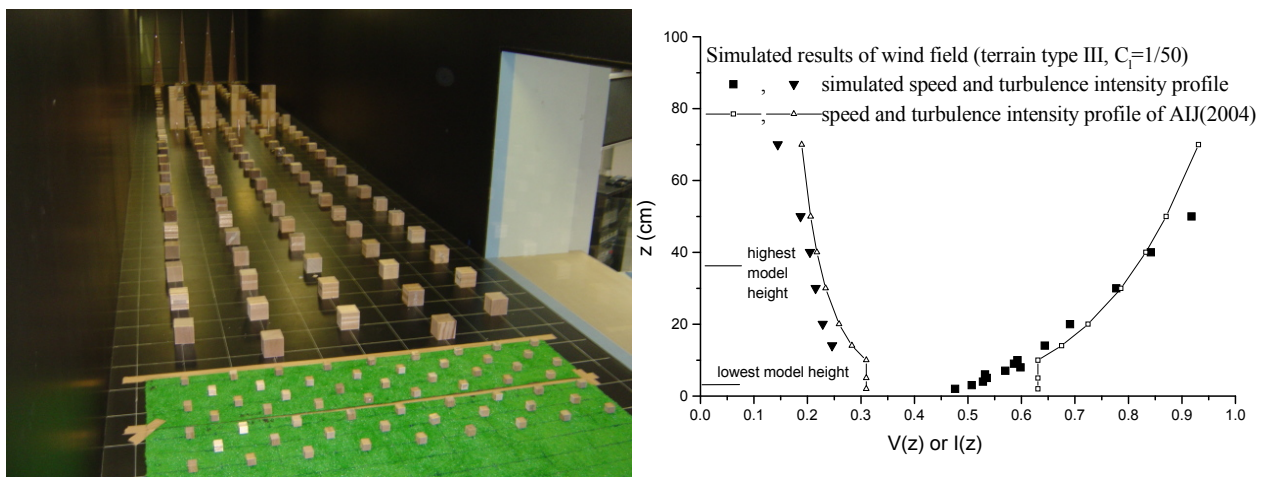
Figure 1. Simulated Wind Field

2.2 Testing Models

Figure 2 shows the test model of a gable house. H, B and D are height, breadth and depth, respectively. β is roof pitch. θ is wind direction angle. When θ is zero degree, the wind flows along the roof ridge. In order to study the effects of the roof pitch, height/breadth ratio and depth/breadth ratio on wind pressure coefficients on the gable roof, 30 models of gable-roofed low-rise buildings with roof pitch of $0^o\sim45^o$, heights/breadth ratio of 3/8~18/8 and depth/breadth ratio of 1~4, as shown in Table 1, were tested. The range of tested wind direction angles was $0^o\sim90^o$ in increments of 15°.
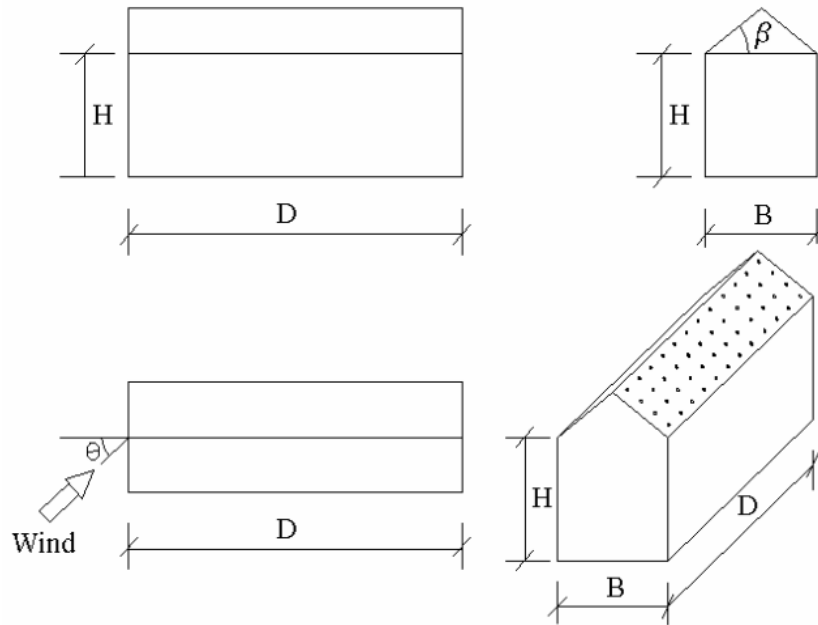
Figure 2. Test Model

Table 1. Parameters of Test Models of Gable-roofed Buildings (Length Unit: cm)

No.	B	D	H	$\beta(^o)$
1~6	16	24	6,12,18,24,30,36	26.7
7~12	16	16,32,40,48,56,64	12	26.7
13~18	16	24	12	45,30,21.8,18.4,4.8,0
19~21	16	24	3.2,6.4,16	45
22~24	16	24	3.2,64,16	26.7
25~27	16	24	3.2,64,16	18.4
28~30	16	24	3.2,64,16	4.8

2.3   Wind Pressure Measurement System

Pressure taps were arranged on the roofs of the testing models at intervals of 20mm. All taps were connected to a pressure measurement scanner by tubes with a length of 1.2m and an inner diameter of 0.8mm. The scanner could measure wind pressures on 384 points simultaneously. Wind pressures on all pressure taps were measured simultaneously with a sampling frequency of 800Hz corresponding to 80hz in full scale and a sampling time of 60 seconds corresponding to 10min in full scale. Each test case was sampled 10 times. The test data were low-pass filtered at 300hz.

2.4   Test Data Process

The transfer function of the tube system as shown in Figure 3 is identified with frequency sweep method. The effect of the tube system on the measured wind pressure was eliminated by dividing the transfer function from the power spectra of the measured raw test data series. Before calculating the statistical values of the wind pressure, the test data were moving averaged every 80 points to make the duration of the peak and RMS value 1s in full scale.
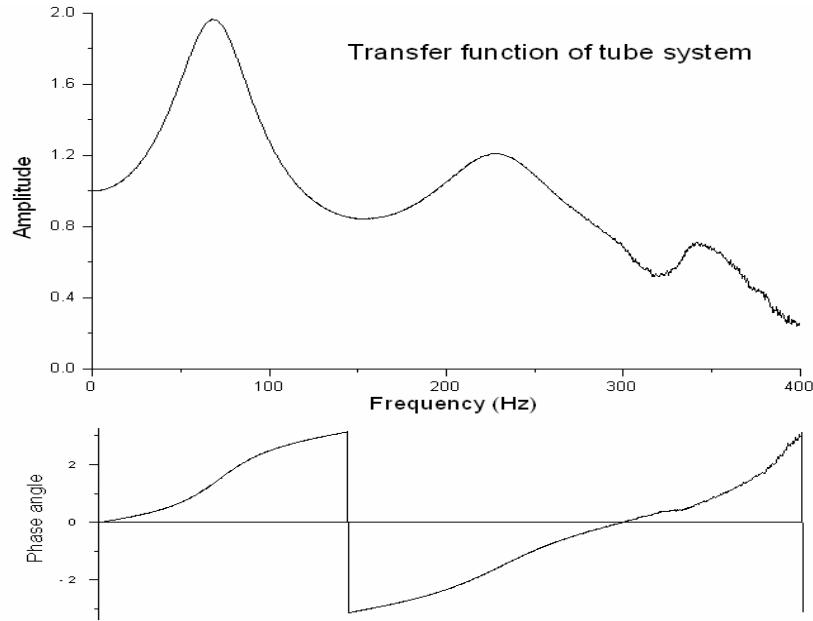
Figure 3. Transfer Function of Tube System

The statistical values of the wind pressures coefficients were the average of the statistical values of the 10 samples. They were calculated from the following equations:

$$\overline{C}_p = \overline{p} / p_{H0} \tag{1}$$

$$\widehat{C}_p = \widehat{p} / p_{H0} \tag{2}$$

$$\breve{C}_p = \breve{p} / p_{H0} \tag{3}$$

$$C'_p = p' / p_{H0} \tag{4}$$

where p is local pressure; p_{H0} is the reference pressure of the approach wind at the average roof height, $H0 = H + \tan \beta.B / 2$.

3.   CONTOURS OF WIND PRESSURE COEFFICIENTS ON ROOF AND WALLS OF LOW-RISE BUILDINGS

Based on the wind tunnel test data, contours of mean, maximum, minimum and RMS values of wind pressure coefficients on the roof and walls, calculated with Equation (1~4), were drawn as shown in Figure 4. Most of the contours are disclosed on the website mentioned on context.

Figure 4 shows two of the contours. It can be seen that, although there are some differences among the wind pressure coefficients at different locations, the mean pressure coefficients near the ridge for wind parallel to the ridge and those on the center-line of the roof for wind perpendicular to the ridge represent approximately the wind pressure coefficients on the whole roof.
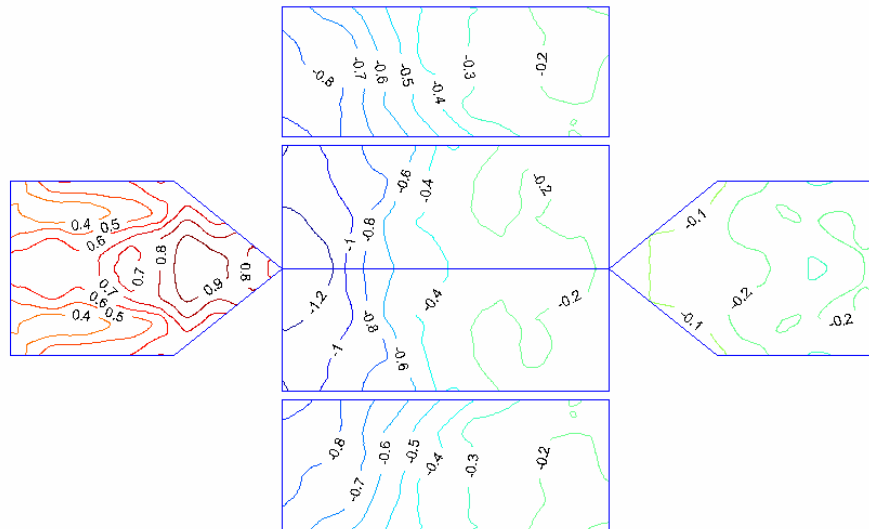
Average Wind Pressure Coefficients of Model Case 13
Height=120mm,Breadth=160mm,Depth=240mm,Roof Pitch=45°,Wind Direction Angle=0°
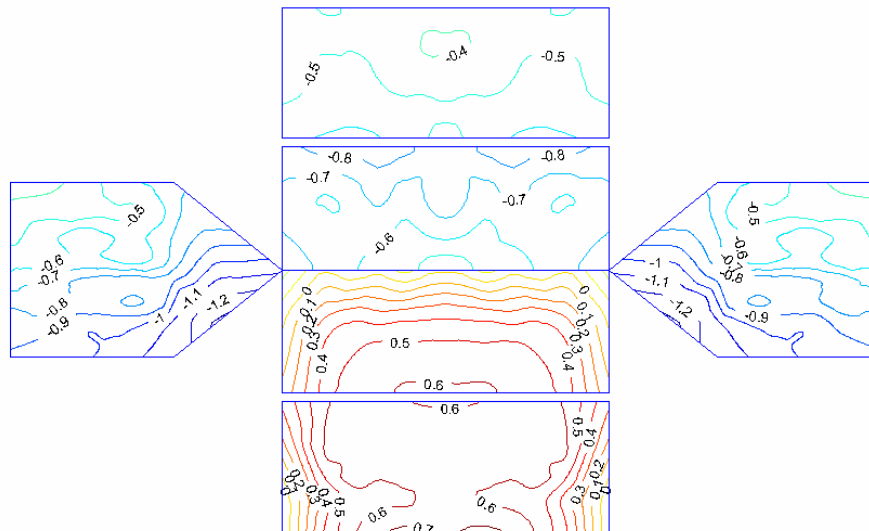
Average Wind Pressure Coefficients of Model Case 13
Height=120mm,Breadth=160mm,Depth=240mm,Roof Pitch=45°,Wind Direction Angle=90°

Figure 4. Contours of Mean Wind Pressure Coefficients on Roof and Wall of Low-rise Buildings

The following paragraphs focus on the mean wind pressure coefficients on gable roofs for wind parallel or perpendicular to the ridge.

4.   COMPARISION WITH TEST RESULTS IN LITERATURE

In order to verify the validity of present test data, the values of $\overline{C}_p$ on the centerline of several gable roofs with wind direction angles of 90° gotten from present wind tunnel tests are chosen to compare with those shown in Holmes' book [1] and Meecham's paper [11] shown in Figure 5.
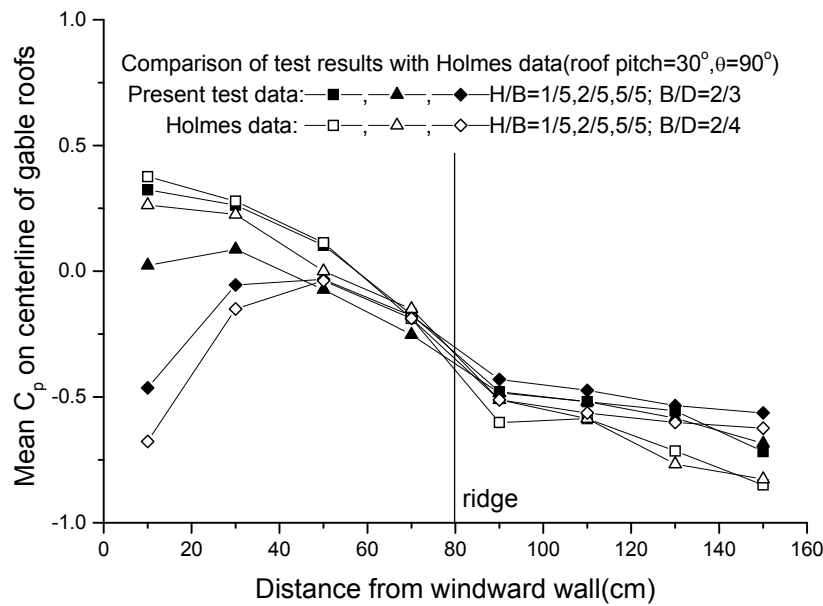
(1)
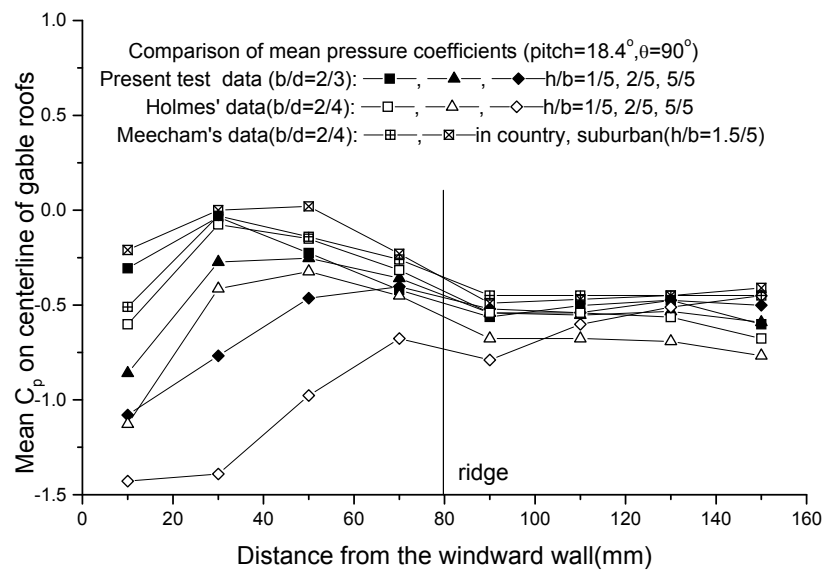
(2)

Figure 5. Comparison of Wind Pressure Coefficients on Gable Roofs

In Figure 5, the trend of the mean wind pressure coefficients obtained from different wind tunnel tests is similar, while there are some differences between the present test data and those of Holmes, especially for the model with a height/breadth ratio of 5/5 and a roof pitch of 18.4, as shown in Figure 5 (2). These differences should be induced by the differences between the test models and wind fields in these two wind tunnel tests. The breadth/depth ratio of Holmes' testing model was 2/4 while the present one is 2/3. The test data of Meecham are a little different from the present ones, since the breadth/depth ratio of Meecham's testing model was 2/4 and the height/breadth ratio was 1.5/5, which is not exactly the same absolutely as the present ones. Furthermore, the turbulence intensities at mid-height of the gable roofs in Meecham's test were 0.14 and 0.18, respectively, while that of the present one is about 0.25.

5.   MEAN WIND PRESSURE COEFFICIENTS FOR WIND PARALLEL OR PERPENDICULAR TO ROOF RIDGES

The temporal mean wind pressure coefficients, $\overline{C}_p$, at each test points on the roofs are calculated from present wind tunnel test data.   Effects of roof pitch, building height and building depth on these mean wind pressure coefficients are analyzed in the following paragraph.

5.1   When Wind Direction Angle is 90°

Figure 6 shows $\overline{C}_p$ on the gable roof for different roof pitches, β. $\overline{C}_p$ on the windward roof increases with increasing β. $\overline{C}_p$ near the windward eave is about -1.5 for $\beta \le 4.8^o$ and increases with increasing β. When β is larger than 30°, positive values of $\overline{C}_p$ begin to appear on the windward roof. When $\beta = 45^o$, $\overline{C}_p$ near the windward eave is $+0.6$. On the leeward roof, $\overline{C}_p$ is $-0.7\sim-0.3$ and decreases with increasing roof pitch, while those near the ridge are around -0.6 and are hardly affected by the roof pitch.
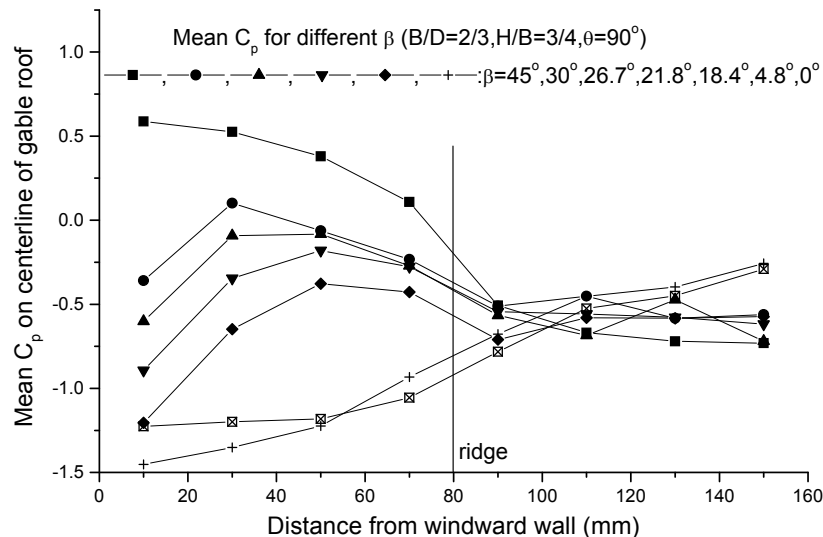
Figure 6. $\overline{C}_p$ on Gable Roofs for Different Roof Pitches When Wind Flows Across Roof Ridge

More test results show that for a wind direction angle of 90°, $\overline{C}_p$ on the windward gable roof with a roof pitch larger than 18.4^o can be considered as linear functions of roof pitch.

Figure 7 shows $\overline{C}_p$ for different model heights. For $\beta = 26.7^o$, $\overline{C}_p$ on the windward roof are mostly negative for $H/B = 3/8 \sim 18/8$ and the suction pressure coefficient increases with increasing height/breadth ratio. This is surprising. With increasing height/breadth ratio, it becomes difficult for the flow to make a detour across the gable roof. More and more flow should make a detour around the sidewalls. This should make the suction pressure coefficients on the windward roof small. However, the present test results show the opposite effect. The test results in Holmes' book showed the same trend.
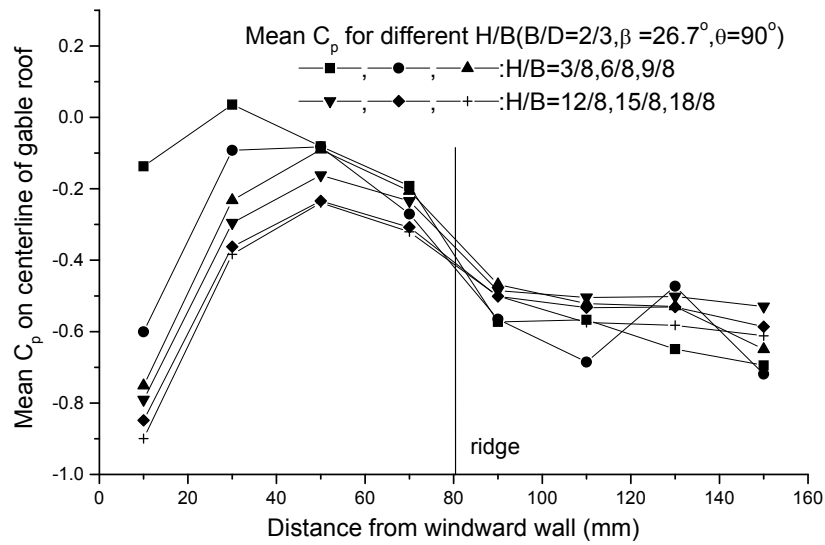
Figure 7. $\overline{C}_p$ on Gable Roofs for Different Building Heights
When Wind Flows Across Roof Ridge
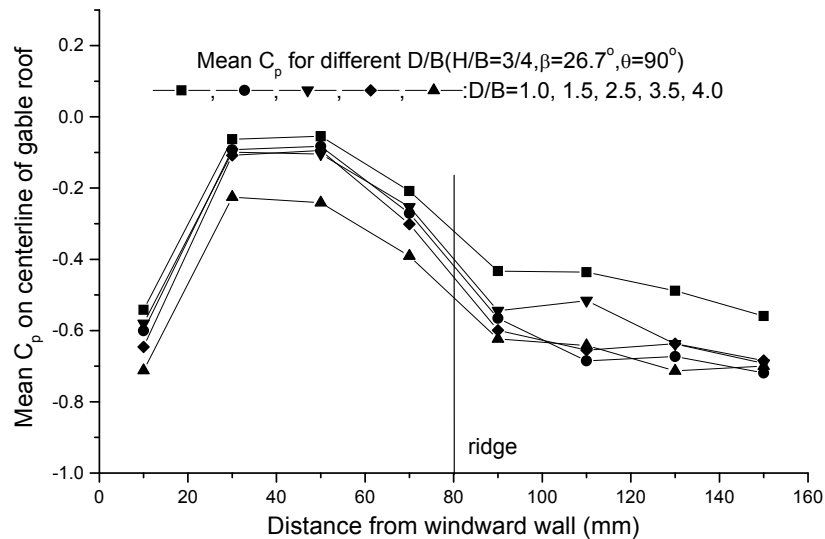
Figure 8. $\overline{C}_p$ on Gable Roofs for Different Building Depths When Wind Flows Across Roof Ridge

More test data indicate that $\overline{C}_p$ near the leeward eave of the steep gable roof increase slightly with increasing model height and those near the ridge show no obvious trend. However, for the gable roof with a roof pitch of 4.8° and the flat roof, $\overline{C}_p$ on the whole roof decrease with increasing model height except those near the windward eave, which are fixed at about −1.2 regardless of the model height.

Figure 8 shows $\overline{C}_p$ on the gable roof for different depth/breadth ratios when the wind direction angle is 90°. As shown, with increasing depth/breadth ratio, $\overline{C}_p$ on the whole roof decreases. With increasing depth/breadth ratio, it becomes difficult for the flow to make a detour around the sidewalls and more and more flow should make a detour across the gable roof. This makes the suction pressure coefficients on the roof large. The present test results confirmed this conclusion.

5.2   When Wind Direction Angle is 0°

When the wind direction angle is 0°, $\overline{C}_p$ on the whole roof is negative and increases with increasing distance from the measured point to the windward gable wall. When this distance reaches the house breadth, $\overline{C}_p$ become fixed at about -0.15 and do not increase any more.

Figures 9~11 show $\overline{C}_p$ for different roof pitches, building heights and building depths for a wind direction angle of 0°. It can be seen that the roof pitch, height/breadth ratio and depth/breadth ratio have little effect on $\overline{C}_p$ when wind flows along the roof ridge.

5.2.1   Fitted equations of mean wind pressure coefficient

Based on the test data of mean wind pressure coefficients on the gable roof, following equations are fitted.
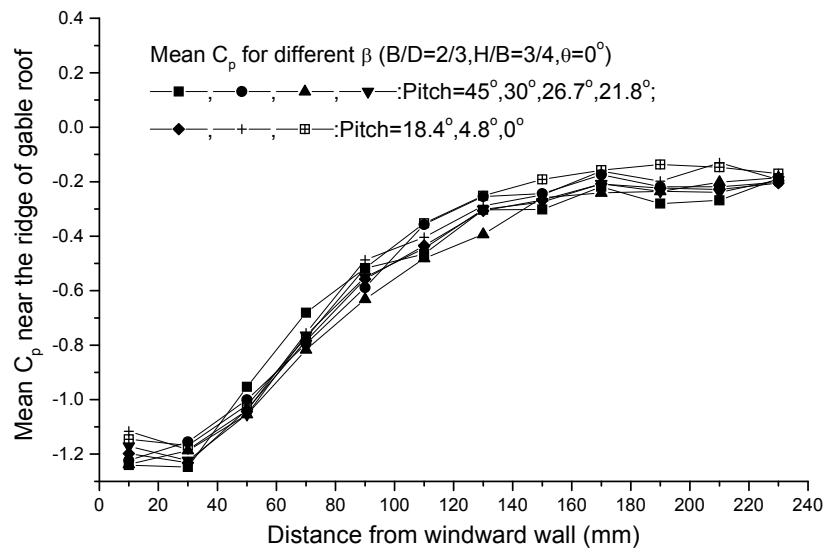
Figure 9. $\overline{C}_p$ on Gable Roofs for Different Roof Pitches When Wind Flows Along Roof Ridge
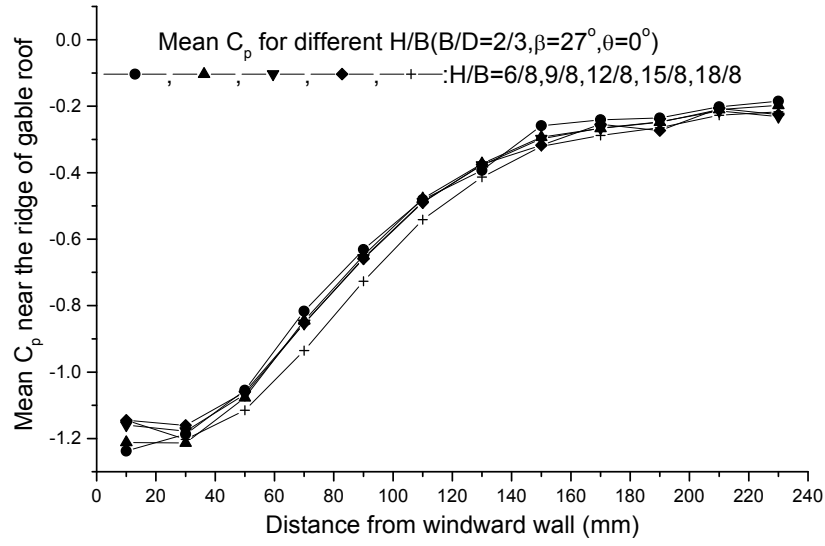
Figure 10. $\overline{C}_p$ on Gable Roofs for Different Building Heights
When Wind Flows Along Roof Ridge
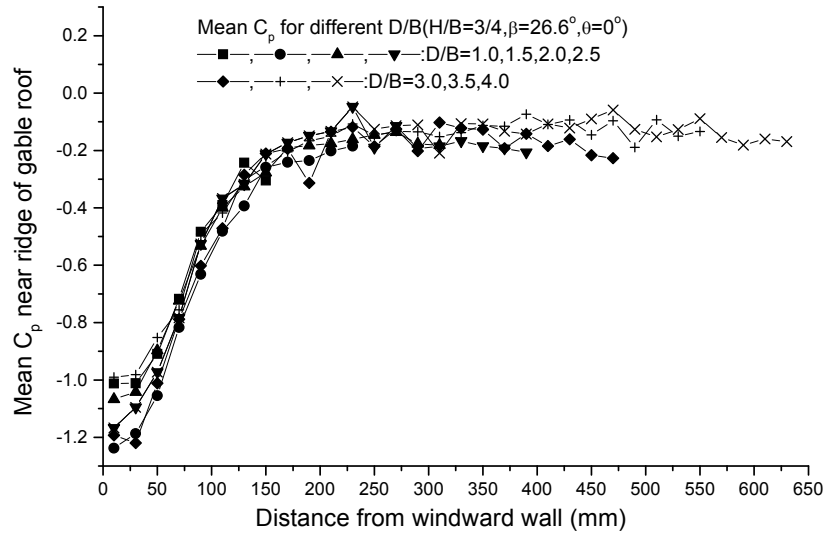
Figure 11. $\overline{C}_p$ on Gable Roofs for Different Building Depths When Wind Flows Along Roof Ridge

When the wind direction angle is 90°, $\overline{C}_p$ on a roof with pitches of 18.4°~45° can be calculated by the following fitted equation:

$$\overline{C}_p = \begin{cases} \psi_1 + \psi_2 (b_1 / B) + \psi_3 (b_1 / B)^2 + 0.1 - 0.05(D/B) & \textit{for windward roof} \\ -0.3 - 0.3(b/B) - 0.04(D/B) & \textit{for leeward roof} \end{cases}$$

$$\psi_1 = (3.56 - 0.094\beta)(-1.23 + 0.3(B/H))$$

$$\psi_2 = (8.45 + 0.4\beta - 0.00127\beta^2)(0.58 + 0.12(B/H) - 0.066(B/H)^2)$$

$$\psi_3 = (2.4 - 1.03\beta + 0.02\beta^2)(0.82 + 0.3(B/H) - 0.125(B/H)^2)$$

(5)

in which, b is the distance from the measured point to the windward sidewall.

When the wind direction angle is 0°, the value of $\overline{C}_p$ on the roof can be calculated by the following approximate equation:

$$\overline{C}_p = \begin{cases} -1.2 + 1.05(d/B) & \text{if } d/B < 1 \\ -0.15 & \text{if } d/B \geq 1 \end{cases} \tag{6}$$

in which d is the distance from the measured point to the windward gable wall.

Compared with the testing data, the mean and maximum error of Equation (5&6) are about 0.05 and 0.24, respectively. The 95% confidence intervals of the calculated results with Equation (5&6) are ± 0.2 as shown in Figure 12.
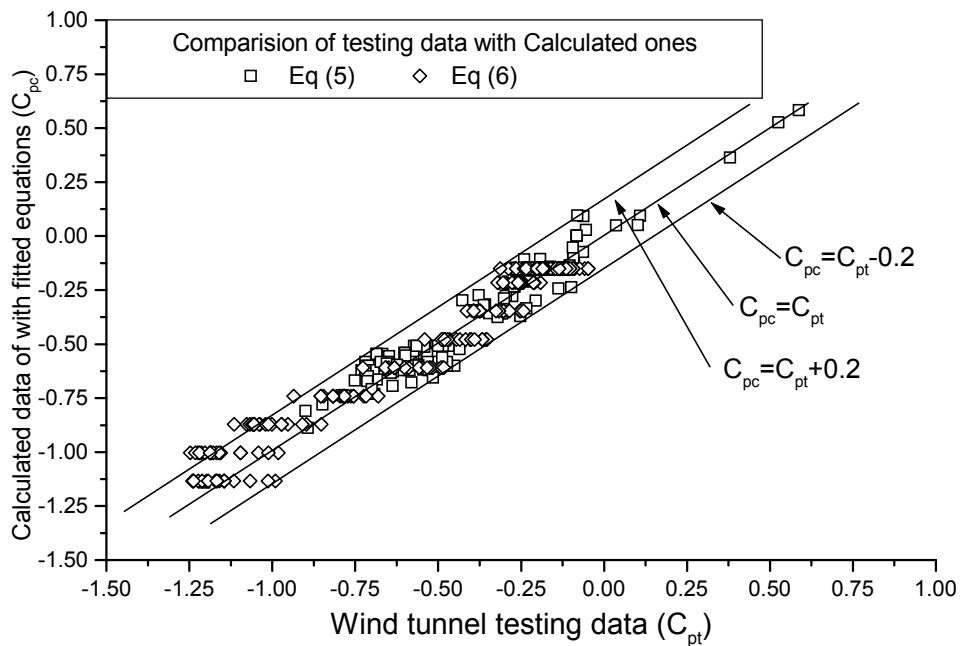
Figure 12. Analysis of Errors of Equation (5&6)

Figures 13~16 compare data obtained from Equation (5&6), present test data and data calculated from AIJ Recommendations for Loads on Buildings [10].

In Figure 13, for roof pitches large than 18.4°, the three sets of data, present test data, calculated ones with Equation (5) and calculated ones basing on AIJ [10], show little difference. Only for roof pitches less than 4.8°, the wind suction pressure coefficients on the windward roof calculated from AIJ [10] are smaller than the present test data.
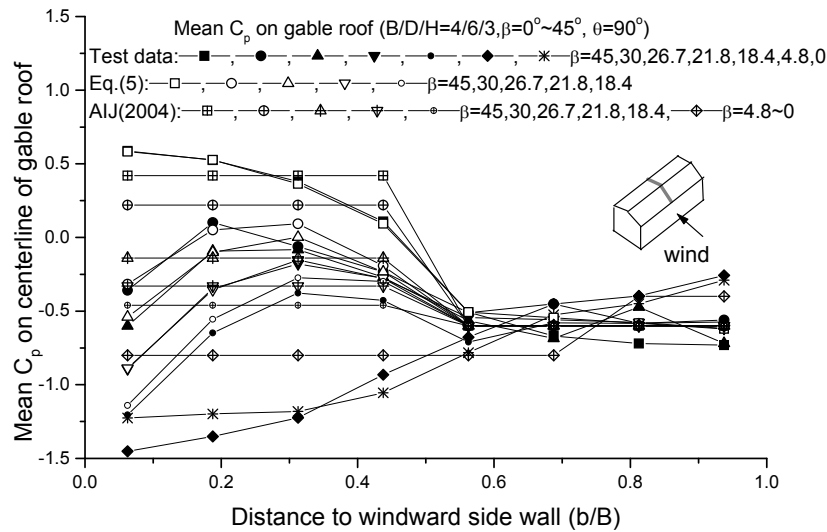
Figure 13. Comparison of Equation (5) with Test Results and Literature for Different Roof Pitch
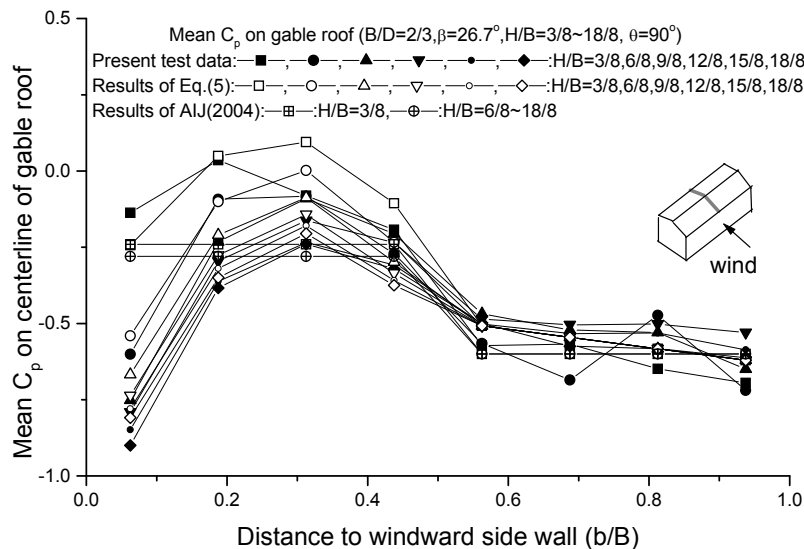
Figure 14. Comparison of Equation (5) with Test Results and Literature for Different Model Height

In Figure 14, the wind pressure coefficients on the windward roof calculated from AIJ [10] vary little with increasing building height, while the present ones decrease with increasing building height. The AIJ [10] method overestimates wind suction pressure on the windward roof for lower buildings and underestimates for higher ones.

Figure 15 shows little difference between present test data and those based on AIJ [10] in most cases, while Equation (5) shows a greater variety of wind pressure coefficients on the roof than the standard.
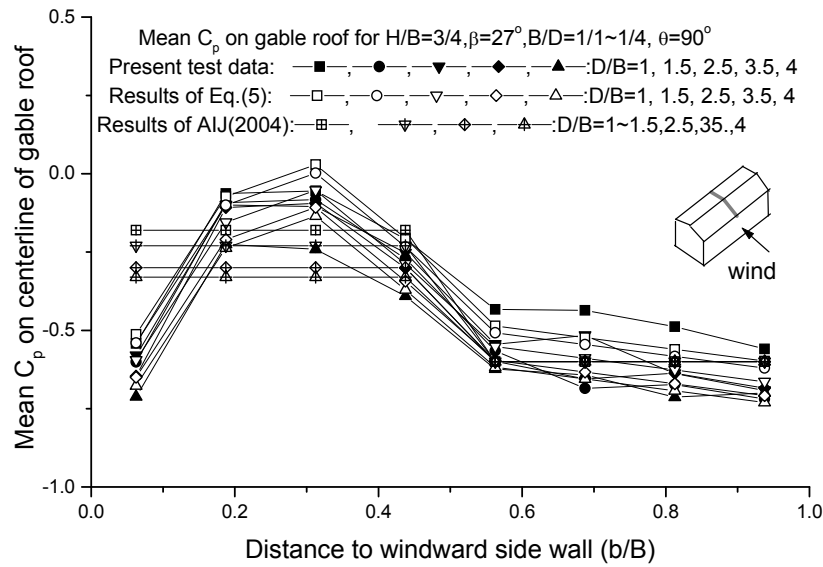
Figure 15. Comparison of Equation (5) with Test Results and Literature for Different Model Depth
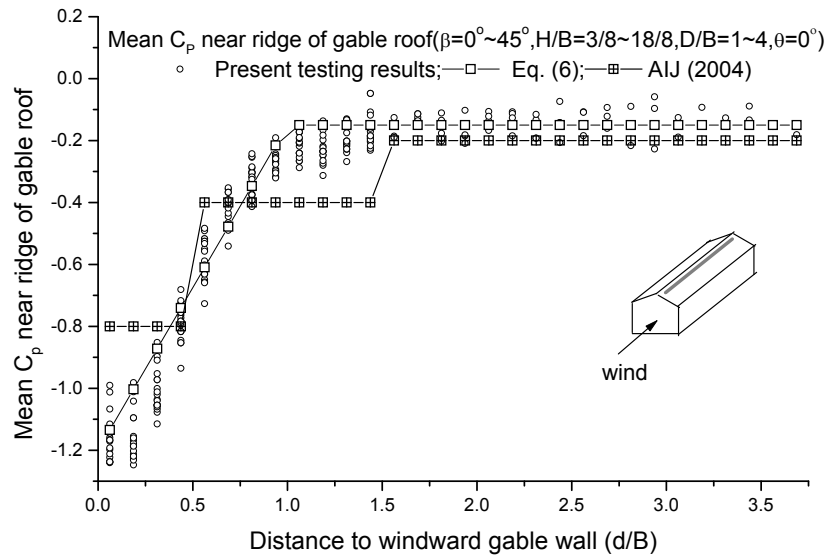
Figure 16. Comparison of Equation (6) with Test Results and Literature

Figure 16 shows that, near the windward wall, the suction wind pressure coefficients in the present test data are larger than those based on AIJ [10]. These differences may be induced by the difference in turbulence intensity. The turbulence intensity at roof height in the present study is about 0.25, while those in some referenced papers (7~9) of AIJ [10] are 0.11~0.17, which are lower than present one. To the rearward, the values given by Equation (6) match quite well with those given by the standard.

It is must be emphasized that Equation (5&6) are fitted with the wind tunnel test data of gable roofed low-rise buildings with a roof pitch of 18.4°~45°, a height/breadth ratio of 3/8~18/8 and a depth/breadth ratio of 1 ~ 4 in a suburban wind field. For other buildings with geometric parameters different from the present ones in different wind fields, the equations may not yield correct results.

6.   CONCLUDING REMARKS

Wind pressures on the roofs of 30 models of gable or hip-roofed low-rise buildings with roof pitches of $0^o \sim 45^o$, height/breadth ratios of $3/8 \sim 18/8$ and depth/breadth ratios of $1.0 \sim 4.0$, were measured in a simulated wind field of suburban terrain.   A database of wind loads on the roofs and walls of low-rise buildings is made from results of this wind tunnel test and the contours of the wind pressure coefficients are disclosed on a website.

Mean wind pressure coefficients on gable roofs for wind direction angles of 0° and 90° were analyzed. When wind flowed across the roof ridge, with increasing roof pitch, $\overline{C}_p$ on the windward roof increased while those on the leeward roof were fixed at about -0.6 regardless of roof pitch. $\overline{C}_p$ on windward gable roofs with a roof pitch large than 18.4o can be considered as linear functions of roof pitch. With increasing height/breadth ratio, $\overline{C}_p$ on the windward roof decreased, while that on the leeward roof was affected little by the height/breadth ratio. $\overline{C}_p$ on the whole roof decreased with increasing depth/breadth ratio. When wind flowed along the roof ridge, $\overline{C}_p$ was negative and increased along the wind direction. When the distance from the windward gable end to the measured point was larger than the house breadth, $\overline{C}_p$ did not increase any more and remained fixed at about -0.15. In this condition, $\overline{C}_p$ on the whole roof was hardly affected by roof pitch, house height or house depth.

Based on the analysis, two new equations for calculating wind pressure coefficients on gable roofs for wind flowing along or across the roof ridge were fitted. The equations fitted well with present test data, which were close to data from Holmes' book. However, there were some differences between the present data those calculated from the standard. These differences may have been induced by the different turbulence intensity of the testing wind field. The fitted equations show more variety of wind pressure coefficients on the roof than the standard.

ACKNOWLEDGEMENTS

REFERENCES

[1]   Holmes, J.D., "Wind Loading of Structures", Spon Press, London, UK, 2001.
[2]   Uematsu, Y. and Isyumov, N., "Wind Pressures Acting on Low-rise Buildings", Journal of Wind Engineering & Industry Aerodynamics, 1999, Vol. 82, pp. 1-25.
[3]   Stathopoulos, T., "Turbulent Wind Action on Low-rise Buildings", Ph.D Thesis, Faculty of Engineering science, The University of Western Ontario, Canada, 1979.
[4]   Stathopoulos, T., Surry, D. and Davenport, A.G., "A Simplified Model of Wind Pressure Coefficients for Low-rise Buildings", Proceedings of ICOSSAR'85, 1985.
[5]   Holmes, J.D., "Wind Pressure and Force on Tropical Houses", Final Report of Project No. 17 of the Australian Housing Research Council, Melbourne, Australia, 1980.
[6]   Holmes, J.D., "Wind Pressure on House with High Pitched Roofs", Wind Engineering Report 4/81, James Cook University, Townsville, Australia, 1981.

[7]   Kamei, Y. and Maruta, E., "Wind Tunnel Test Study on Wind Pressure of Gable Roof Buildings, Part 2: Cases With Eaves (in Japanese)", Proceedings of AIJ conference (Structure Construct Engineering), September 1981, pp. 1041-1042.

[8]   Ueda, H., Tamura, Y. and Fujii, K., "Effects of Turbulence of Approaching Wind on Mean Wind Pressure Acting on Flat Roofs (in Japanese)", Journal of Structure Construct Engineering, 1991, AIJ, No. 425, July, pp. 91-99.

[9]   Maruta, E. et al., "A Study on Wind Pressure Coefficients about Low-rise Buildings with Gable Roofs, Part 3: Mean Wind Pressure Coefficient and Wind Direction (in Japanese)", Proceedings of AIJ conference (B), August 1992, pp. 119-120.

[10]   AIJ, "AIJ Recommendations for Loads on Buildings", Architectural Institute of Japan, 2004.

[11]   Meecham, D., Surry, D. and Davenport, A.G., "The Magnitude and Distribution of Wind-induced Pressures on Hip and Gable Roofs", Journal of Wind Engineering & Industry Aerodynamics, 1991, Vol. 38, pp. 257-272.

STRUCTURAL STEEL DESIGN CODES: VEHICLES FOR IMPROVING PRACTICE OR FOR IMPLEMENTING RESEARCH?

D.A. Nethercot

Department of Civil and Environmental Engineering, Imperial College London, UK
(Corresponding author: E-mail: d.nethercot@imperial.ac.uk)

ABSTRACT: Drawing on over 30 years of personal involvement with the preparation of codes of practice for structural steel design, the issue of academic elegance versus practitioner practicality is discussed. Several examples taken from recently produced codes are used to illustrate different manifestations of the issue. The matter is discussed within the wider context of both the growing internationalisation of codes and the substantial supporting infrastructure needed by designers to efficiently implement their provisions. Although the specifics relate largely to the design of steel buildings in the UK and the wider European context, it is thought that the points stated, lessons learned and recommendations made are of general relevance.

Keywords: codes of practice, design, steel structures, structural engineering

1.   INTRODUCTION

Design Codes covering some aspects of steel construction started to become a feature in several countries during the early and middle part of the last century (Baker [1]). Initially, these tended not to be national documents but rules and procedures with varying degrees of comprehensiveness and differing scientific bases issued by City authorities and other organisations with some sort of responsibility for the control of construction. Not surprisingly, there was great variation, leading to various levels of safety within the same country and giving considerable difficulty to those organisations wanting to work across several different districts. Within the UK, so-called sets of rules for steel construction often concentrated on fire prevention in buildings, gave some information on loading and provided general guidance on the principles of overall stability of construction. Detailed rules for the proportioning of individual elements based on an appreciation of the mechanics of load resistance were not necessarily the main feature.

These local documents were quickly followed by the first generation of National Codes. However, there was still significant variation between rules covering similar issues provided by different countries, since the concept of a generally accepted underlying research base had yet to become established. It was also the case that a "Code of Practice" was often essentially just that i.e. the encapsulation of established good practice rather than the setting down of a collection of scientifically based procedures.

Increasing steel production, plus the need in several regions around the world to rebuild, meant greatly increased development in the period immediately following the end of the 2nd World War. For example, the construction of many steel bridges in Germany led to the emergence of DIN 4114, covering advanced aspects of buckling and steel plated structures that, because of the absence of any form of local equivalent, was used for many major bridge projects extending far beyond Germany. Other forms of influence e.g. the former British Commonwealth and American presence overseas, meant that documents originally produced for home use often found significant take-up elsewhere – sometimes explicitly and sometimes implicitly in the form of simply being copied and issued as the local Code. Of course, objections tended to be muted since "imitation is

the sincerest form of flattery".

During the 50s, 60s and 70s activity surrounding the preparation of Codes developed rapidly (2). New editions giving improved coverage of an ever wider range of topics were produced, completely new areas such as: composite construction, light gauge steelwork and stressed skin design, were addressed.   Newer formats e.g. limit states design, were adopted.   Much of this was driven by the regulatory side for whom the phrase "Is it in accordance with the Code" gave an all too easy method of discharging their responsibilities for construction safety.   Much was underpinned by the growing body of research data that meant that it now became possible to provide rules and procedures for topics previously considered "too difficult".

Not all this development was necessarily Government driven.   In several areas Industry played a significant role e.g. AISC in the United States is not the National Bureau of Standards.   Moreover, in some cases where no Code was provided, industry (or industry representative bodies) took the lead to develop guidance.   In the UK the phrase "plastic design to BS 449" was often used; the Code (3) contained just two general sentences; "You may use it.   The load factor shall be 1.7". All detailed rules were given in a pair of BCSA Black Books (Burnett [4] and Horne [5]).

Growing internationalisation of the construction industry, plus greater interactions within the research community have, in the last third of the 20th Century, led to a growing body of activity designed to prepare Codes valid across national boundaries.   The prime example of this is, of course, within the EU, leading to the preparation and issue of the Structural Eurocodes – specifically EC3 for Steelwork and EC4 for Composite Construction - as part of the suite of 10 documents covering Structural Design in all the main materials.   But other, far reaching, collaborations also exist e.g. the decision of Australia and New Zealand (themselves two hours flying time apart) to work with the United States and Canada on a joint Code covering light gauge steel construction.

Based very much on the author's personal experience during the past 35 years, this paper explores some of the issues faced by modern steel design codes.   These include: simplicity versus rigour, brevity versus comprehensiveness, safety and economy, elegance versus ease of use, transparent rules versus computational procedures etc.   It also exposes the tensions sometimes observed between the research community's desire for technical advance and the practitioner's wish for greater economy.

2.   ROLE OF CODES

In the UK BS0 – a Standard for Standards – lists the six aims of Standardisation as:

   (i)   To simplify the growing variety of products and procedures.
   (ii)   To improve communication.
   (iii)   To promote overall economy.
   (iv)   To ensure safety.
   (v)   To protect consumer and community interests.
   (vi)   To eliminate trade barriers.

The possibilities for conflict are immediately clear.   Will (i) and (iii) always agree?   Can (iii), (iv) and (v) always be reconciled?

More particularly, in presenting the background thinking to the development of the Part 3 of

BS5400 to a conference in 1980 (Flint [6]) the Chair of the Committee responsible, Dr A R Flint, identified 5 parties, each with different legitimate requirements from that Steel Bridge Code. Leaving aside the owners, fabricators and suppliers of steel, it is of interest to contrast his concept of the requirements of designers and researchers:

- "Designers have different priorities. Many plead for simplicity in a Code both for speed of application and to enable it to be used by engineers with limited experience.   Some expect rules to be both simple and all embracing.   Others accept that they should refer to fundamental knowledge when designing major bridges and want freedom for experienced designers to work beyond the scope of a Code.   Those competing for world-wide markets require the Code to produce the "most economical" bridges.   Simplicity of design rules and economy in the material content of a bridge are incompatible for other than the simplest structures."

- "Researchers desire a Code to be technically perfect and comprehensive, making use of the most recent research results."

Without the direct involvement of those responsible for the latest technical developments in the subject area i.e. the researchers, in the Code drafting process, how is it possible to ensure that the most up to date thinking has been properly embodied?   But if the representatives of the research community merely see the preparation of a new Code as an opportunity to promote their latest ideas – even to the extent of proposing incomplete and untried approaches based on work that is yet to receive public scrutiny – then their contribution amounts to an exercise in vanity rather than the guarantee of intellectual rigour.   The solution is, of course, that the researchers need to act in a statesmanlike fashion, making objective decisions and offering sound advice that accords with the best interests of the task in hand rather than be influenced by personal preferences.

3   POTENTIAL TENSIONS

3.1   Ease of Use versus Academic Nicety
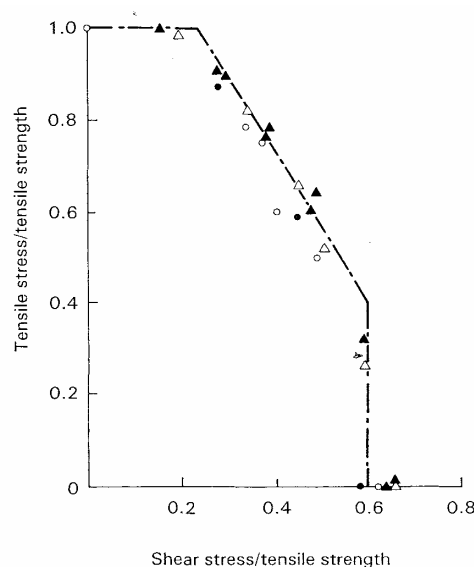
Figure 1. Trilinear Interaction Curve for Bolts Under Combined Tension and Shear;
Comparison with Test Data

Figure 1 presents a typical set of test data (Kulak [7]) for the strength of bolts subjected to combined tension and shear, a condition often found in practical connections. Several forms of interaction relationship are possible. Two particular arrangements are:

1   Some form of curved interaction e.g. reference (Kulak [7]) suggests:

$$\frac{x^3}{(0.62)^2} + y^2 = 1.0$$

in which   x   = ratio of shear stress on the shear plane to the tensile strength

y = ratio of tensile stress to the tensile strength

2   Trilinear

The former is obviously elegant and allows a single formula to cover all combinations. The later appears less straightforward when given as a formula yet has two great practical advantages.

In many cases the full tensile (or shear) resistance may be used. Design calculations are much simpler, since providing the applied tension (or shear) is less than the 60% of the full capacity corresponding to the plateau limits in the figure, the actual value is immaterial in terms of its effects on the other resistance quantity.

Since it is rare in practice to find that the same bolts are required to resist high levels of both tension and shear, the great majority of design arrangements will not fall on the inclined part of the diagram and the actual design check will therefore be much simpler. Thus designers arc likely to prefer the convenience of the trilinear rule, whereas researchers might well advocate the elegance of the circular arc representation. Clearly a potential for conflicting views!

3.2   Guidance on Implementation versus Limitation to Principles

A fundamental parameter used when checking the bending resistance of laterally unrestrained beams is the elastic critical moment M_{cr}. This property may either appear explicitly in the design formula or be used implicitly in some form of equivalent slenderness. Calculation of M_{cr} is lengthy and involves properties not familiar to most users e.g. warping rigidity of the cross-section. Thus some codes assist the designer by providing specific guidance on the determination of M_{cr}. For example, in BS 5950: Part 1 M_{cr} is not used explicitly but forms part of the "lateral-torsional slenderness" λ_{LT}, for which a full calculation procedure is provided. In contrast EC3 not only uses M_{cr} directly but provides no assistance in its calculation. Designers must therefore make reference elsewhere. For cross-sections other than doubly symmetrical I-sections e.g. unequal flange I-beams, working from first principles is particularly tedious.

Thus the EC3 procedure first requires the calculation of M_{cr}; no specific guidance is provided so the user must resort to textbooks (Trahair [8]) or design guides (9).

For bisymmetrical I-section the elastic critical moment M_{cr} may be obtained from:

$$M_{cr} = m \left\{ \left[\frac{\pi^2 EI_y}{(kL)^2} \right] \left[GJ + \frac{\pi^2 EI_w}{(kL)^2} \right] \right\}^{1/2}$$

in which   m   =   factor that depends on the shape of the in-plane bending moment distribution

EI_y =   minor axis flexural rigidity

GJ   =   torsional rigidity

EI_w =   warping rigidity

k   =   effective length factor allowing for end restrain in the buckling plane

L   =   length between points of effective lateral restraint

If the cross-section has unequal flanges but is still symmetric about its minor axis i.e. a monosymmetric beam, then the expression for M_{cr} contains additional properties:

$$M_{cr} = m \left\{ \frac{\pi^2 EI_y}{L^2} \right\}^{1/2} \left\{ \left[GJ + \frac{\pi^2 EI_w}{L^2} + \left\{ \frac{\beta}{2} \left(\frac{\pi^2 EI_y}{L^2} \right)^{1/2} \right\}^2 \right]^{1/2} + \frac{\beta}{2} \left(\frac{\pi^2 EI_y}{L^2} \right)^{1/2} \right\}$$

in which β is monosymmetric parameter (8)

Once a value for M_{cr} has been determined the buckling resistance moment M_b is calculated from:

$$M_b = W_y f_y \left[\frac{1}{\phi_{LT} + \left(\phi_{LT}{}^2 - \beta \overline{\lambda}_{LT}{}^2 \right)^{1/2}} \right]$$

in which $W_y f_y$ =   cross-sectional moment of resistance (W_y depends on section classification)

$$\phi_{LT} = 0.5 \left\{ 1 + \alpha_{LT} \left(\overline{\lambda}_{LT} - \overline{\lambda}_{LT0} \right) + \beta \overline{\lambda}_{LT}{}^2 \right\}$$

and $\overline{\lambda}_{LT} = \left[W_y f_y / M_{cr} \right]^{1/2}$ is the modified slenderness

α_{LT}, β and $\overline{\lambda}_{LT0}$ are defined in the Code; α_{LT} and $\overline{\lambda}_{LT0}$ control the positioning of the design curve.

Clearly the above represents an extremely lengthy calculation process, especially if trial and error is necessary, with no guidance being provided on how best to arrange the calculation, what shortcuts might be acceptable if some degree of conservation/inaccuracy could be accepted etc.

Contrast this with the designer-oriented approach of BS 5950: Part 1 to determine M_b.

$M_b = P_b Z_{ex}$

in which p_b = buckling strength, $p_b = f(p_y, \lambda_{LT})$

Z_{ex} = approximate section modules

Determination of p_b is facilitated through the introduction of λ_{LT} defined by:

$$\lambda_{LT} = \left\{ \left(\pi^2 E / p_y\right)^{\frac{1}{2}} \left(M_{cx} / M_{cr}\right)^{\frac{1}{2}} \right\}$$

in which p_y =   material design strength

                M_{cx} =   in-plane moment capacity, $p_y Z_{ex}$

                M_{cr} =   elastic critical moment

Rather than use M_{cr} explicitly, however, λ_{LT} may be calculated from:

$$\lambda_{LT} = uv\lambda\sqrt{\beta_w}$$

in which v is tabulated for standard sections or may safely be taken as 0.9 for standard hot rolled sections or 1.0 otherwise:

$$v = \left[1 + 0.05\left(\lambda / x\right)^{\frac{1}{2}}\right]^{-\frac{1}{4}}$$

$$\lambda = L / r_y$$

    x   is also tabulated for standard rolled sections or may be approximated by D/T

$$\beta_w = Z_{ex} / S_x$$

Since for compact sections $Z_{ex} = S_x$ and noting that v is normally not much less than unity, the particularly simple approximation:

$$\lambda_{LT} = 0.9 \, x \, 1.0 \, x \, \lambda \, x \, 1.0$$

may be used to obtain a safe (high) estimate and thus a safe (low) value for p_b and hence M_b.   No similar quick simplification of the EC3 approach appears possible.

3.3   Level of Detail

One of the fundamental pieces of information required when designing a composite beam is the strength of the shear studs used to transfer the interface forces between the steel and concrete surfaces.   Its basis is normally some form of representation of test data – obtained from a combination of laboratory push-off and/or beam tests for representative samples.   Over the years a general consensus has emerged that a pair of design equations, covering the two basic failure modes of stud shear and concrete crushing, is appropriate (8).

P_{Rd} = $0.08 f_u \left(\pi d^2 / 4\right)$ stud shear

P_{Rd} = $0.029 d^2 \left(f_{ck} E_{cm}\right)^{\frac{1}{2}}$ concrete crushing

in which f_u =   ultimate tensile strength of the steel
                d   =   shank diameter

f_{ck} = cylinder strength of concrete

E_{cm} = mean secant modulus of concrete

Forms of composite beam beyond basic flat slab arrangements have become increasingly common in recent years. One particular manifestation is the use of metal decking as an aid to the construction process. Manufacturers around the world have been in competition to produce ever more efficient (in terms of structural performance) and effective (in terms of usage of concrete and the inclusion of practically useful factors) profiles.

In order to allow for the presence of metal decking, design rules for shear connections in flat slabs have traditionally included empirical coefficients, obtained from tests on each profile. Table 1 reproduces the EC4 material. Strictly speaking, as each new deck is introduced more tests and a further set of coefficients are required. Not only has this not always happened but the appearance of ever more complex profiles has seen the identification of new forms of failure not possible with plain concrete. (9) These cannot, of course, be properly handled by further extrapolation of the original design concept i.e. the pair of equations governing only stud shear and concrete crushing.

Table 1. EC4 Modification Factors for Dealing with Metal Decking

Case	Reduction factor
Ribs parallel to beam	$k_1 = 0.6 \dfrac{b_o}{h_p}\left(\dfrac{h}{h_p}-1\right) \leq 1.0$
Ribs perpendicular to beam	$k_t = \dfrac{0.7}{\sqrt{N_r}}\dfrac{b_o}{h_p}\left(\dfrac{h}{h_p}-1\right) \leq 1.0$
in which N_r = number of studs in one rib where it crosses the beam < 2 h => hp + 75 mm and the other terms are defined in the diagrams below	
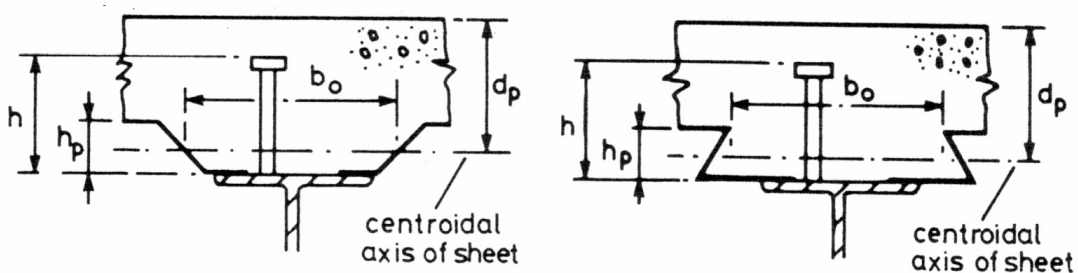
The situation is now such that even if code modifications could keep pace with the introduction of each new deck profile, the catalogue of coefficients – each directly related to a particular commercial product – would be both too lengthy for a Code and would contravene a firmly established principle that Codes should not relate directly to particular commercial products, remaining at the level of generic guidance.

One solution would be to remove all but the basic generic guidance and to rely on manufacturers themselves to provide the specialist information required for their own products. It would therefore be in their interests to ensure that this was kept up to date. A precedent already exists in the area of light gauge steel design, where much design information is provided by the manufacturers of purlins, sheeting systems etc. Not only does this remove any linkage in the

Code to particular products, it also encourages manufacturers to conduct their own scientific studies and thus to understand the performance of the items they manufacture and sell since it is normally possible to produce more competitive procedures on the basis of specialist testing than by relying simply on the straightforward application of the generic code procedures.

3.4   Formulation

The most general component in a steel frame is the beam-column, a member subjected to combined compression (or tension) and bending about both principal axes.   Design rules normally rely on the use of some form of interaction equation linking resistances under each basic type of loading when acting alone.   Figure 2 gives both a pictorial representation of a uniaxial bending interaction diagram and the 3-dimensional interaction surface necessary for the biaxial case (Menzies [10]). The precise shape of the interaction for any particular arrangement will, of course, depend on the details e.g. shape of cross-section, exact load arrangements, form of support etc.
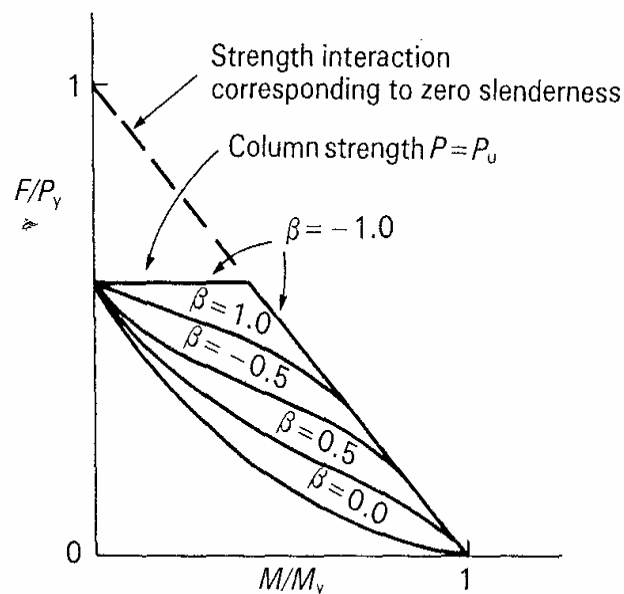
Figure 2. Uniaxial Interaction in Terms of Elastic Limit and Effect of Moment Gradient β
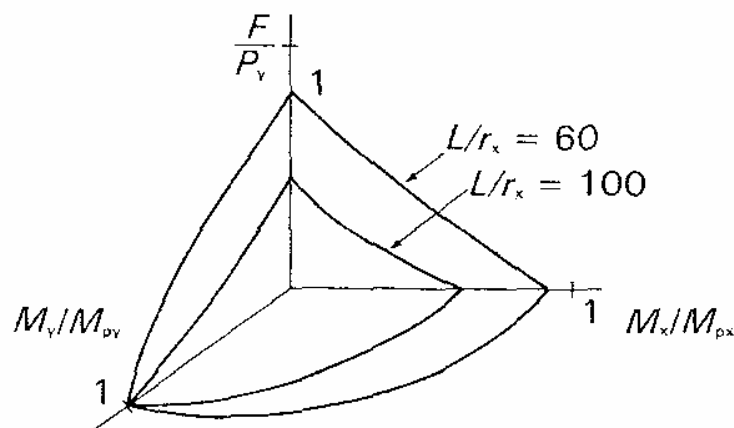
Figure 2. Indicative Interaction Surface for Slender Beam Columns Under Biaxial Loading

The emergence of numerical analysis as a credible alternative to laboratory testing as a means of determining the true ultimate strength of structural components has been a feature of structural steel

research over the past 20 years.   Once the numerical models have been properly validated against representative test data, it becomes possible to conduct far more detailed parametric studies, in which the effects of systematic changes in key variables are examined, than was the case when this needed to be done in the laboratory.   The result has been a far better appreciation of "cause and effect" i.e. the influence of each key parameter on behaviour or in terms of the beam- column problem an understanding of precisely how the interaction relationship is affected by different parameters.   This has naturally led to a wish to see this improved knowledge reflected in more rigorous design procedures.

The result in EC3 is that the design rules for beam-columns are extremely complex.   Two procedures are given and both incorporate several coefficients that in turn depend on a number of properties of the system under consideration.   They adopt the form:

$$\frac{N_{Ed}}{\chi_y N_{Rk}/\gamma_{M1}} + k_{yy}\frac{M_{y,Ed}}{\chi_{LT}M_{y,Rk}/\gamma_{M1}} + k_{yz}\frac{M_{z,Ed}}{M_{z,Rk}/\gamma_{M1}} \le 1$$

$$\frac{N_{Ed}}{\chi_z N_{Rk}/\gamma_{M1}} + k_{zy}\frac{M_{y,Ed}}{\chi_{LT}M_{y,Rk}/\gamma_{M1}} + k_{zz}\frac{M_{z,Ed}}{M_{z,Rk}/\gamma_{M1}} \le 1$$

in which N_{Ed}, $M_{y,Ed}$, and $M_{z,Ed}$ are the design values of the compression force and the maximum moments about the y-y and z-z axis along the member, respectively

N_{Rk}, $M_{y,Rk}$, $M_{z,Rk}$ are the characteristic values of the compression resistance of the cross section and the bending moment resistances of the cross-section about the y-y and z-z axes, respectively

χ_y and χ_z are the reduction factors due to flexural buckling

χ_{LT} is the reduction factor due to lateral torsional buckling taken as unity for members that are not susceptible to torsional deformation

k_{yy}, k_{yz}, k_{zy}, k_{zz} are interaction factors k_{ij}

All of the terms apart from the interaction factors k are reasonably straightforward as they follow directly from, the individual load and resistance effects.   However two alternative procedures for calculating the k-factors are given.   Both run to 2 pages of tabulated formulae that, themselves, introduce further parameters.   In addition, different expressions are required for members "not susceptible to torsional deformation" or "susceptible to tostional deformations" as well as for class 1 and 2 sections and for class 3 and 4 sections.

Both procedures have been calibrated against appropriate numerical data (Boissonnade [13] and Lindner [14]). This has resulted in procedures that give a very close representation for those cases used in their derivation.

Two criticisms may be levelled at this:

- Lack of transparency i.e. it is very difficult for a designer to see the linkage between some of the problem parameters and the likely result in terms of the effect on the interaction calculation.
- Restricted applicability i.e. although the design formulae have been very precisely calibrated for certain arrangements, their use for situations that do not conform to one or other of these is, effectively, unknown.

Codes produced before the availability of such comprehensive but selective data tended to use more general design approaches e.g. the Chen concept (12) defined as:

$$\left(\frac{M_{Edy}}{M_{cy}} \right) \ + \ \left(\frac{M_{Edz}}{M_{cz}} \right)^{\beta} > 1.0$$

in which M_{cy} and M_{cz} are the resistance moments in the presence of the axial load N_{ed}

and α, β are appropriate powers, taken as 1.0 for the most conservative interpretation

and provided detailed procedures for a limited number of cases for which more substantial data existed. Cases outside this range could then be dealt with by adopting the most conservative interpretation of the design concept, in the expectation that it would lead – even for cases that had not previously been examined in a more rigorous fashion – to safe results. It was also possible for designers to use the simpler and conservative form of the design expressions for preliminary checks so as to gain a good indication quickly that a particular arrangement would be of the correct order of magnitude.

4   INTRODUCTION OF NEW CODE

The following quotation epitomises the sentiments most frequently heard from the Structural Engineering Community when confronted by a new or revised Code:

> "The onset of new or revised regulations invariably heralds a trying period of the unfortunate people who have to work such regulations. This applies both to those who have to comply with, and those who have to administer, such regulations"

Readers might think this to be contemporary. It actually dates from 1955 and relates to the introduction of a revised version of BS449 – a document regarded by many practitioners with affection as a model for the sort we should be using nowadays. It is interesting to speculate on the reasons behind this reaction:

- Any newly introduced document is, by definition, unfamiliar.
- New is often perceived as technically more complex.
- This leads to the expectation that it will be more difficult to use.
- The consequence is to presume longer design times.
- Since there is no expectation of additional fee income, the presumption is that profitability will be eroded.

How might this cycle be reversed?

- A properly orchestrated campaign to both prepare the community for a new document and to explain how it should be used, including the provision of illustrations where it confers genuine benefits as compared with its predecessor is clearly crucial.
- More comprehensive coverage, meaning fewer situations that need to be resolved "outside the Code" is normally thought beneficial by practitioners.
- Time spent on making the procedures easy to follow and, above all, quick to implement should lessen the view of the new document as being "difficult".
- Identification during the introductory period that problem areas in the previous document have been recognised, accepted and dealt with in an improved fashion should demonstrate that users concerns (with the previous Code) have been addressed.
- Well in advance of the introduction, clear views on the reason why the new document is needed and illustrations of how it will make the lives of designers easier should help create a climate of anticipation – rather than dread.

When viewed like this, much of the above might seem self evident.   It is, surprising how often in the past these simple lessons based on an appreciation of human nature seem to have been ignored. Statements such as "because it gives a more consistent level of reliability" or "because it is technically more up to date" are unlikely to produce converts among potential users.   Even though researchers involved directly with the preparation of a new Code may hold these views (and the expectation for a new document is that it would exhibit these characteristics), they are best kept in the background.   Presenting the new Code as "more comprehensive in its coverage", "containing easier to use treatments for commonly encountered topics", "reducing the scope for varying interpretations", "providing more economical solutions for certain topics", etc, is likely to be far better received.

It is also necessary these days to recognise that the introduction of a new Structural Code brings with it the need for substantial updating of the "design infrastructure used by practitioners i.e. computer software, manufacturers literature textbooks, design guides etc.   The author has recently been involved in an exercise (15) designed to identify the needs of the UK structural design community as it migrates from a system based on National Codes to one that relies on the Structural Eurocodes.   This has graphically illustrated the scale of the task involved if it is to be undertaken in anything approaching a coherent and comprehensive fashion.

5.   CONCLUSIONS

Following a brief history of the background of structural steel design codes over the past 100 years, the issue of academic elegance versus practitioner practicality has been discussed.   Four specific topics have been used to illustrate different facets of the issue.   An appreciation of the needs of the Code users and of the concerns influencing their behaviour is offered as something that should be central to the whole drafting and subsequent introduction operations.   The substantial effect of the introduction of a new Code on the associated portfolio of design support is highlighted as a matter of great concern to practitioners – but something that is often left to develop in an ad hoc fashion once the Code has been produced.

ACKNOWLEDGEMENTS

REFERENCES

[1]   Baker, J.F., "Comparison of the Regulations Governing the Design of Steel Frame Buildings", 1st Report of the Steel Structures Research Committee, London, HMSO, 1931.

[2]   American Institute of Steel Construction, "Stability of Metal Structures: A World View", AISC, 1982.

[3]   British Standards Institution, "BS449: Part 2: 1969, The Use of Structural Steel in Building", BSI, London, 1969.

[4]   Burnett, N., et al., "Plastic Design", The British Constructural Steelwork Association Publication Number 28, London, 1965.

[5]   Horne, M.R., "The Plastic Design of Columns", The British Constructional Steelwork Association Publication Number 23, London, 1964.

[6]   Flint, A.R., "The History, Scope, Aims and Principles of BS5400 in relation to Steel and Composite Bridges in the Design of Steel Bridges", Edited by Rockey, K.C. and Evans, H.R. Granada, London, 1981.

[7]   Kulak, G.L., Fisher, J.W. and Struik, J.A.H., "Guide to Design Criteria for Bolted and Riveted Joints", Second Edition, Wiley, New York, 1987.

[8]   Trahair, N.S., "Flexural-Torsional Buckling of Structures", E and FN Spon, London, 1993.

[9]   Column Research Committee of Japan, "Handbook of Structural Stability", Corena, Tokyo, 1971.

[10]   Menzies, J.B., "CP117 and Shear Connectors in Steel-concrete Composite Beams, March 1976", The Structural Engineer, Vol. 49, No. 3, pp. 137-153.

[11]   Patrick, M., "Composite Beam Shear Connection Design and Detailing Practices for Australian Steel Decks", Report Number CCTR/CBSC-001-04, University of Western Sydney, July 2004.

[12]   Chen, W.F. and Atsuta, T., "Theory of Beam –Columns: Vol. 2, Space Behaviour and Design", McGraw Hill, 1977.

[13]   Boissonnade, N. et al., "Improvement of the Interaction Formulae for Beam-columns in Eurocode 3", Computers and Structures, 2002, Vol. 80, pp. 2375-2385.

[14]   Lindner, J., "Design of Beams and Beam Columns", Progress in Structural Engineering and Materials, 2003, Vol. 5, pp. 38-47.

[15]   Institution of Structural Engineers, "National Strategy for Implementation of the Structural Eurocodes; Design Guidance", Report to Office of the Deputy Prime Minister. (www.istructe.org.uk/eurocodes), 2004.

THE ULTIMATE BEHAVIOUR OF CRACKED SQUARE HOLLOW SECTION T-JOINTS

S.T. Lie[*], Z.M. Yang, S.P. Chiew and C.K. Lee

School of Civil and Environmental Engineering, Nanyang Technological University
50 Nanyang Avenue, Singapore 639798, Singapore
Tel: +65-6790-5284; Fax: +65-6792-1650
*(Corresponding author: E-mail address: cstlie@ntu.edu.sg)

ABSTRACT: The ultimate static strength of tubular joints is usually calculated at the design stage based on empirical formulae incorporating the joint geometry, loading mode and materials strength. However, fatigue cracks have been detected in some aging structures, which tend to reduce the static strength. Methods for predicting the loss of strength of cracked tubular joints are therefore very important in practice. Very few published results are available concerning the residual strength of cracked square hollow section (SHS) joints. In order to develop guidelines on assessing the static strength of fatigue-cracked square hollow section (SHS) joints, a range of numerical analysis and full-scale test has been carried out on cracked and uncracked T-joints. The non-linear elastic-plastic finite element (FE) technique has been employed successfully for calculating the plastic collapse loads of uncracked and cracked T-joints under axial load at the brace end. Accordingly, an approach to predict the ultimate strength of cracked SHS T-joints is proposed in this paper. The experimental test results, conducted at room temperature, have confirmed and agreed well with the FE analysis findings.

Keywords: crack; finite element technique; non-linear analysis; square hollow section (SHS); T-joints; ultimate strength

1. INTRODUCTION

It is well known in practice that almost all engineering structures and components contain cracks or crack-like flaws. These are either introduced during manufacture, especially if welding is used, or during the earlier service life by environment fatigue loading or by accidental damage, i.e. impact and earthquake. When the defect size increases, the structure strength capacity is reduced accordingly, and therefore, there is a need to develop a reliable procedure to determine the residual static strength of such structures containing defects.

The fracture mechanics method is the most reliable approach to assess the integrity of a cracked or damaged component with crack-like defects. The most widespread and successful assessment approach is the failure assessment diagram (FAD) approach. Based on this approach, API RP579[4], BS7910 [5] and R6 [13] give guidance for assessing the acceptability of defects in welded structures. This approach was originally developed from two criteria assessment proposed by Dowling and Townley [9]. It enables the integrity of cracked components to be assessed through two separate calculations based on the two extremes of fracture behaviour, linear elastic and fully plastic. A design curve is used to interpolate between these two failure criteria. The relative position of the assessment point on the diagram, derived from the two separate calculations, determines the integrity of the structure as shown in Fig. 1. If the assessment point falls inside the failure curve, the structure is deemed safe; if the assessment point is on or outside the curve, then failure is predicted to occur. An increased load or larger crack size will move the assessment point along the loading path toward the failure line. The reliability of the method depends on how accurately the intersection zone is described by the failure assessment curve which in turn depends on the structural geometry, type of loading and crack size.

Although the existing codes and standards do provide guidance in the form of detailed procedures for the fracture assessments, these are intended for general applications and do not necessarily give optimal solutions for all types of structures, such as welded SHS tubular joints. Because of the complexity of these tubular joint geometries, there are uncertainties with essential fracture parameter solutions; and both experimental and numerical studies are costly. In this paper, the formulae of plastic collapse load of cracked square hollow section (SHS) T-joints is derived in accordance with the yield line theory, and the failure assessment curve (FAD) is constructed using the J-integral approach. Compared with the standard BS7910 [5] FAD, some recommendations are given to extend the utilization of the standard FAD.
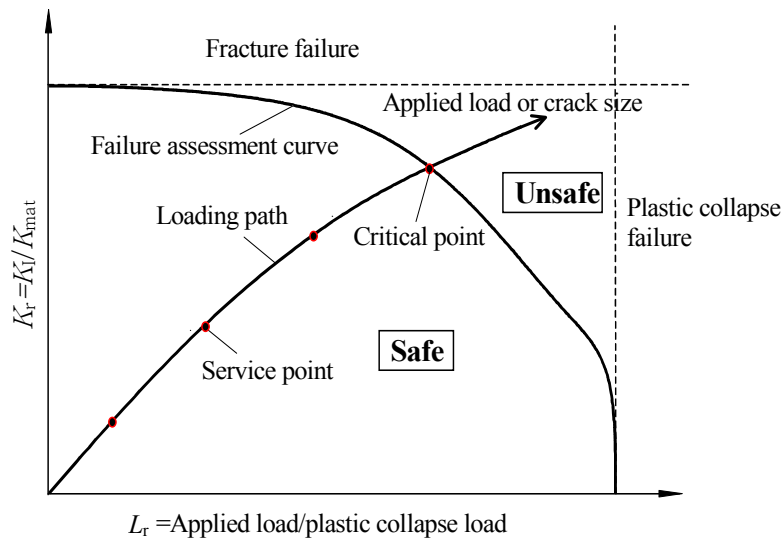
Figure 1. FAD Philosophy for the Assessment of Flawed Structure

2. DETERMINATION OF PLASTIC COLLAPSE LOAD

The plastic collapse loads for the cracked geometry are evaluated by reducing the plastic collapse loads for the corresponding uncracked geometry (Cheatani and Burdekin [6]). When the brace to chord width ratio β is less than 0.8, normally the failure model of the T and Y-joints under brace end axial loads is chord face yielding (Wardenier [14]). The ultimate strength of uncracked RHS T and Y-joints can be derived using the yield line pattern as shown in Fig. 2 (Wardenier [14]). Based on the yield line theory, an approach was given to predict the collapse loads of RHS T-joints with surface cracks in this paper, and it is validated numerically.
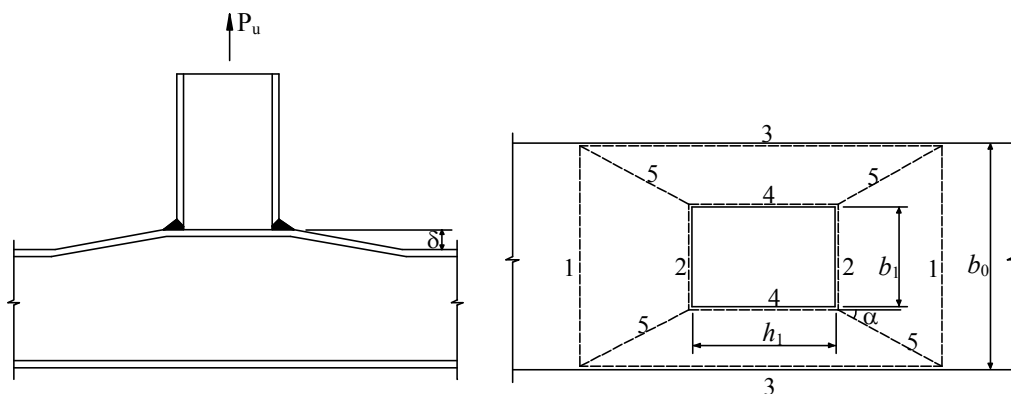
Figure 2. Yield Line Pattern for the Uncracked T-joint

For the joints containing a surface crack, the ligament in front of the crack has the capability to pull and deform the chord face. Therefore, the axial displacement of the chord face around the entire circumference of the brace and chord intersection can be assumed to be δ as shown in Fig. 3. Based on the yield line theory, the following two assumptions are deduced,

- The yield line pattern remains the same as the uncracked joint.
- The thickness of the crack region is $t_0 - a$, where t_0 is the thickness of the chord face, and a is the vertical depth of the crack under weld toe.

The corresponding yield line pattern for the cracked joint is shown in Fig. 3, the energy participated in the yield lines 1 to 5 keeps the same as the uncracked joint, they are $\dfrac{4\text{tg}\alpha}{1-\beta}\cdot\delta\cdot m_p$,

$\dfrac{2\beta\cdot\text{tg}\alpha}{1-\beta}\cdot\delta\cdot m_p$, $\left\{\dfrac{4\eta}{1-\beta}+4\cot g\alpha\right\}\cdot\delta\cdot m_p$, $\dfrac{2\eta}{1-\beta}\cdot\delta\cdot m_p$ and $4(\text{tg}\alpha+\cot g\alpha)\cdot\delta\cdot m_p$ respectively.

Because of the influence of the crack, the energy participated in yield line 2′ and 4′ is derived as follow:

yield line 2′: $\quad (b_1 - l_{c1})\cdot\dfrac{2\delta}{(b_0 - b_1)\cot g\alpha}\cdot m_p + l_{c1}\cdot\dfrac{2\delta}{(b_0 - b_1)\cot g\alpha}\cdot m_p'$ $\qquad(1)$

yield line 4′: $\quad (h_1 - l_{c2})\cdot\dfrac{2\delta}{b_0 - b_1}\cdot m_p + l_{c2}\cdot\dfrac{2\delta}{b_0 - b_1}\cdot m_p'$ $\qquad(2)$

where $m_p = \dfrac{\sigma_{e0}\cdot t_0^2}{4}$, $m_p' = \dfrac{\sigma_{e0}\cdot(t_0 - a)^2}{4}$, and σ_{e0} is yield strength of the material.

The energy by the external load P_u is equal to the participated energy in the yield lines, which gives

$$P_u = \dfrac{2\sigma_{e0}\cdot t_0^2}{1-\beta}\left\{\text{tg}\alpha + \dfrac{1-\beta}{\text{tg}\alpha} + \eta\right\} - \dfrac{\sigma_{e0}\cdot[t_0^2 - (t_0 - a)^2]}{2}\cdot\left\{\dfrac{l_{c1}}{(b_0 - b_1)\cot g\alpha} + \dfrac{l_{c2}}{b_0 - b_1}\right\} \qquad(3)$$

In accordance with assumption 1, the following relationship can be obtained from the uncracked joint (Wardenier, 1982), $\text{tg}\alpha = \sqrt{1-\beta}$. $\qquad(4)$

Substituting Equation (4) into Equation (3) gives the yield load

$$P_u = \dfrac{\sigma_{e0}\cdot t_0^2}{1-\beta}\left\{2\eta + 4\sqrt{1-\beta}\right\} - \dfrac{\sigma_{e0}\cdot[t_0^2 - (t_0 - a)^2]}{2(b_0 - b_1)}\cdot\left\{l_{c1}\cdot\sqrt{1-\beta} + l_{c2}\right\} \qquad(5)$$

where the first term is the yield load of uncracked joint, and the second one is the reduction of the yield load because of the introduction of the crack. If there are several cracks, the additional reduction terms which have the same expression need to be calculated for different crack depths and lengths. Then Equation (5) becomes

$$P_u = \dfrac{\sigma_{e0}\cdot t_0^2}{1-\beta}\left\{2\eta + 4\sqrt{1-\beta}\right\} - \sum_n \dfrac{\sigma_{e0}\cdot[t_0^2 - (t_0 - a^n)^2]}{2(b_0 - b_1)}\cdot\left\{l_{c1}^n\cdot\sqrt{1-\beta} + l_{c2}^n\right\} \qquad(6)$$

where n represent the number of cracks. Considering the influence of the weld and the chord wall thickness, the brace to chord width ratio β should be $\dfrac{b_1 + 2t_w}{b_0 - 2t_0}$, and the bracing member depth to chord width ratio η should be $\dfrac{h_1 + 2t_w}{b_0 - 2t_0}$ (Wardenier, 1982), where t_w is the width of the weld toe as shown in Fig. 4.
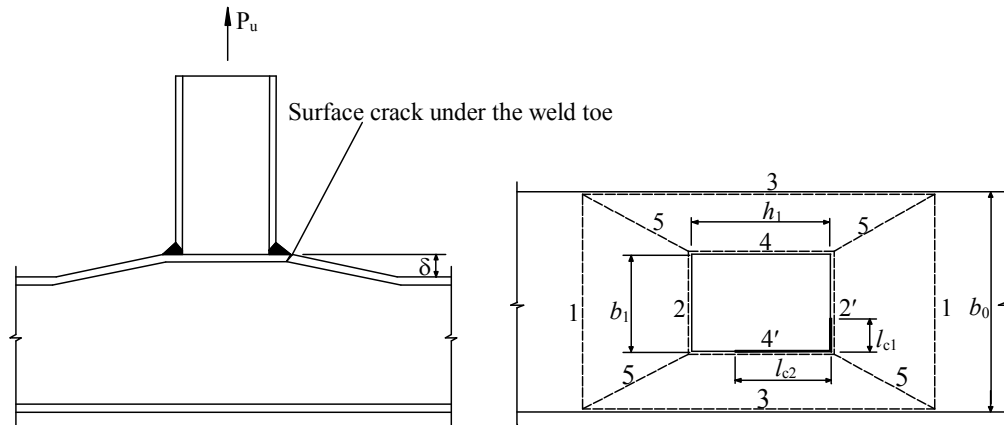
Figure 3. Yield Line Pattern for the Cracked T-joint
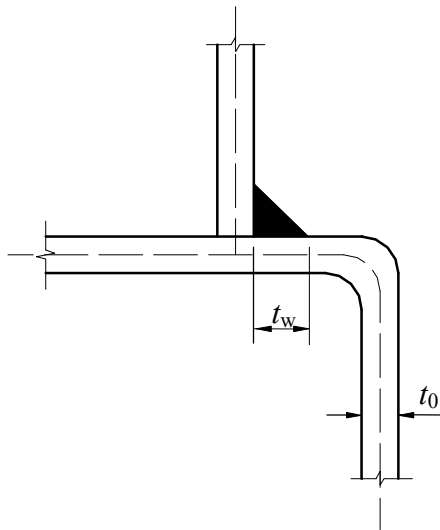
Figure 4. The Weld Details for the RHS T-joints

3.   NUMERICAL MODELING OF CRACKED SHS JOINT

In accordance with the experimental results (Chiew et al. [7]), the fatigue crack under the weld toe is inclined and slightly curved, and the crack is located at the corner of the brace where the hot spot stress is the highest. Therefore, the crack surface is modelled as an inclined plane which has an angle θ with the vertical plane as shown in Fig. 5. The crack is located at the inclined crack surface, and the inclined angle θ is varying with the crack depth. Because the geometry and the stress distribution are not symmetric with respect to the corner, the shape of the crack is not symmetric either. In this study a two halves of semi-ellipse model is used and it is mapped onto the three dimensional inclined crack surface as shown in Fig. 6. 20-node brick elements are used throughout to model the joint except at the crack zone. Around the crack front, the brick elements are degenerated into wedges as shown in Fig. 7. Between the crack front and the field far away from it, 15-node prism elements and 10-node tetrahedron elements are used to refine the mesh gradually. The completed mesh of the cracked SHS T-joint is illustrated in Fig. 8. The mesh close to the crack zone is refined to capture the steep stress gradient.

In elastic problems, the nodes at the crack tip are normally tied together, and the mid-side nodes are moved to the 1/4 points as shown in Fig. 9(a). Such a modification results in a $1/\sqrt{r}$ strain singularity in the element, which enhances numerical accuracy (Lapidus and Pinder [11]). When a

plastic zone forms, the $1/\sqrt{r}$ singularity does not exist any longer at the crack tip. Consequently, elastic singular elements are not appropriate for elastic-plastic analyses. Fig. 9(b) shows an element that exhibits the desired strain singularity under fully plastic conditions. The element is degenerated to a wedge as before, but the crack tip nodes are untied and the location of the mid-side nodes is unchanged. This element geometry produces a 1/r strain singularity, which corresponds to the actual crack tip strain field for fully plastic materials (Aliabadi and Rooke [2]).
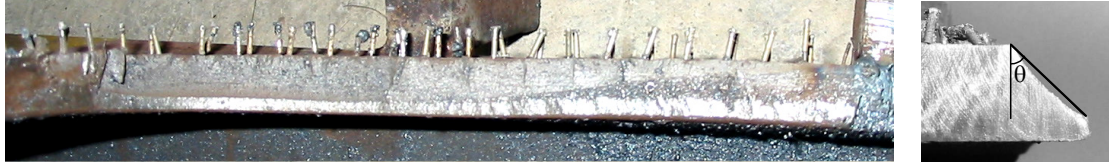
Figure 5. A Typical Crack Surface of the Damaged T-joint
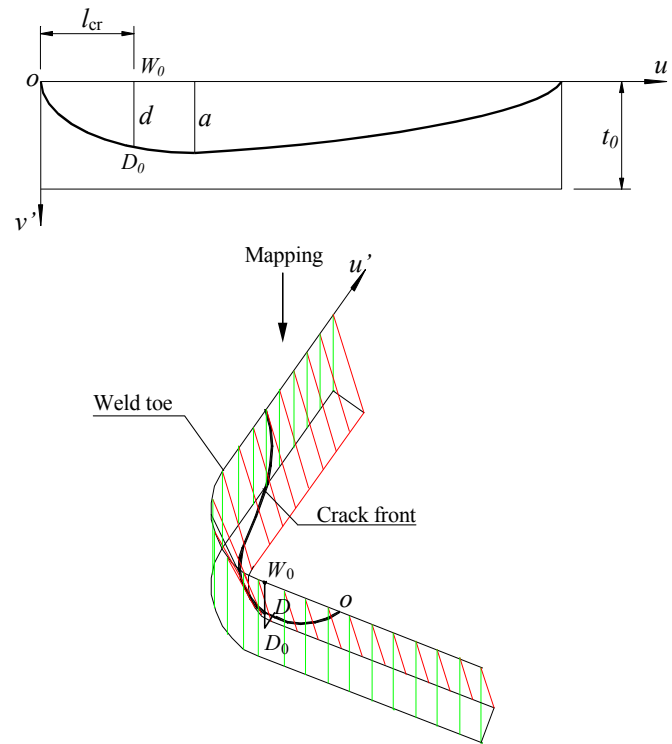
Figure 6. Modelling of the Surface Crack under the Weld Toe
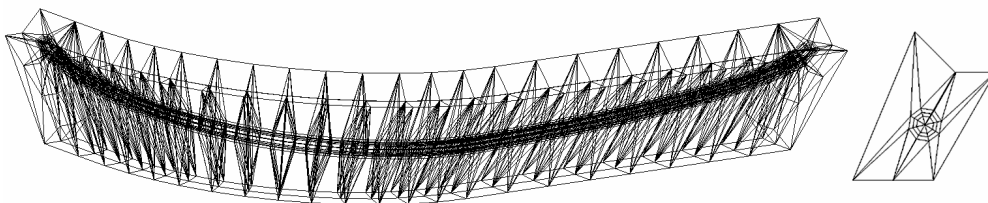
Figure 7. Mesh of the Crack Zone
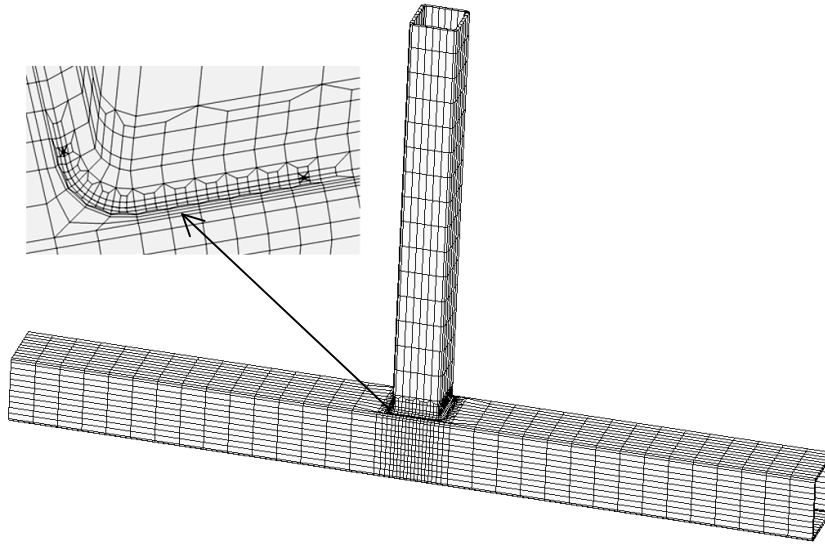
Figure 8. Mesh of the T-joint with Crack

(a) Elastic singularity element

(b) Plastic singularity element
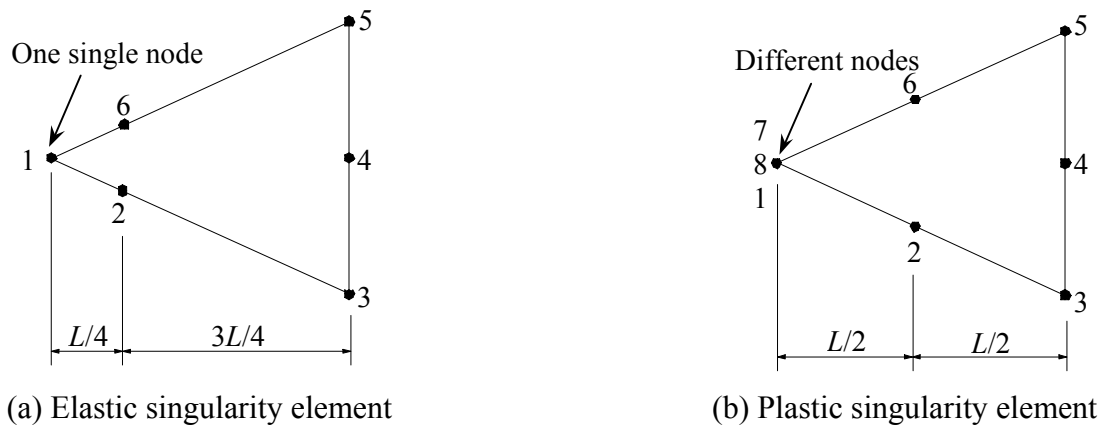
Figure 9. Crack Tip Elements used for Elastic and Elastic-plastic Analyses

4.   STATIC STRENGTH TEST OF CRACKED SHS JOINT

For validation of the numerical model, two static tests of the cracked T-joints are performed up to failure. A specially designed test rig as shown in Fig. 10 was used to test these SHS T-joints. The specimens were available from the previous fatigue test programmes conducted on a structural steel BS4360-50D. Every specimen contains at least one fatigue surface crack under the weld toe. The dimensions of the joints are given in Table 1, and the weld and crack details are tabulated in Table 2. The weld profile and the specimen preparation were carried out in accordance with the American Welding Society (AWS) Structure Welding Code D1.1-2000 [3] specifications and they were checked using the ultrasonic technique to deem the welds quality. The two ends of the chord were supported on two rollers placed on the top of the concrete supports as shown in Fig. 11. The joint was loaded under displacement control in the test rig with regular pauses for photography, visual examination and instrumentation checks until the load was observed to start decreasing from the maximum value. The applied load was obtained via load cell of the actuators, and it was also measured using the strain gauges attached at the middle of the brace to confirm the load readings.

The crack growth was monitored using the Alternating Current Potential Drop (ACPD) technique (Dover et al., 1995). The ACPD probes around the fatigue crack location are shown in Fig. 12.
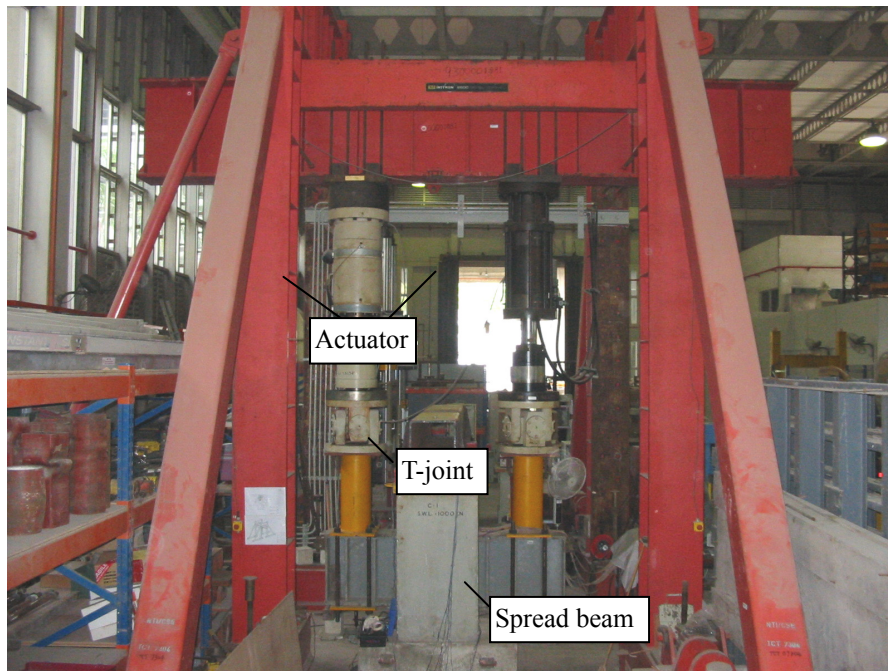
Figure 10. The Test Rig
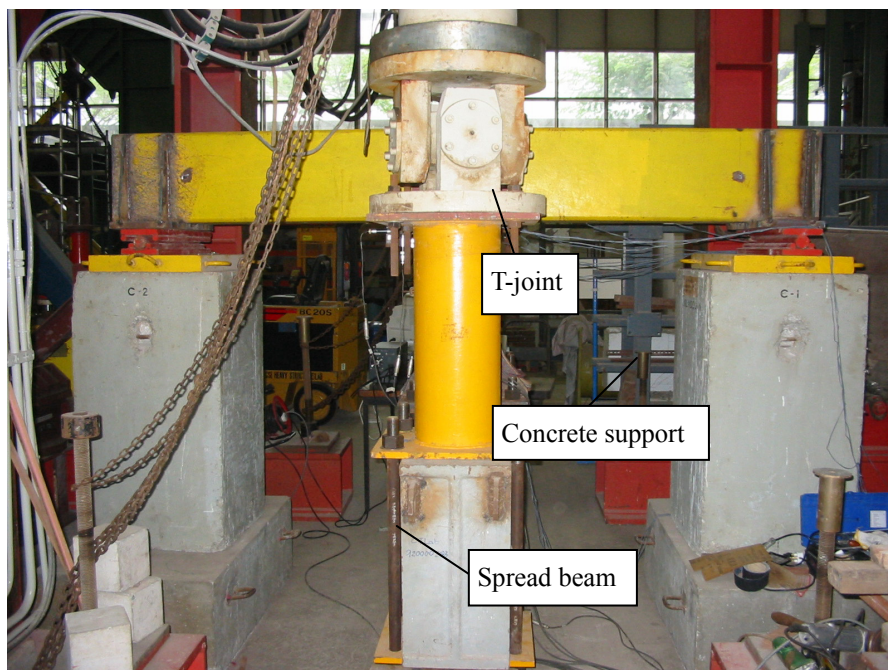
Figure 11. The Static Test Set-up
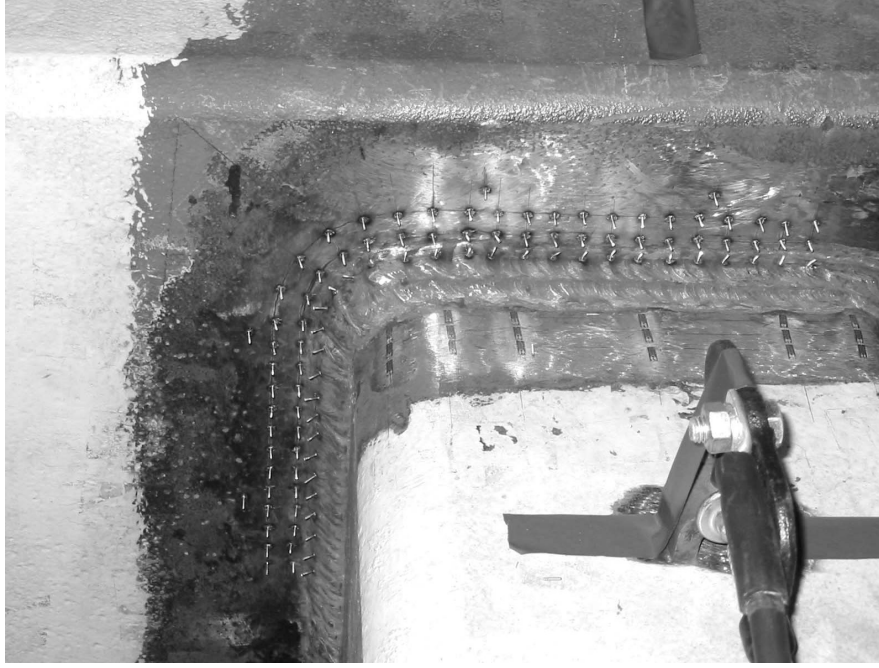
Figure 12. The Set-up of the ACPD Probes

Table 1. Dimensions of the Specimens

Specimen	b_0 (mm)	H_0 (mm)	t_0 (mm)	b_1 (mm)	h_1 (mm)	t_1 (mm)
T1	350	350	15	200	200	16
T2	350	350	15	200	200	12

Table 2. The weld and fatigue crack details

Specimen	No. of cracks	L_{c1} (mm)	L_{c2} (mm)	Crack depth a (mm)	Weld thickness t_w (mm)
T1	1	67	217	12.7	12
	2	47	92	9.0	
T2	1	77	187	13.6	12

Three LVDTs with a stroke capacity of 10 mm were used to measure the crack mouth opening displacement (CMOD) as shown in Fig. 13. One block and one bracket were attached to the chord face and brace face, and in turn three LVDTs were fixed to the bracket. The three LVDTs are in contact with the block so that the vertical displacement of point 1 and 2 and the horizontal displacement of point 3 relative to the brace can be measured accordingly. If the region between the crack and the measured point is treated as a rigid body, the displacements at the measured points are caused by the displacements and rotations of the crack faces. If the displacement measured by LVDTs 1, 2 and 3 are expressed as d_1, d_2 and l, the following relationships can be found for the calculation of CMOD,

$$\delta_{CMOD} = \sqrt{d_c^2 + l_c^2} \qquad (7)$$

$$l_c = l - \gamma \cdot h \qquad (8)$$

$$d_c = d_1 - \gamma \cdot L_1 \qquad (9)$$

where the rotation angle of the crack face can be calculated as

$$\gamma = \frac{d_2 - d_1}{L_2} \qquad (10)$$
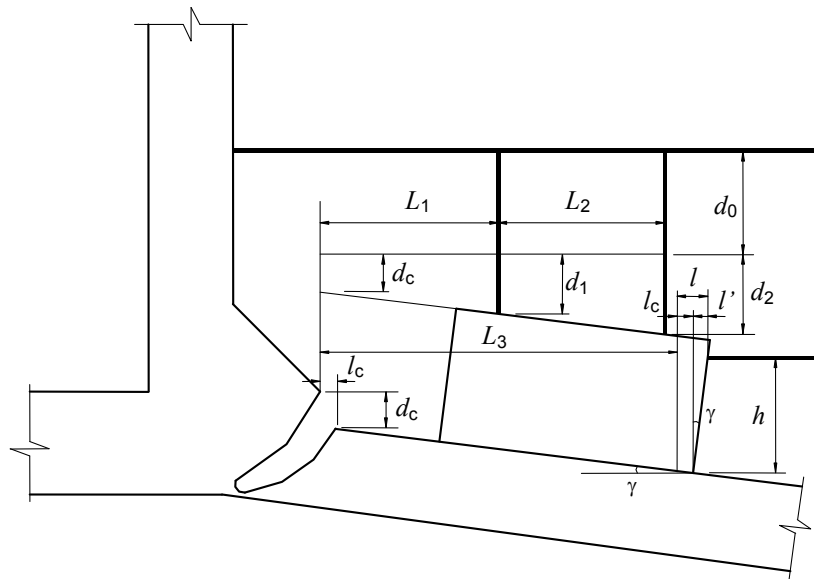
Figure 13. Measurement of the Crack Mouth Opening Displacement

5. COMPARISONS OF EXPERIMENTAL AND NUMERICAL RESULTS

Two elastic-plastic analyses are carried out on the T-joints under brace end axial loads using the ABAQUS (2002) finite element program. The dimensions of the joints and cracks are the same as those of specimens T1 and T2. Based on the proposed numerical model of the cracked RHS T-joints, the cracks are modelled using the actual crack dimensions measured from the damaged specimens as shown in Fig. 14.
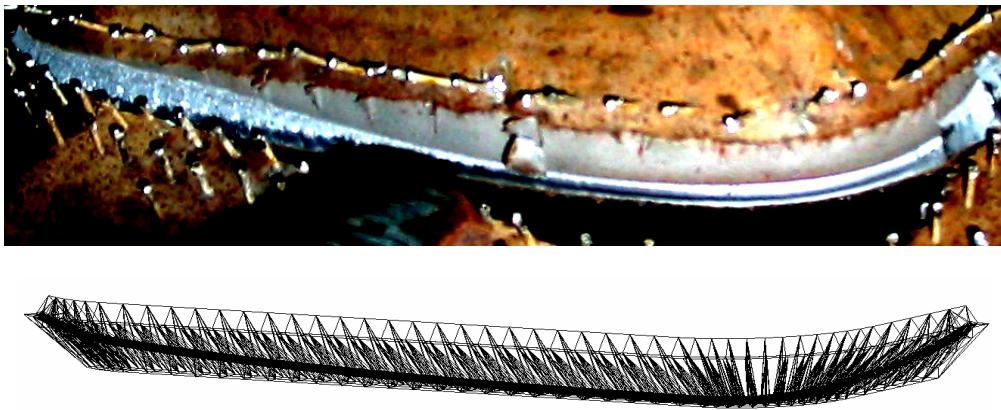
Figure 14. The Mesh of the Crack Compared with the True Crack

6 coupons were cut from the specimens and tested using the Instron 4486 universal testing machine. In accordance with the coupon tests results shown in Fig. 15, the true stress-strain curve was then obtained. In the analyses by ABAQUS [1], a piecewise multi-linear stress-strain curve approximated from the true stress-strain curve is adopted as shown in Fig. 16. The Von-Mises yield criterion and isotropic strain hardening were assumed in this analysis.
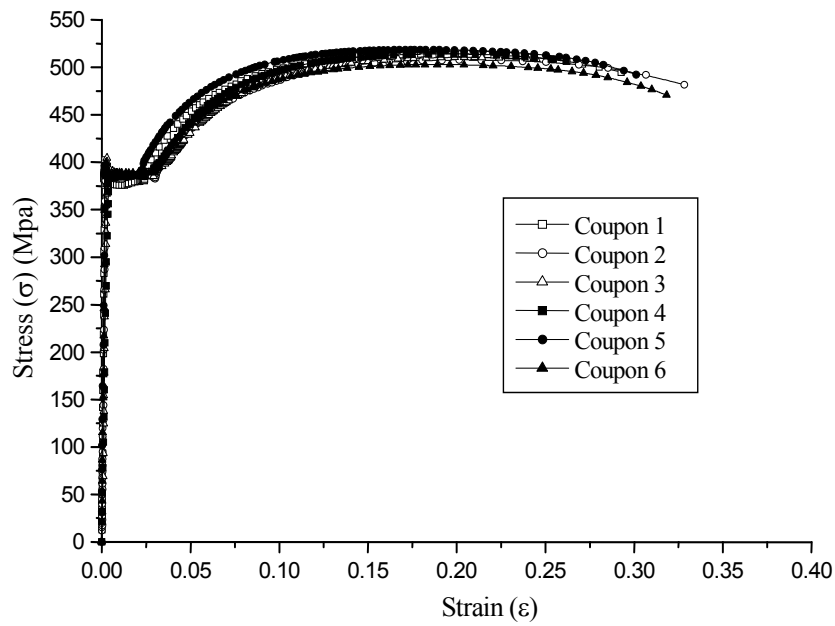
Figure 15. The Coupon Tests Results
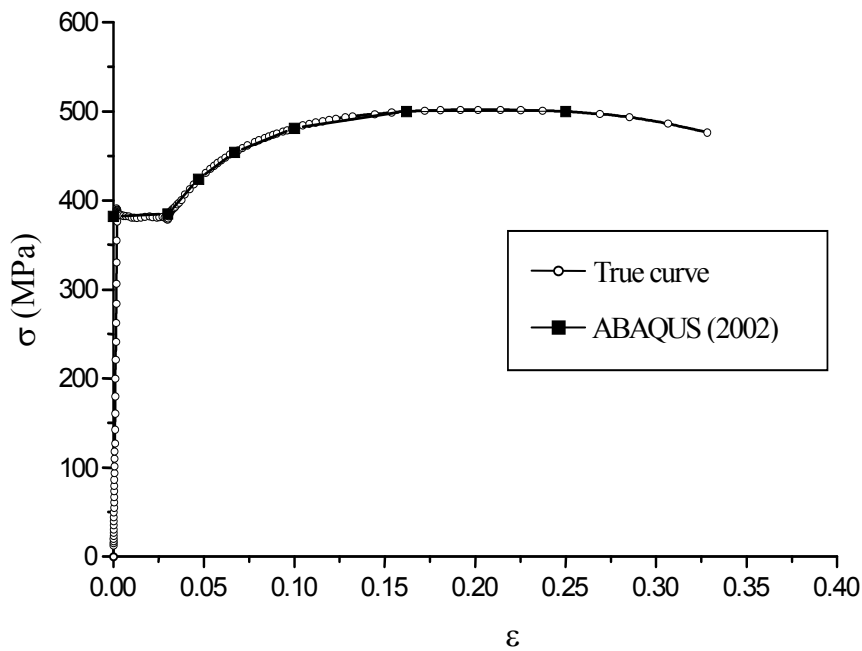
Figure 16. The Stress-strain Curve used in the Numerical Analyses

The load-displacement curves and the crack mouth opening displacements (CMOD) are calculated and compared with the experimental recordings as shown in Figs. 17 and 18. It can be found that a good agreement between the numerical and experimental results is obtained up to the failure. Therefore, it is reasonable to use the proposed numerical model to analyze the cracked SHS T-joints.
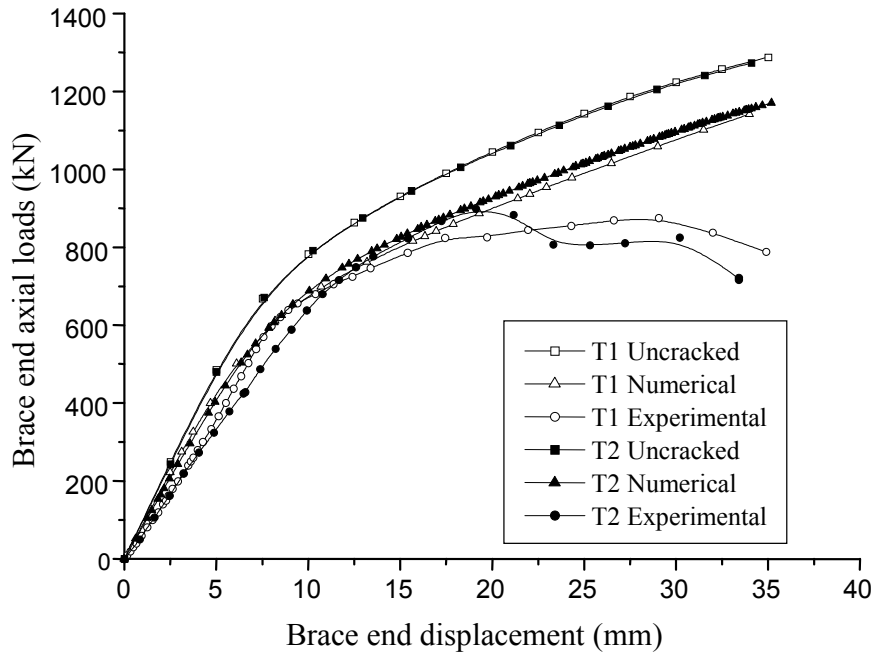
Figure 17. The Load-displacement Curves
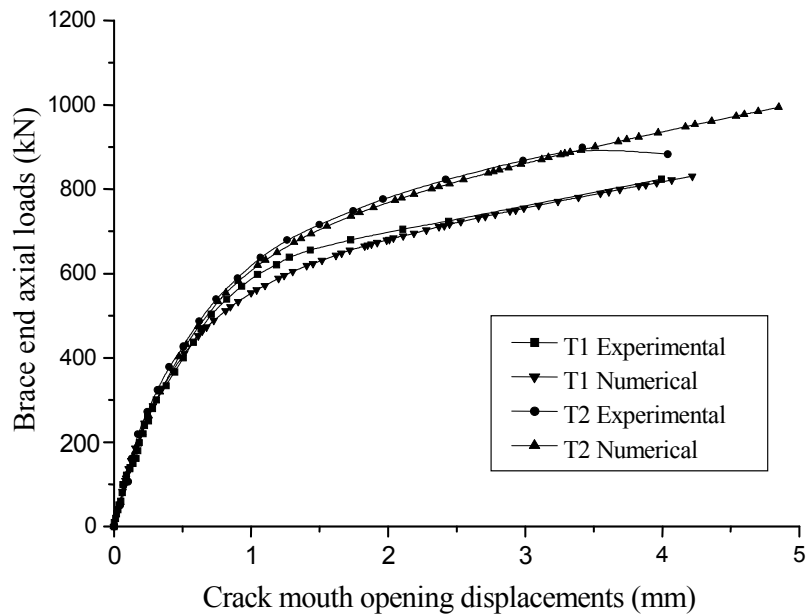
Figure 18. The Load-CMOD Curves at the Deepest Point

6. NUMERICAL CASE STUDIES

Based on the proposed numerical model, several sets of numerical cases which have different geometrical parameters and crack sizes are studied. The dimensions and crack sizes of the SHS T-joints are tabulated in Table 3. The material parameters are the same as the experimental specimens. The tension load is applied at the end of the brace under displacement control, and the two ends of the chord are pinned and connect to the ground as shown in Fig. 19. In accordance with the twice elastic compliance criterion (Cheaitani and Burdekin [6]), the plastic collapse loads of the

cracked joints are calculated and tabulated in Table 4. It can be found that the difference between the numerical results and the plastic collapse loads calculated from the Equation (6) is small. In practice, the influence of the weld width and the chord wall thickness are neglected when Equation (6) is used. Therefore, the brace to chord width ratio β is equal to $\dfrac{b_1}{b_0}$, and the brace height to chord width ratio η is equal to $\dfrac{h_1}{b_0}$. The plastic collapse loads P'_u, which neglect the weld and the chord wall thickness, are also calculated and tabulated in Table 4. It can be seen that the plastic collapse loads P'_u gives a very conservative results, and the difference between the P'_u and numerical plastic collapse load increases with increasing β ratio.
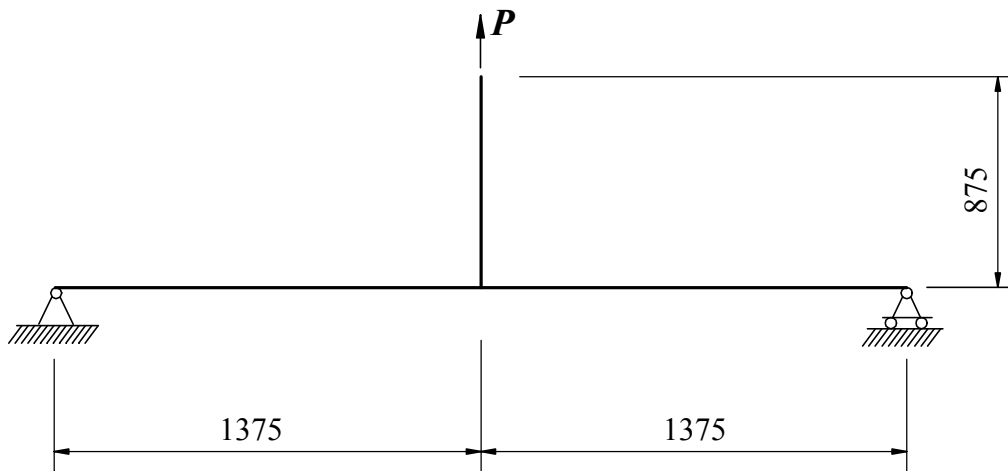
Figure 19. The Load and Boundary Conditions
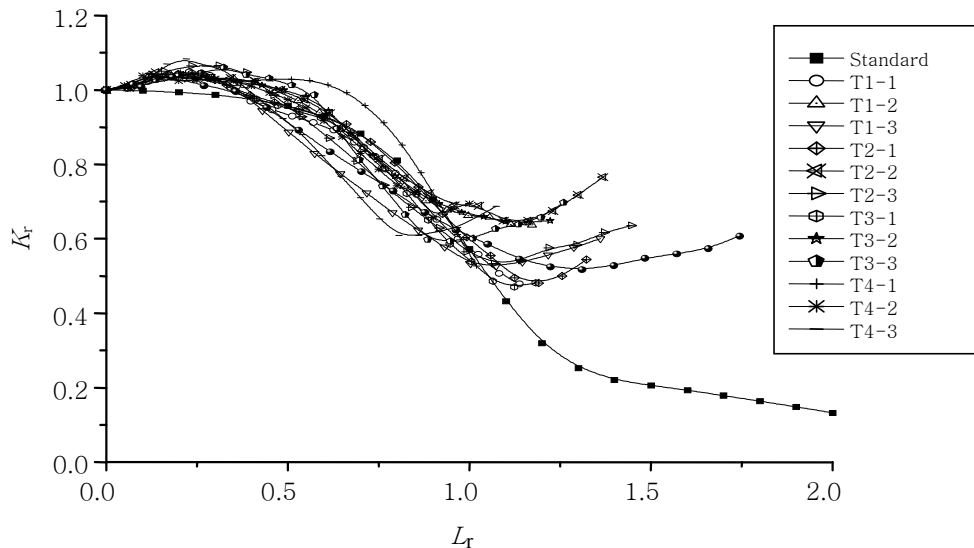
Figure 20. The Failure Assessment Curves for the SHS T-joints
(L_r = Applied Load/Numerical Collapse Load)

Table 3. The Dimensions and Crack Sizes of the SHS T-joints with Cracks

Series	b_0 (mm)	b_1 (mm)	t_0 (mm)	t_w (mm)	No.	a/t_0	l_{c1} (mm)	l_{c2} (mm)	Inclined angle θ
T1	350	150	16	8	1	0.4	33	83	30°
					2	0.6	43	108	45°
					3	0.8	63	158	45°
T2	350	200	15	8	1	0.4	38	108	30°
					2	0.6	58	128	45°
					3	0.8	68	178	45°
T3	350	200	15	12	1	0.4	42	102	30°
					2	0.6	62	132	45°
					3	0.8	72	182	45°
T4	350	250	16	8	1	0.4	63	203	30°
					2	0.6	73	223	45°
					3	0.8	93	243	45°

Table 4. The Plastic Collapse Loads of the SHS T-joints

Series	No.	Numerical (kN)	P_u (kN)	Difference	P'_u (kN)	Difference
T1	1	784.8	753.6	3.9%	646.1	17.7%
	2	762.8	738.3	3.2%	634.8	16.7%
	3	732.3	713.4	2.6%	615.9	15.9%
T2	1	975.1	921.0	5.5%	728.6	25.3%
	2	942.6	899.4	4.6%	713.8	24.3%
	3	897.4	869.5	3.1%	693.2	22.8%
T3	1	1091.1	987.8	0.9%	730.4	33.1%
	2	1050.3	961.3	0.8%	713.8	32.0%
	3	1005.4	928.7	7.6%	693.1	31.1%
T4	1	1947.1	1820.7	6.5%	1144.5	41.2%
	2	1785.6	1759.1	1.5%	1112.3	37.7%
	3	1675.5	1705.5	1,8%	1083.4	35.3%

The failure assessment curves for the numerical cases are generated using the J-integral approach. Fig. 20 shows the assessment curves constructed by using the numerical plastic collapse load as the plastic collapse load of the joints. The standard FAD curve is the BS7910 [5] Level 3A curve. It can be seen that most of the assessment curves in Fig. 20 fall inside the standard curve. Therefore the use of the standard curve is unsafe. If the standard curve is adopted to assess the strength of the cracked SHS T-joints, a conservative plastic collapse load or a safety factor should be used. As mentioned earlier, the plastic collapse load P'_u which neglects the influence of the weld and the chord wall thickness gives a conservative results, therefore, the failure assessment curves which adopt P'_u as the plastic collapse load to calculate the L_r are constructed and shown in Fig. 21. It can be seen that all of the curves fall outside or close to the standard curve. Hence, the use of the standard BS7910 [5] Level 3A curve for the assessment of the cracked SHS T-joint is safe.
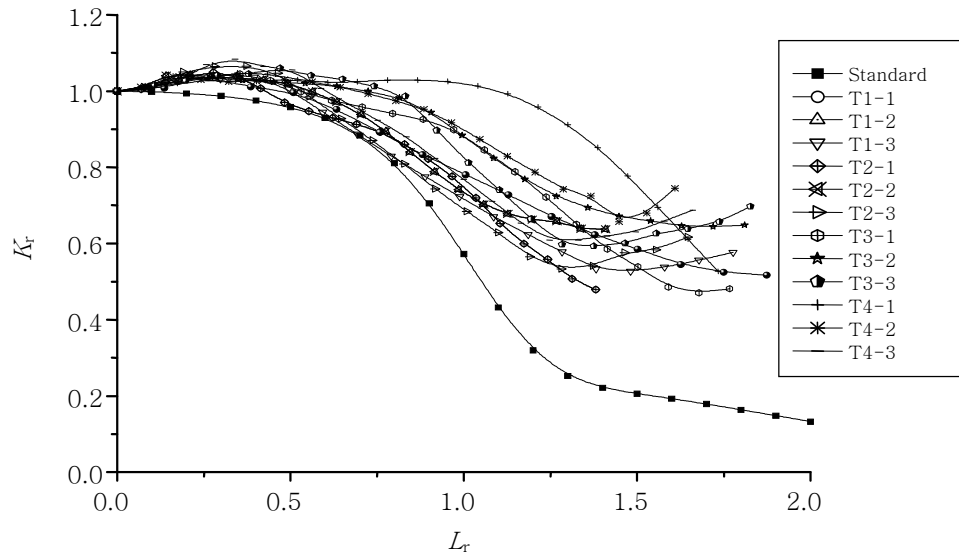
Figure 21. The Failure Assessment Curves for the SHS T-joints
(L_r = Applied Load$/P'_u$)

Using the BS7910 [5] Level 3A FAD, the fatigue-cracked specimens of T1 and T2 are assessed as shown in Fig. 22, and the calculation of the parameters K_r and L_r are tabulated in Table 5. The fracture toughness of BS 4360-50D steel were given by Hancock and Spurrier [10]. The plane strain fracture toughness δ_{IC} is about 2.7 mm on the upper shelf. The values of CTOD are derived from the experiments. It can be seen that the critical failure loads which are predicted from the failure assessment diagram are lower than the true failure loads which are recorded from the experimental tests. Therefore, the use of the standard assessment curve is safe for SHS T-joints under brace end axial loads.
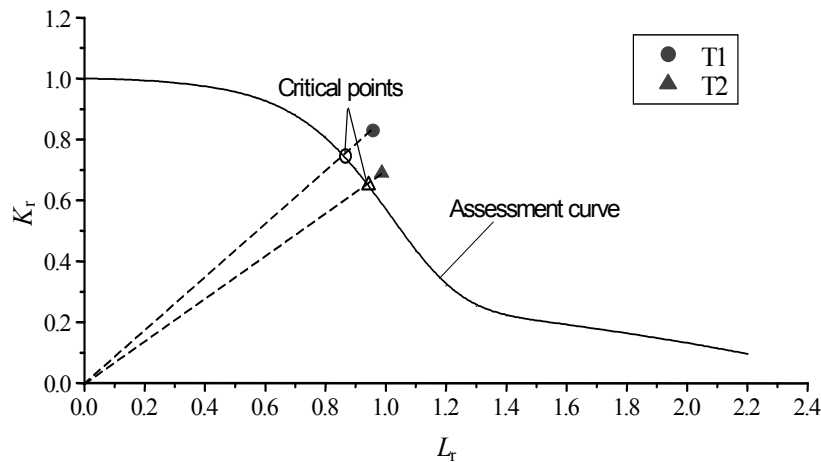
Figure 22. Failure Assessment of BS7910 (1999) Level 3A for the Specimens

Table 5. The Parameters of K_r and L_r

Specimens	δ_{IC} (mm)	δ_{CTOD} (mm)	K_r	Failure load (kN)	P'_u (kN)	L_r
T1	2.7	1.86	0.83	824.0	866.3	0.95
T2	2.7	1.29	0.69	899.0	928.1	0.97

7. CONCLUSIONS

In accordance with the yield line theory, the plastic collapse load of the cracked SHS T-joints under brace end axial loads is derived. This plastic collapse load is then validated by numerical models and experimental tests. Based on this plastic collapse load, the failure assessment diagrams (FADs) of this type of joints are constructed using the *J*-integral approach. Elastic and elastic-plastic finite element analyses have been carried out on various geometries of cracked SHS T-joints under brace end axial loads. These models contain at least one surface crack under the weld toe, and cover the following geometrical ranges of β=0.43, 0.57 and 0.71. It is found that the use of standard BS7910 (1999) Level 3A FAD is safe if the plastic collapse load is calculated using Equation (6) neglecting the influence of weld and chord wall thickness. The two full-scale specimens are then assessed, and it is concluded that the standard FAD gives a safe assessment.

Nomenclature

a	=	vertical crack depth
d_0	=	chord width
d_1	=	brace width
K	=	stress intensity factor
K_r	=	fracture ratio using stress intensity factor
l_{c1}	=	crack length along the weld toe parallel to the chord side wall
l_{c2}	=	crack length along the weld toe perpendicular to the chord side wall
L_r	=	ratio of applied load to plastic collapse load
P	=	applied load
P_u	=	plastic collapse load considering the influence of welds
P_u'	=	plastic collapse load neglecting the influence of welds
t_0	=	chord wall thickness
t_1	=	brace wall thickness
t_w	=	weld width
β	=	brace to chord width ratio
η	=	brace height to chord width ratio
γ	=	rotation angle of crack face
δ_c	=	critical crack tip opening displacement
δ_{CMOD}	=	crack mouth opening displacement (CMOD)
δ, δ_{CTOD}	=	crack tip opening displacement (CTOD)
δ_r	=	fracture ratio using CTOD parameters
σ_{e0}	=	yield stress of material
θ	=	crack inclined angle

REFERENCES

[1]   ABAQUS, "Theory Manual", Version 6.4, Hobbit, Karlsson & Sorensen Inc., USA, 2002.

[2]   Aliabadi, M.H. and Rooke, D.P., "Numerical Fracture Mechanics", Kluwer Academic Publishers, Dordrecht, The Netherlands, 1991.

[3]   American Welding Society (AWS), "ANSI/AWS D1.1: 2000 Structural Welding Code – Steel", Miami, USA, 2002.

[4]   API RP579, "Fitness-for-Service", American Petroleum Institute, Washington, USA, 2000.

[5]   BS7910, "Guide to Methods for Assessing the Acceptability of Flaws in Metallic Structures", British Standards Institution, London, UK, 2005.

[6]   Cheaitani, M.J. and Burdekin, F.M., "Ultimate Strength of Cracked Tubular Joints, Tubular Structures VI", Melbourne, Australia, A.A. Balkema-Rotterdam, 1994, pp. 607-616.

[7]   Chiew, S.P., Lie, S.T., Lee, C.K. and Ji, H.L., "Stress Analysis of Square-to-square Tubular T-joint under Combined Loads", 7th International Conference on Steel & Space Structures, Singapore, 2002, pp. 199-206.

[8]   Dover, W.D., Dharmavasan, S., Brennan, F.P. and Marsh, K.J., "Fatigue Crack Growth in Offshore Structures". Engineering Materials Advisory Services Ltd, Chameleon Press, London, UK, 1995.

[9]   Dowling, A.B. and Townley, C.H.A., "The Effect of Defect on Structural Failure: A Two-criteria Approach, International Journal of Pressure Vessels and Piping, 1975, Vol. 3, No. 2, pp. 77-107.

[10]   Hancock, P. and Spurrier, J., "The Influence of Stored Energy on the Interpretation of Fracture Test Results", Proceedings of International Conference, Fracture Toughness Testing-Methods, Interpretation and Application, The Welding Institute (TWI), Abington, Cambridge UK, 1982, Vol. 1, Paper 37.

[11]   Lapidus, L. and Pinder, G.F., "Numerical Solution of Partial Differential Equations in Science and Engineering", John Wiley and Sons Inc., New York, USA, 1982.

[12]   Packer, J.A., Wardenier, J., Kurobane, Y., Dutta, D. and Yeomans, N., "Design Guide for Rectangular Hollow Section (RHS) Joints under Predominantly Static Loading", CIDECT 3, TÜV-Verlag GmbH, Köln, Germany, 1992.

[13]   R6, "Assessment of the Integrity of Structures containing Defects", Revision 4, British Energy, Gloucester, UK, 2001.

[14]   Wardenier, J., "Hollow Section Joints", Delft University Press, Delft University of Technology, Delft, The Netherlands, 1982.

NUMERICAL IMPLEMENTATION AND CALIBRATION OF A HYSTERETIC MODEL WITH PINCHING FOR THE CYCLIC RESPONSE OF STEEL JOINTS

Pedro Nogueiro[1], Luís Simões da Silva[2,*], Rita Bento[3] and Rui Simões[4]

[1]*Department of Applied Mechanics, Polytechnic Institute of Bragança, Bragança, Portugal*
[2]*Department of Civil Engineering, University of Coimbra – Polo I, Pinhal de Marrocos, 3030 Coimbra, Portugal*
*(Corresponding author: E-mail: luisss@dec.uc.pt
[3]*Department of Civil Engineering, Instituto Superior Técnico, Av. Rovisco Pais, Lisboa, Portugal*
[4]*Department of Civil Engineering, University of Coimbra – Polo II, Pinhal de Marrocos, 3030 Coimbra, Portugal*

ABSTRACT: In this paper, a hysteretic model with pinching is presented that is able to reproduce realistically the cyclic response of generic steel joints. Secondly, the computer implementation and adaptation of the model in a spring element within the computer code SeismoStruct is described. The model is subsequently calibrated using a series of experimental test results for steel joints subjected to cyclic loading. Finally, typical parameters for the various joint configurations are proposed.

Keywords: structural engineering, steel structures, buildings, component method, beam-to-column joints, dynamic behaviour, seismic behaviour, joint model

1. INTRODUCTION

The behaviour of steel or composite joints under cyclic loading is characterized by hysteretic loops with progressive degradation of strength and stiffness that eventually lead to failure of the joint. A typical natural event that, for simplicity, is usually approximated by cyclic loading is an earthquake. Usually, seismic events provoke relatively high amplitudes of rotation in the joint area, so that steel repeatedly reaches the plastic range and the joint fails after a relatively small number of cycles. This typical behaviour is usually called oligocyclic fatigue, in close analogy with the behaviour of steel under repeated cyclic loading stressed into the plastic range (Fig. 1a).
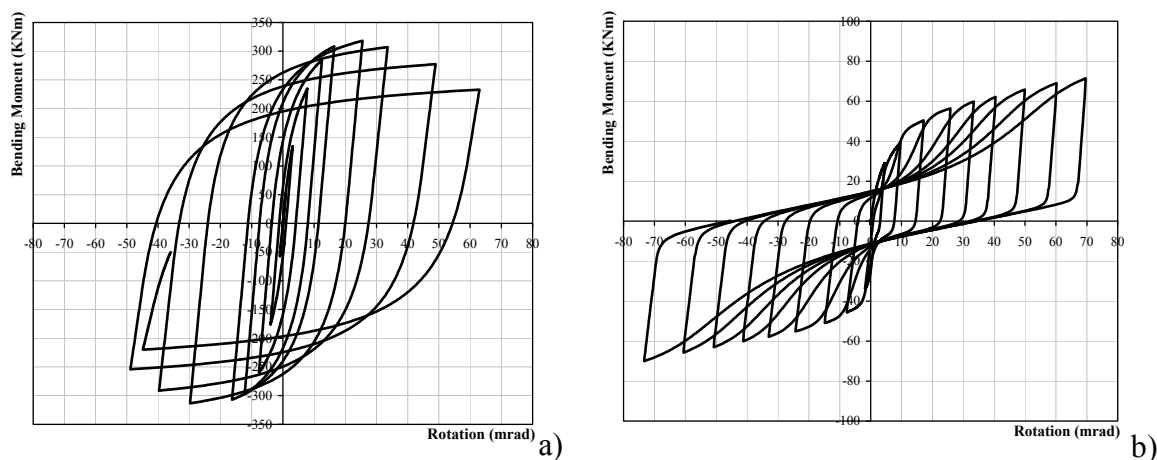
Figure 1. The Loading Branch: a) Without Pinching and b) With Pinching.

Predicting the behaviour of steel and composite joints is quite complex, because it combines several phenomena such as material non-linearity (plasticity, strain-hardening), non-linear contact and slip, geometrical non-linearity (local instability), residual stress conditions and complicated geometrical configurations. Under cyclic loading, this behaviour is further complicated by successive static loading and unloading, as illustrated in Fig. 1b, where the characteristic pinching effect in the loading branches is clearly visible. For static monotonic situations it is nowadays possible to accurately predict the moment-rotation response of a fairly wide range of joint configurations by applying the principles of the component method (Eurocode 3 [18]; Jaspart [21]). However, this is not the case for the cyclic situation. In this case, the usual approach is to develop multi-parameter mathematical expressions that are able to reproduce the range of hysteretic behaviours for a given group of steel joint typologies. Subsequently, the values of the parameters are calibrated to satisfactorily correlate to a range of section sizes for a given group of joint typologies.

Historically, two mathematical formulas have provided the basis for most of the models that have been proposed in the literature: Ramberg-Osgood type mathematical expressions (Ramberg and Osgood [38]), that usually express strain (generalized displacement) as a non-linear function of stress (generalized force) and Richard-Abbott type mathematical expressions (Richard and Abbott [39]), that usually relate generalized force (stress) with generalized displacement (strain).

Ramberg-Osgood based mathematical models were first used by Popov and Pinkey [36] to model hysteresis loops of non-slip specimens and later applied to model the skew symmetric moment-rotation hysteretic behaviour of connections made by direct welding of flanges with or without connection plate (Popov and Bertero [35]). Mazzolani [28] developed a comprehensive model based on the Ramberg-Osgood expressions that was able to simulate the pinching effect, later modified by Simões et al. [43]) to allow for pinching to start in the unloading zone. It is noted that models based on the Ramberg-Osgood expressions present the disadvantage of expressing strain as a function of stress, which clearly complicates its integration in displacement-based finite element codes (that constitute the majority of the available applications) or the direct application for the calibration and evaluation of test results, almost always carried out under displacement-control once they reach the non-linear stage.

The Richard-Abbott expression was first applied to the cyclic behaviour of joints by De Martino et al. [10]. Unfortunately, that implementation was not able to simulate the pinching effect (Simões et al. [43]). Subsequently, Della Corte et al. [11] proposed a new model, also based on the Richard-Abbott expressions, that was capable of overcoming this limitation and simulate the pinching effect, as well as strength and stiffness deterioration and the hardening effects.

Since the mid 1980's, several research projects on the cyclic behaviour of steel joints were undertaken in various research centres, comprising a total number of 39 research projects and 216 individual experimental tests. These tests are summarized in tables 1 to 5 and comprise steel joints, ranging from welded configurations to end-plate typologies. In general, the objective of these cyclic tests was the study of the seismic performance of the joints, following the observation of failures resulting from the Kobe and Northridge seismic events.

Table 1. Welded Steel Joints
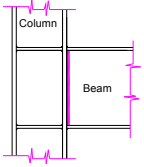
		Total number of research projects: 7 Total number of tests: 28 Total number of different load histories: 5		
Authors (date)	N.º of tests	Joint Characterization	Load History	Main parameters investigated
Popov [34]	2	Internal welded joints with beams W460x74 (W18x50) and W610x113(W24x76) column sizes with 13 mm web continuity plates.	(1)	Contribution of the panel zones and column web stiffeners (continuity plates) to joint flexibility in the post-elastic range of behaviour.
Elnashai and Elghazouli [16]	2	One half of two storey frame. Columns in H150x150x7x10, beams in H250x130x9x9 and column web stiffener with 9 mm thickness. One cyclic test and one pseudo-dynamic.	(4)	Investigate the effect of the joints rigidity on the member as well as the frame behaviour. Study the hysteretic joint behaviour.
Elnashai et al. [17]	2	Tests on external two-storey steel frames with rigid joints comprising welded beam (H250x130x9x9) to column (H150x150x7x10).	(4)	Effect of the joint stiffness and capacity on frame response. In addition, a comparison between the behaviour of frames with bolted semi-rigid and fully welded rigid joint is carried out.
Mele et al. [29]	15	Welded beam-to-column joints with beams section IPE300 and columns section HEB160, HEB200 and HEB240 sections and continuity plates 10 mm thick.	(9)	Assessment of the cyclic behaviour, influence of the column size and panel zone design.
Dubina et al. [13]	2	Welded beam (IPE360) to column (HEB300) internal joints	(2)	Initial stiffness, moment capacity and plastic rotation capacity.
Calado [8]	1	Welded steel beam (IPE300) to column (HEB200) external joint.	(2)	Cyclic behaviour, modes of failure.
Grecea et al. [20]	4	Beam-to-column internal welded joints, comprising an H or I column to two cantilever beams, without transverse stiffener in column web.	(2)	Evaluation of cyclic rotation capacity.

Table 2. Welded Flange and Bolted Web Steel Joints

	Total number of research projects: 8 Total number of tests: 38 Total number of different load histories: 6			
Authors (date)	N.º of tests	Joint Characterization	Load History	Main parameters investigated
Popov [34]	5	Internal welded flanges and bolted webs joints. W460x74(W18x50) beams and W610x113(W24x76) columns, with 19 or 13 mm column web continuity plates.	(1)	Contribution of the panel zones and column web stiffeners (continuity plates) to joint flexibility in the post-elastic range of behaviour.
Plumier and Schleich [33]	2	One external joint and one internal joint, combining bare steel elements in section HEB300 and beams in section HEA260.	(2)	Contribution of the shear panel in the energy dissipation. Study the strength and rotation capacity joint.
Tsai et al. [46]	10	External beam to wide flange column joints, using bolted web welded flange. Beams sections W21x50, W21x62, W21x83 and W21x101. All columns W14x159. 8 mm doubler plate welded to the column panel zone in the first test. All specimens have continuity plates of thickness equal to beam flange thickness.	(5)	Quality of beam-flange groove welds, strength of specimens, beam's plastic rotation capacity and effects of web-joint details.
Leon et al. [24, 25]	1	Interior joints, with beam W27x94 and the column W14x211, the panel zone incorporate four continuity plates and doubler plate on both sides of the column web.	(3)	Investigate the modes of failure in the region of the bottom flange, specially the effect of the composite concrete slab.
Lu et al. [27]	4	External joints with the flange beam (W36x150) welded to column (W14x311) and web beam bolted plate.	-	Effect of the weld metal toughness.
Stojadinovic et al. [44]	10	External joints with the flange beam welded to column and web beam bolted plates. W36x150, W30x99, W24x68 beam sizes and W14x120 to W14x257 column sizes.	(10)	Investigate the parameters beam size, panel zone strength and material properties of beam steel.
Yu and Uang [48]	4	External beam (W30x99) to column (W14x176) joints.	(11)	Evaluate the effects of the near-failure loading and extra lateral bracing.
Dubina et al. [13]	2	Welded cover plates and web cleats beam (IPE360) to column (HEB300) internal joints	(2)	Initial stiffness, moment capacity and plastic rotation capacity.

Table 3. Top and Seat Steel Joints

		Total number of research projects: 8 Total number of tests: 53 Total number of different load histories: 6		
Authors (date)	N.º of tests	Joint Characterization	Load History	Main parameters investigated
Elnashai and Elghazouli [16]	2	One half of the two storey frame. Columns in H150x150x7x10, beams in H250x130x9x9 and column web stiffener with 9mm thickness. One cyclic test and one pseudo-dynamic.	(4)	Investigate the effect of the semi-rigid joints on the member as well as the frame behaviour. Study the hysteretic joint behaviour.
Bernuzzi et al. [4]	4 + 1	External top and seat angle joints, with beam IPE300 attached to a rigid counterbeam.	(2)	In the first series study the influence of load history. The second series study the influence of the key geometrical and mechanical parameters in the cyclic performance.
Elnashai et al. [17]	5	Tests on two-storey steel frames with semi rigid joints comprising of top, seat and web angles. Beams in H250x130x9x9 and UB 254x146x31 sections and columns in H150x150x7x10 and UC 203x203x6 sections.	(4)	Effect of the joint stiffness and capacity on frame response. In addition, a comparison between the behaviour of frames with bolted semi-rigid and fully welded rigid joint is carried out.
Shen and Astaneh-Asl [42]	6	Bolted-angle beam-to-column joints, with W360x179 column size.	(7)	Inelastic behaviour under large cyclic deformation, failure modes and energy dissipation capacity.
Kukreti and Abolmaali [23]	12	Bolted top and seat angle steel joints with column W200x100 and beam sizes W360x64 and W410x67.	(8)	Approach toward formulating analytical models to predict the moment-rotation hysteresis behaviour, including the initial stiffness, ultimate moment capacity, ultimate rotation.
Abolmaali et al. [1]	20	Double web angle external joints, with the angles bolted in beam and bolted in the column and welded-bolted. W410x67 beam size and W200x100 column size.	(8)	Moment-rotation hysteresis loops and the failure modes.
Calado [8]	1	Bolted top, seat and web angle steel external joint with IPE300 beam size and HEB200 column size.	(2)	Cyclic behaviour, modes of failure.
Leon et al. [26]	2	Top, web and seat angle external joints with W460x60 beam size and W360x216 column size.	(3)	Strength, stiffness and rotation capacity.

Table 4. Bolted End-plate Steel Joints

	Total number of research projects: 12 Total number of tests: 87 Total number of different load histories: 3			
Authors (date)	N.º of tests	Joint Characterization	Load History	Main parameters investigated
Korol et al. [22]	7	External extended end plate joints with beam haunch, and with or without transverse web column stiffeners. Beams in W360x45 and W360x57, and columns in W360x64 and W360x79.	-	Seismic performance in terms of strength, stiffness, energy dissipation, and ductility. Influence of end-plate thickness, bolt pre-tension forces, column flange slenderness and column flange stiffeners.
Plumier and Schleich [33]	4	Two external joints and two internal joints, combining bare steel columns in sections HEB300 and beams in section HEA260.	(2)	Contribution of the shear panel in the energy dissipation. Study the strength and rotation capacity of the joint.
Pradhan and Bouwkamp [31]	-	High-strength bolted joints. Beams in HEA260 and columns in HEB300. Some tests are with beam and column filled-in reinforce concrete.	-	Interactive plastification of the beam-end and column shear web panel zone, shear panel thickness and contribution of the concrete.
Bernuzzi et al. [4]	4 + 5	External flush and extended end plate joints, with beam IPE300 attached to a rigid counter beam.	(2)	First series studies the influence of load history. Second series studies the influence of the key geometrical and mechanical parameters in the cyclic performance.
Adey et al. [2]	8	Extended end-plate moment joints with two beam sizes W460x97 and W610x125 and one column size W310x143. End plate with 15.9 and 19.0 mm thick.	(6)	Effect of the beam size, bolt layout, end plate thickness and extension stiffeners.
Yorgun and Bayramoglu [47]	4	Bolted fabricated beam-to-column end-plate joints. (110x195) for beam and (160x135) column sizes.	(2)	Effect on cyclic load of the gap between the end plate and the column flange on the performance of the joint.
Dubina et al. [13]	2	Bolted with extended end plate beam (IPE360) to column (HEB300) internal joints	(2)	Initial stiffness, moment capacity and plastic rotation capacity.
Dubina et al. [14]	4	Bolted steel double-sided extended end-plate beam to column joints.	(2)	Evaluate the performance of the beam-to-column extended end plate, and numerical modelling of joints.
Broderick and Thomson [5]	6	Flush end-plate steel external joints. UC 203x203x86 column sizes, 254x102x22UB and 254x146x37 UB beam sizes.	(2)	Stiffness, moment capacity, rotation capacity and hysteretic behaviour.
Bursi et al. [7]	18	Bolted steel double-sided extended end-plate beam to column external joints. IPE300 beam size, HEA180, HEB180 and HEA280 column sizes.	(2)	Joint geometry and loading history.
Summer and Murray [45]	6	Bare steel double extended end-plate beam-to-column external joints. Four combinations beam/column: W24x68/ W14x120, W30x99/W14/193 W36x150/W14x157, W24x68/W14x257.	(11)	Influence of the extended-end-plate in the strength, stiffness and joint ductility.
Dunai et al. [15]	19	Bolted end-plate joints with or without encased column. Columns in HEA200 or welded (6mm) changing the end plate thick, class and bolt diameters.	(2)	Study and characterise the typical cyclic behaviour failure modes of this type of joints.

Table 5. Dog Bone Beam Flange Welded Steel Joints

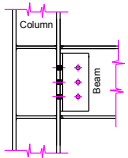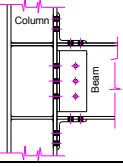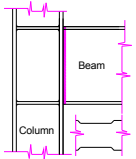|				
		Total number of research projects: 2 Total number of tests: 10 Total number of different load histories: 1		
Authors (date)	N.º of tests	Joint Characterization	Load History	Main parameters investigated
Plumier and Schleich [33]	4	Two exterior joints and two interior joints, combining bare steel columns in sections HEB300 and beams in section HEA260.	(2)	Contribution of the shear panel in the energy dissipation. Study the strength and rotation capacity joint.
Chen and Chu [9]	5+1	Five external joints with the beam (H600x300x12x20) flanges welded to the box column (500x500x20x20), and web beam bolted plates. One-storey steel frame.	-	Examine the seismic resistance characteristics of the beam-to-column assemblies.

The cyclic loads histories recorded in these tests, eleven in total, are summarized in Table 6.

Table 6. Cyclic Load Histories

Load History	N.º of tests	Description
(1)	7	Typical cyclic loading sequence which induced cyclic displacement exceeded the elastic range.
(2)	87	ECCS procedure.
(3)	3	Full reversal cycles at 0.1, 0.25, 0.50, 0.75, 1.0, 1.5, 2.0 and 3.0% interstorey drifts.
(4)	11	Based in the second-storey yield displacement (δ_y), three cycles were applied at each displacement of δ_y, $2\delta_y$, $4\delta_y$, $6\delta_y$, etc.
(5)	10	Cyclically increasing displacements of 6 mm at the cantilever end, between each cycles.
(6)	8	Applied Technology Council Guidelines for Testing of Components of Steel Structures (ATC-24 1992).
(7)	6	Three phases of loading history: displacement increased to 5-10 mm to 15-20 mm, then decreased to the starting displacement.
(8)	32	Three cycles of 4.45 KN loops, three cycles of 8,9 KN loops, three cycles of 13.35 KN loops, two cycles of 17.8 KN loops.
(9)	15	Four different load history, defined in terms of applied beam tip displacement (d), yield displacement d_y (d/d_y) and interstorey drift angle (d/H) and one more load history according to the ECCS procedure.
(10)	10	5 cycles of 0.375% of drifts, 5 cycles of 0.5 %, 5 cycles of 0,75%, 3 cycles of 1%, 2 cycles of 0.5%, 2 cycles of 1.5%, 2 cycles of 0.5%, 2 cycles of 2%, 2 cycles of 0.5%, 2 cycles of 3%, 2 cycles of 0.5%, 2 cycles of 4%, 2 cycles of 0.5%, 2 cycles of 5%, 2 cycles of 0.5% and 8 cycles of 5%.
(11)	10	SAC standard and SAC near-fault loading history.

Previous work by the authors (Nogueiro et al. [30]) investigated the effect of pinching on the seismic response of steel frames and concluded that it leads to a variation of about 20% of the joint rotation, thus increasing the ductility demand on the joints to avoid failure. It is the objective of this paper: (i) to present a hysteretic model with pinching based on the Richard-Abbott mathematical model and developed by Della Corte et al. [11]; (ii) to describe the computer implementation and

adaptation of the model in a spring element within the computer code SeismoStruct (SeismoStruct [41]; (iii) to apply and calibrate the model with a series of experimental test results for steel joints subjected to cyclic loading; and (iv) to compare and propose typical parameters for the chosen joint configurations.

2.   MODIFIED RICHARD-ABBOTT MODEL

The modified Richard-Abbott model was developed by Della Corte et al. [11], to include pinching. According to this model, the loading curve for a generic branch of the moment-rotation curve of a joint is given by the following equation:

$$M = M_n - \frac{(k_a - k_{pa}) \cdot (\phi_n - \phi)}{\left[1 + \left|\frac{(k_a - k_{pa}) \cdot (\phi_n - \phi)}{M_{0a}}\right|^N\right]^{1/N}} - k_{pa} \cdot (\phi_n - \phi) \tag{1}$$

where $M_{0a} = M_n + M_{0p}$. The unloading curve is obtained in the same way, replacing (M_n, ϕ_n) by (M_p, ϕ_p) and the parameters M_{0a}, k_a and k_{pa} by the corresponding values evaluated at unloading, M_{0d}, k_d and k_{pd}.
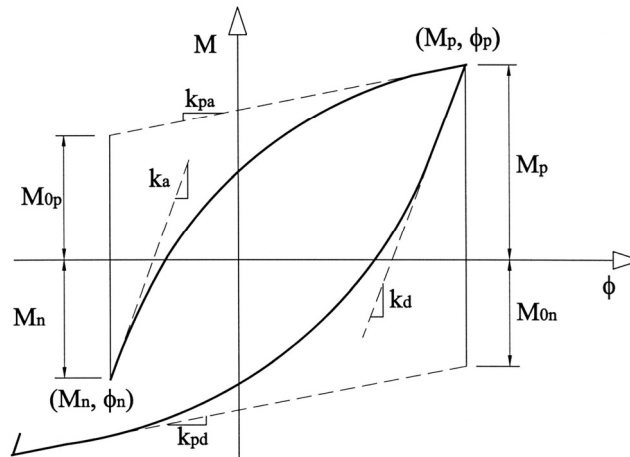
Figure 2. Generic Loading and Unloading Branches

To describe the pinching phenomenon, two limit curves are introduced, that represent a lower and an upper bounds to possible M-ϕ values. Both curves have a Richard-Abbott type law, and are characterised by parameters K_{op}, M_{op}, K_{hp}, n_p (lower bound curve) and K_o, M_o, K_h, n (upper bound curve). Additionally, any generic point (M, ϕ) along the real path is also considered to belong to a Richard-Abbott type curve, where the relevant parameters are defined as follows:

$$K_{ot} = K_{op} + (K_o - K_{op}) \times t \tag{2a}$$
$$M_{ot} = M_{op} + (M_o - M_{op}) \times t \tag{2b}$$
$$K_{ht} = K_{hp} + (K_h - K_{hp}) \times t \tag{2c}$$
$$n_t = n_p + (n - n_p) \times t \tag{2d}$$

The parameter t, ranging in the interval [0,1], defines the transition law from the lower bound to the upper bound curve. It must reproduce, as closely as possible, the shape of the experimental curves and is given by:

$$t = \left[\frac{(\phi/\phi_{\lim})^{t_1}}{(\phi/\phi_{\lim})^{t_1}+1}\right]^{t_2} \tag{3}$$

where t_1, t_2 and ϕ_{lim} are three experimentally calibrated parameters. Figure 3 illustrates, qualitatively, the resulting pinching behaviour with reference to one single excursion from the origin.

$$M = \frac{(K_{ot}+K_{ht})\times\phi}{\left[1+\left|\dfrac{(K_{ot}+K_{ht})\times\phi}{M_{ot}}\right|^{n_t}\right]^{\frac{1}{n_t}}} + K_{ht}\times\phi \tag{4}$$
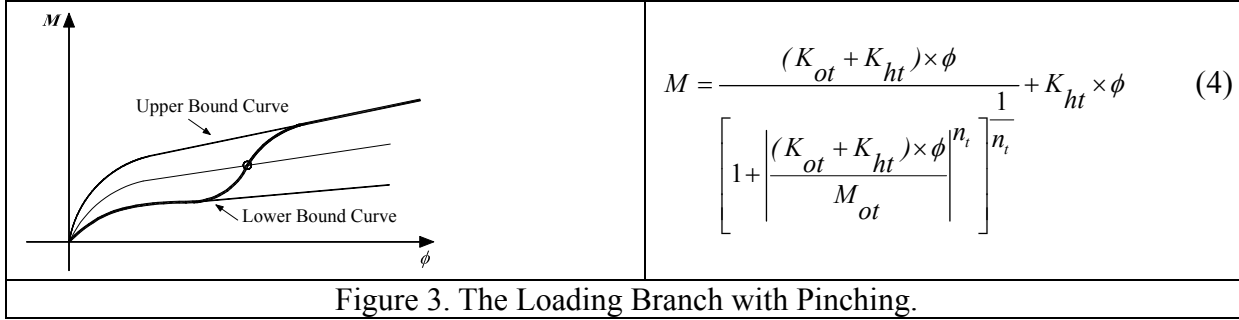
Figure 3. The Loading Branch with Pinching.

In case of a generic deformation history, the parameter ϕ_{lim} is related to the maximum experienced deformation in the direction of the loading branch to be described. It is evaluated according to the following relationship:

$$\phi_{\lim} = C\left(\left|\phi_o\right| + \phi_{\max}\right) \tag{5}$$

where $\left|\phi_o\right|$ is the absolute value of the deformation corresponding to the starting point of the current excursion, $\phi_{\max}$ is the maximum absolute value of the deformation experienced in the previous loading history, in the direction of loading branch to be described (Figure 4a) and C is a calibration parameter. The unloading branch is assumed to be linear with a slope equal to the initial stiffness K_o up to the interception with the straight line obtained drawing a parallel to the hardening line going through the origin. This allows the Bauschinger effect to be considered.

a)

b)
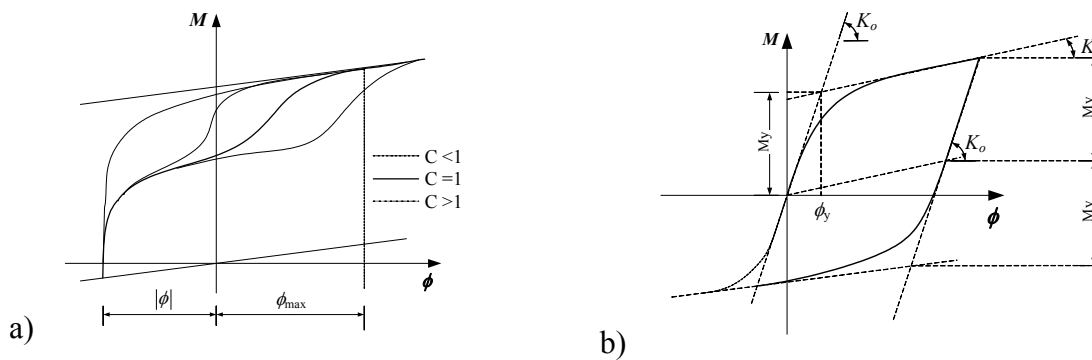
Figure 4. a) Effect of Parameter C; b) Definition of the Unloading Branch.

Cyclic action in the inelastic range produces accumulation of plastic deformation, until ductility of the system is locally exhausted and failure occurs due to fracture. In some cases, the repetition of loading is accompanied by degradation of the structural response because of deterioration of its mechanical properties. This can be taken into consideration both for strength ($M_{o,red}$) and stiffness ($K_{o,red}$) using the following expressions:

$$M_{o,red} = M_o\left(1 - i_M \times \frac{E_h}{M_y \times \bar{\phi}_{u,o}}\right) \tag{6}$$

$$K_{o,red} = K_o \left(1 - i_K \times \frac{E_h}{K_o \times \bar{\bar{\phi}}_{u,o}} \right).$$

$\bar{\bar{\phi}}_{u,o}$ is the corresponding ultimate value in the case of one single excursion from the origin (monotonic loading), E_h is the hysteretic energy accumulated in all previous experienced excursions, M_y represents the conventional yield resistance of the joint, K_o the initial stiffness as defined in the Figure 4b and coefficient i is an empirical parameter related to damage rate.

Hardening due to cyclic plastic deformation is considered to be isotropic. Besides, experimental results of constant deformation amplitude tests for joints not exhibiting strength deterioration show that cyclic hardening grows up in few cycles and then becomes stable. Therefore, the following assumption is made:

$$
\begin{aligned}
M_{o,inc} &= M_o && \text{if } \phi_{max} \leq \phi_y \\
M_{o,inc} &= M_o \left(1 + H_h \times \frac{\phi_{max} - \phi_y}{\phi_y} \right) && \text{if } \phi_{max} \geq \phi_y
\end{aligned}
\tag{7}
$$

M_o and $M_{o,inc}$ are the initial and increased value of strength, respectively; ϕ_{max} is the maximum value of deformation reached in the loading history (in either positive or negative direction); ϕ_y is the conventional yielding value of deformation (see Figure 4b); H_h is an empirical coefficient defining the level of the isotropic hardening (Filippou et al. [19]). The above formulation practically corresponds to translate the asymptotic line of the original Richard-Abbott equation (De Martino et al. [10]), as a function of the extent of the plastic deformation.

3.   COMPUTATIONAL IMPLEMENTATION

The numerical implementation of the hysteretic model described above was carried out using the Delphi (Delphi 7 [12]) development *platform*. A six degree-of-freedom spring element was implemented in the structural analysis software SeismoStruct [41]. The implementation comprised two major parts. The first consists of the management of the hysteretic cycles, where a clear distinction between positive and negative moment must be made because of possible asymmetry of joint response under hogging or sagging bending. An illustrative flowchart of the cycle management is shown in Figure 5.
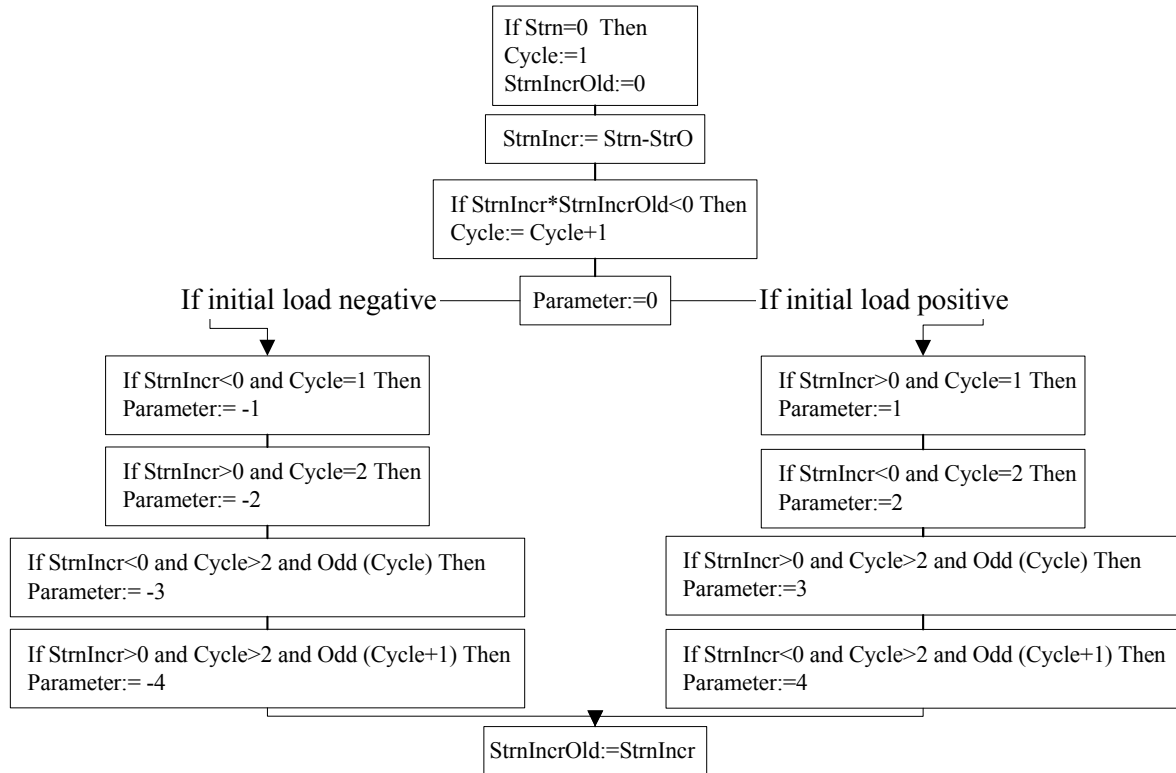
Figure 5. Flowchart for the Management of Hysteretic Cycles.

The second part of the implementation relates to the development of the code for each cycle. Several possibilities must be considered, depending on the starting bending moment (positive or negative) and the sign of the strain increment (positive or negative), as can be seen in the figure 6a, b and c.
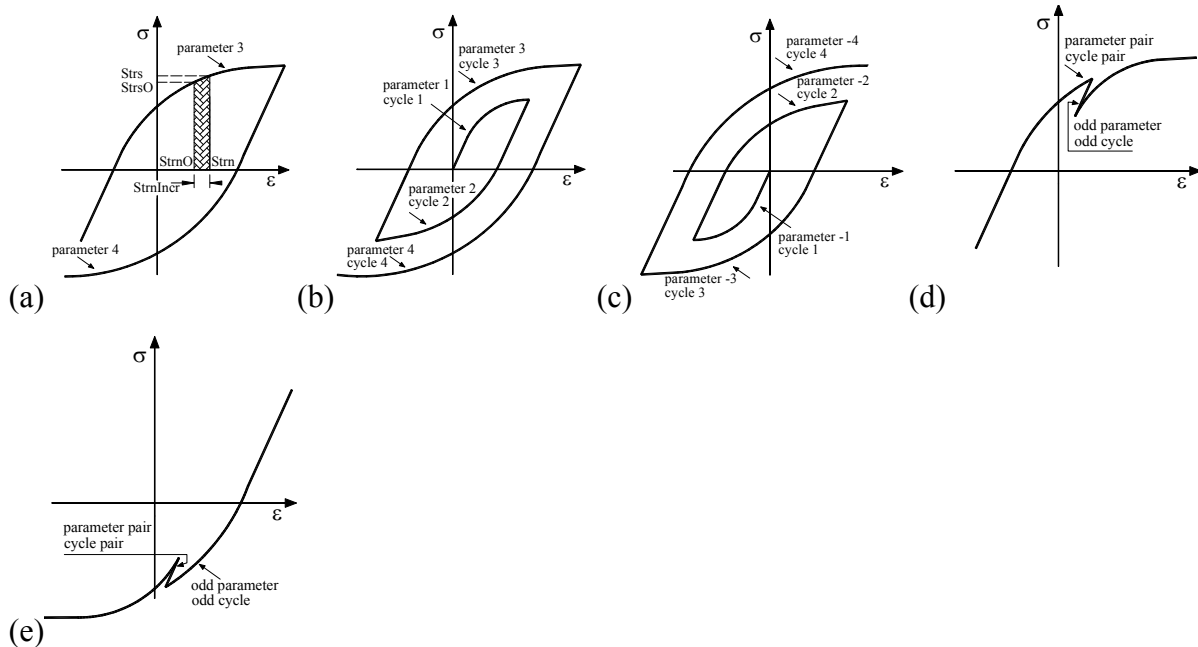
Figure 6. a) Definition of the Increment; b) Hysteretic Curve for Positive Starting; c) Hysteretic Curve for Negative Starting; d) Small Loading for Odd Parameters, e) Pair Parameters.

In total, 30 parameters have to be defined for this model, fifteen for the ascending branches (subscript a) and fifteen for the descending branches (subscript d): K_a (and K_d) is the initial stiffness, M_a (and M_d) is the moment resistance, K_{pa} (and K_{pd}) is the post limit stiffness, n_a (and n_d) is the shape parameter, all these for the upper bound curve (see figure 1), K_{ap} (and K_{dp}) is the initial stiffness, M_{ap} (and M_{dp}) is the strength, K_{pap} (and K_{pdp}) is the post limit stiffness, n_{ap} (and n_{dp}) is the shape parameter, all these for the lower bound curve, t_{1a} and t_{2a} (and t_{1d} and t_{2d}) are the two parameters related to the pinching, C_a (and C_d) is the calibration parameter related to the pinching, normally equal to 1 (see figure 4a), i_{Ka} (and i_{Kd}) is the calibration coefficient related to the stiffness damage rate, i_{Ma} (and i_{Md}) is the calibration coefficient related to the strength damage rate, H_a (and H_d) is the calibration coefficient that defines the level of isotropic hardening and E_{maxa} (and E_{maxd}) is the maximum value of deformation.

The model had to be prepared to work with any kind of loads, especially for the seismic action where loading and unloading branches can be either large or small. So, the model must be prepared to consider a reversal of loading like the one presented in Figure 6d and e, for both positive and negative starting points.

To illustrate the application and versatility of the model, it was first tested on a typical steel joint with its properties defined in Table 7, considering stiffness and strength deterioration but no hardening.

Table 7. Joint Parameters

K_a KNm/rad	M_a KNm	K_{pa} KNm/rad	n_a	K_{ap} KNm/rad	M_{ap} KNm	K_{pap} KNm/rad	n_{ap}	t_{1a}	t_{2a}	C_a	i_{Ka}	i_{Ma}	H_a	E_{maxa} rad
34440	116	1700	2	34440	60	1700	1	10	0.15	1	15	0.01	0	0.1
K_d KNm/rad	M_d KNm	K_{pd} KNm/rad	n_d	K_{dp} KNm/rad	M_{dp} KNm	K_{pdp} KNm/rad	n_{dp}	t_{1d}	t_{2d}	C_d	i_{Kd}	i_{Md}	H_d	E_{maxd} rad
44440	136	1700	2	44440	80	1700	1	10	0.15	1	15	0.01	0	0.1

Firstly two monotonic loadings were considered, one positive and another negative. Subsequently, two distinct cyclic load histories were applied (ECCS load history and a random load history). The results, illustrated in Figure 7, show that, for low rotations ($< \theta_y$), the cyclic results coincide with the monotonic results. With increased rotation, the cyclic response deviates from the monotonic response because of strength and stiffness deterioration.
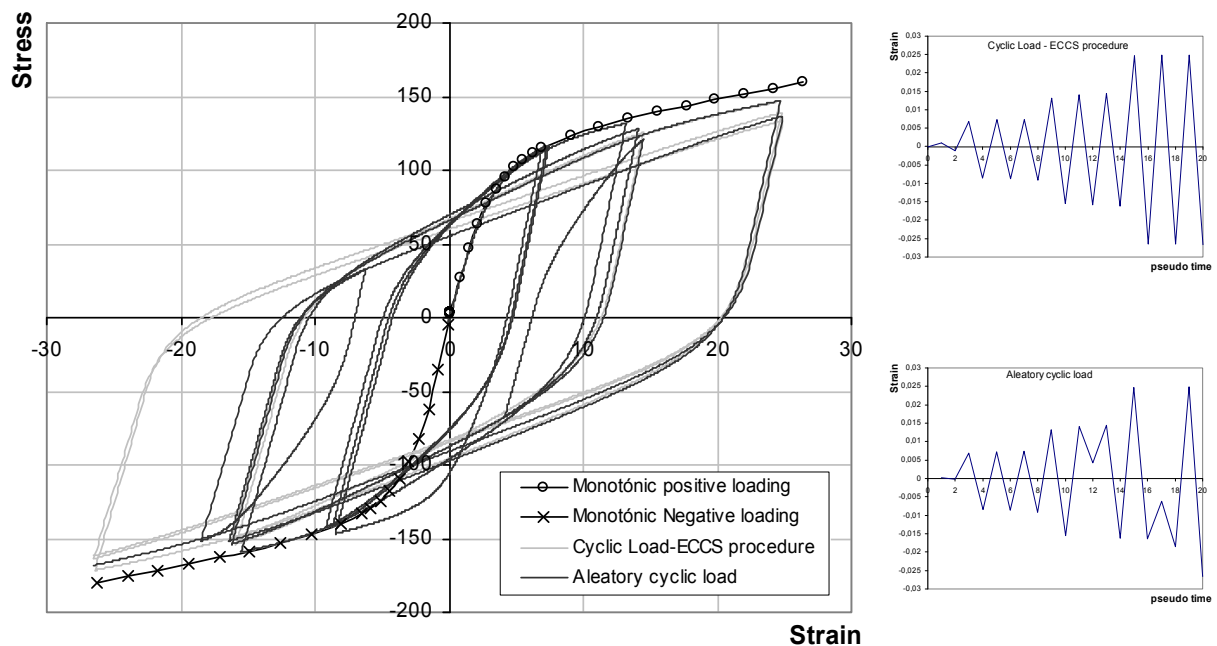
Figure 7. Hysteretic and Monotonic Curves.

4.   APPLICATION AND VALIDATION

4.1   Description of the Experimental Tests

In order to establish reliable parameters for a range of end-plate or cleated beam-to-column steel joint configurations and to validate the accuracy of the model, a group of well-documented experimental results were selected from tables 1 to 8. These tests were performed by Bernuzzi et al. [4], Elnashai et al. [17], Korol et al. [22], Broderick et al. [5], Bursi et al. [7] and Abolmaali et al. [1] and are summarized in Table 8, corresponding to extended end-plate, flush end-plate, top and seat and web cleat connections.

Table 8. Experimental Tests

Nº	Test Ref.	Authors	Typology	Beam	Column	Bolts	Thickness plate	K^+_y KNm/rad	K^-_y KNm/rad
1	EPBC-1	Bernuzzi et al.	Extended	IPE300	"Rigid plate"	M20	12 mm	78000	97500
2	JB1-3A	Bursi et al.	Extended	IPE300	HEB180	M20	18 mm	35000*	35000*
3	A2	Korol et al.	Extended	W360x45	W360x64	Ø 25	25.4 mm	63751	63741
4	A3	Korol et al.	Extended	W360x45	W360x79	Ø 25	19.0 mm	79370	79370
5	FPC/D	Bernuzzi et al.	Flush	IPE300	"Rigid plate"	M20	12 mm	19000	30500
6	EP4	Broderick et al.	Flush	254x146x37UB	203x203x86UC	M20	12 mm	3550	3550
7	EP2	Broderick et al.	Flush	254x102x22UB	203x203x86UC	M20	12 mm	10210	10210
8	CS01	Elnashai et al.	Top and Seat	254x146x31UB	203x203x6UC	Ø 16	8 mm	4300	4300
9	CS02	Elnashai et al.	Top and Seat	254x146x31UB	203x203x6UC	Ø 16	12 mm	7500	7500
10	CS03	Elnashai et al.	Top and Seat	254x146x31UB	203x203x6UC	Ø 16	15 mm	9800	9800
11	TSC/D	Bernuzzi et al.	Top and Seat	IPE300	"Rigid plate"	M20	12 mm	12800	20100
12	DW-WB 4	Abolmaali et al.	Web cleat	W410x67	W200x100	Ø 19	10 mm	32263	32263
13	DW-WB 5	Abolmaali et al.	Web cleat	W410x67	W200x100	Ø 19	19 mm	16254	16254

* Estimated value

The description of the tests starts with the extended end-plate connection tests performed by Bernuzzi et al. [4], Bursi et al. [7] and Korol et al. [22].

The study developed by Bernuzzi et al. had two series of tests on beam-to-column joints under cyclic loading. The first series of tests aimed at investigating the influence of the loading history on the joint performance. The second series of tests was subsequently performed with the goal of setting the key parameters enabling a full description of the connection response, including the energy dissipation capability. From this study only three tests were chosen. The first test, referred to as EPBC-1, considers end-plates extended on both sides of the beam, as shown in Figure 8a. The plate extension ensures a noticeable increase in stiffness and strength, when compared with the others tests FPC/D and TSC/D from the same author (Table 8), later discussed. Failure occurred in the weld of the extended plate. The second test, also an end-plate extended both sides but with 18 mm plate thickness, was performed by Bursi et al. (Figure 8b) and results in an increase of strength; therefore the hysteretic response is quite different, as can be observed in Figure 12. Similarly, the failure mode was at weld toe, in the end plate, starting with a ductile crack at the steel surface owing to plastic strains, a stable growth of a ductile crack in the plate thickness followed by a sudden propagation of the crack in a brittle fracture mode.

Tests number 3 and 4 (Table 8), performed by Korol et al., are also extended end-plate connections, but with transverse stiffeners in the column web, as well in the end-plate, as can be seen in Figure 8c. These are stronger joints, without slippage, but much more influenced by stiffness and strength deterioration. Both exhibited failure by beam local buckling, the column flange being the first yielded component for test A2 (test number 3) and the beam web buckling for test A3 (test number 4).

Figure 8. a) Geometrical Representation of Joints 1, b) Joint 2, c) Joints 3 and 4.
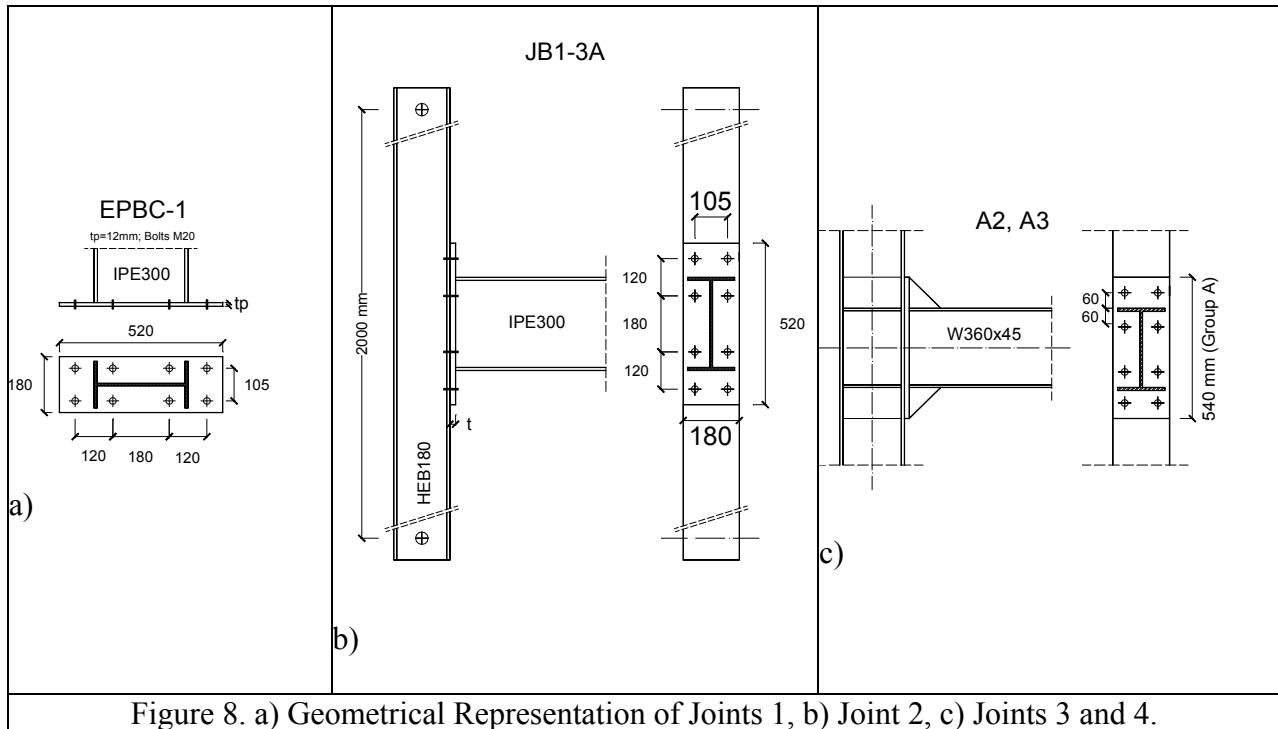
The second group of tests corresponds to flush end plate joints (test numbers 5 to 7, Table 8). The first test from this group was performed by Bernuzzi et al., and the other two by Broderick et al. The corresponding geometrical characteristics are presented in Figure 9a and 9b, respectively. In the FPC/D tests, the endplate played the most important role in the deformation, while the bolts exhibited a negligible contribution. The plastic deformation is mainly concentrated in the end plate and the failure mode was finally related to weld fracture in the internal part of the beam flange.

Figure 9. a) Geometrical Representation of Joints 5, b) Joints 6 and 7.
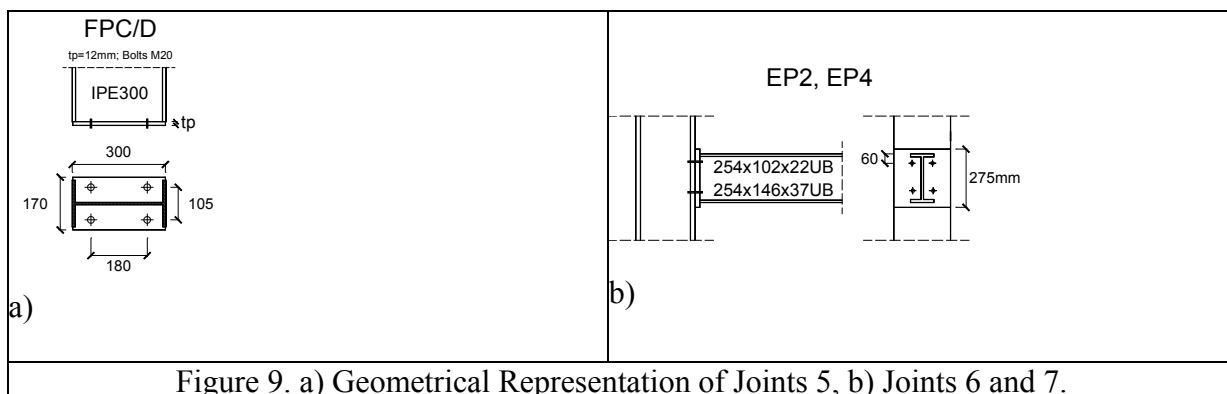
The next four tests were performed by Elghazouli et al. and Bernuzzi et al. and the geometrical representation of joints are shown in Figure 10. For the first three tests (Figure 10a), top, seat and web cleat connections, an axial load of 400 kN was applied to the column, which represents 29% of the column section plastic capacity. The CS01 joint is the most flexible and with lesser resistance and has a relatively low-energy dissipation capacity. The CS02 connection is stronger, with higher

stiffness. The CS03 has the strongest and the most stiffened connection. For all cases, the strains on the web of the connection panel zone were measured and the values were well below yield. These connections have no slippage. The TSC/D test is a top and seat connection and the failure mode is governed by the plastic deformation of the flange cleats (including hole ovalisation) and by the fracture of one bolt for large deformations, after 60 mrad, which is not recommended for seismic design.
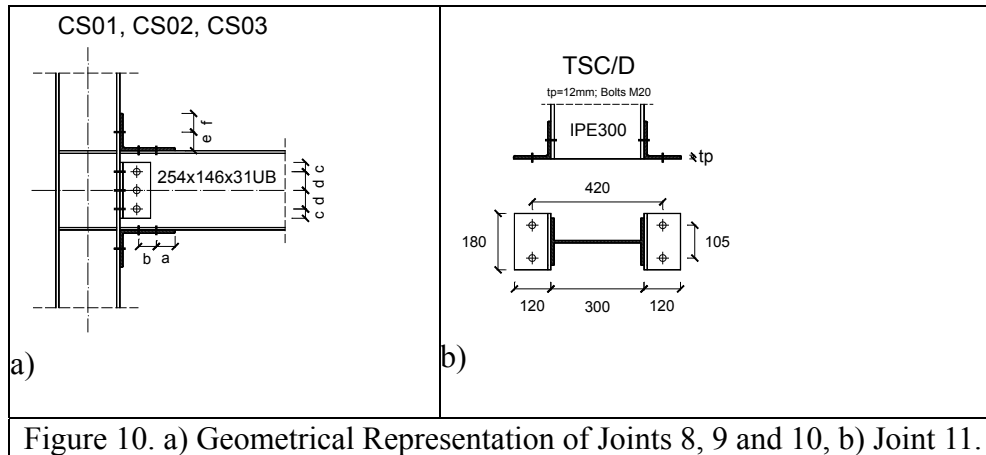
Figure 10. a) Geometrical Representation of Joints 8, 9 and 10, b) Joint 11.

Finally, the last two tests, DW-WB4 and DW-WB5, are web cleat connections (Figure 11) and were performed by Abolmaali et al.. This type of joints are very much influenced by slippage, which leads to a low rate of energy dissipated. In his study, Abolmaali et al. presented the cyclic behaviour of two series of tests corresponding to two types of semi-rigid double web cleat connections: bolted-bolted and welded-bolted (cleats welded to the beam web and bolted to the column flange), with pre-tensioned bolts, as can be seen in Figure 11. The first series of tests was rejected because of inappropriate seismic behaviour. In the second series of tests only two tests were chosen from the eight performed, respectively test DW-WB numbers 4 and 5, which exhibited yielding of the angles as the failure mode.
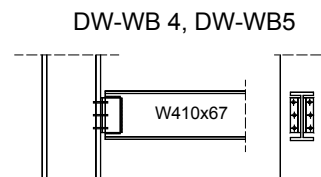
Figure 11. Geometrical Representation of Joints 12 and 13.

4.2   Application of the Modified Richard-Abbot model

This section presents the results of the application of the modified Richard-Abbott model to the selected tests. It is noted that almost all of the experimental curves presented in this work were rebuilt by means of the curves published in the corresponding papers, a process that can lead to some errors. The accuracy of this process dictated the selection of the tests where, whenever possible, at least one test per typology was chosen, based on the type of the mode failure.

Firstly, the figures overlaying, for each experimental hysteretic curve, the numerical curve obtained using the modified Richard-Abbott model are presented. Then, a comparison between both curves in terms of dissipated energy and moment resistance for each cycle is also presented. Finally, Tables 9 and 10 show the parameters chosen in the Richard-Abbott model, for the ascending and descending branches.

For the first two tests, with similar geometrical properties, the corresponding moment-rotation curves are shown in Figure 12. Joint number 1 has more stiffness and pinching, and has also more stiffness and strength deterioration than joint number 2. The latter has more strength, a more stable hysteretic behaviour and, as no pinching occurs, can dissipate much more energy (see also Figure 13).
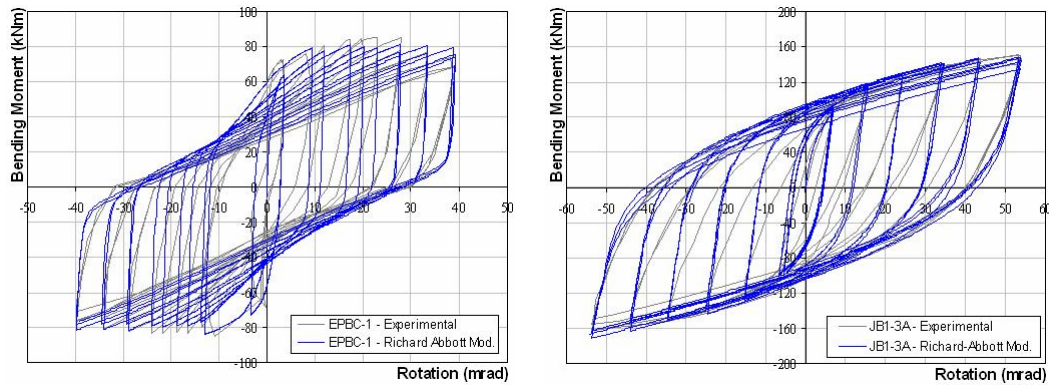
Figure 12. Hysteretic Curves for Joints 1 and 2.

To assess the accuracy of the model, the dissipated energy and the moment resistance in each cycle from the experimental tests and the Modified Richard-Abbott model were evaluated. These results are graphically presented in Figures 13 and 14. The percentage of error in each cycle was also evaluated and the results obtained are presented in all the graphs. It can be seen that, for large values of rotation, corresponding to higher values of hysteretic energy dissipation, the errors are small. Thus, in this situation, a very good agreement between the experimental and the numerical values was found.
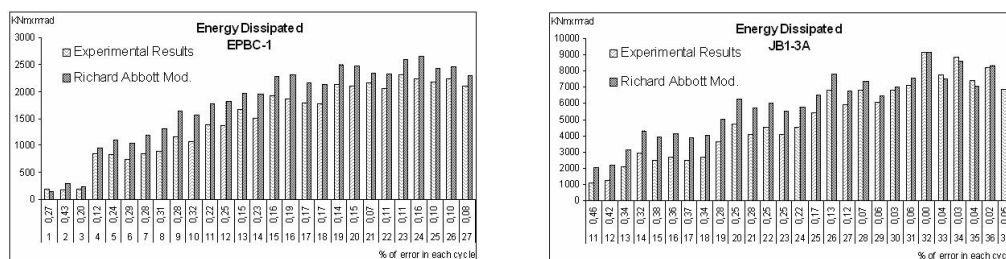
Figure 13. Energy Dissipated in Each Cycle for Joints 1 and 2.
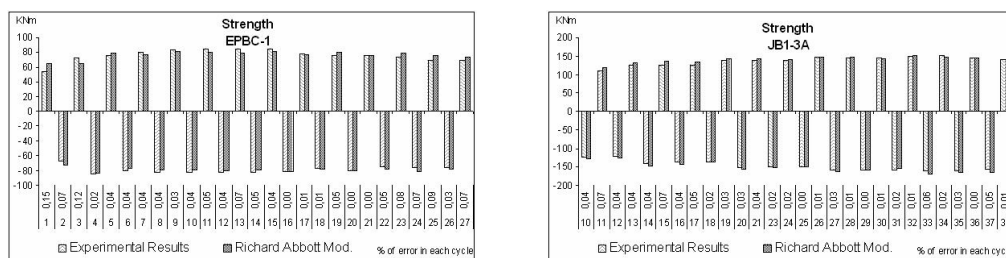
Figure 14. Moment Resistance in Each Cycle for Joints 1 and 2.

Tests number 3 and 4, with more strengthen joints than the previous tests, have no pinching, but are much more influenced by stiffness and strength deterioration, as can be seen in Figure 15. For both tests, the specimen had a good cyclic performance in terms of dissipated energy, as is shown in Figure 16. Moreover, the hysteresis loops were stable up to the onset of beam web buckling, at which beam-moment deterioration developed. The experimental and numerical curves are very close, and the model parameters are presented in Tables 9 and 10. The values of the dissipated

energy for both curves are very similar. The moment resistance values are also very similar, leading to a very small value of error, as represented in Figure 17.
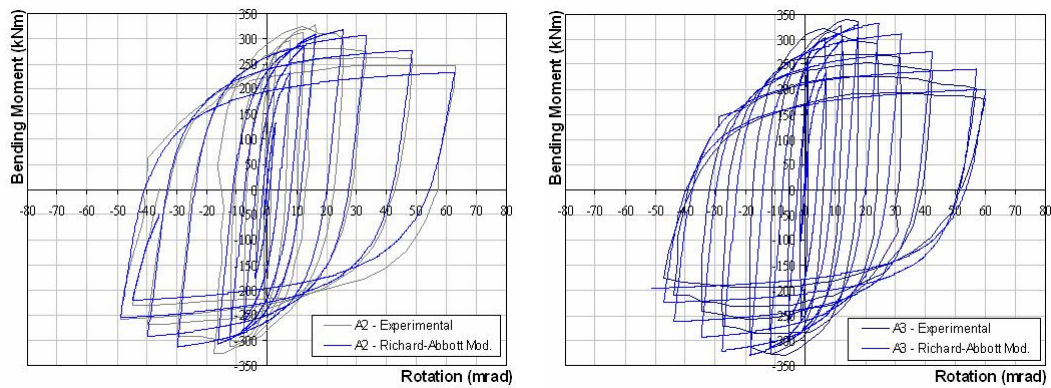
Figure 15. Hysteretic Curves for Joints 3 and 4.
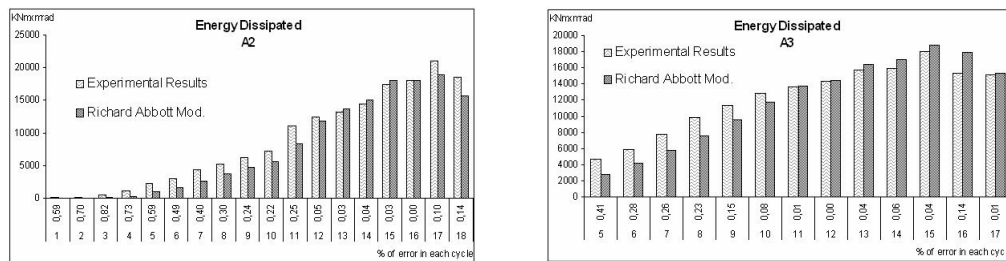
Figure 16. Energy Dissipated in Each Cycle for Joints 3 and 4.
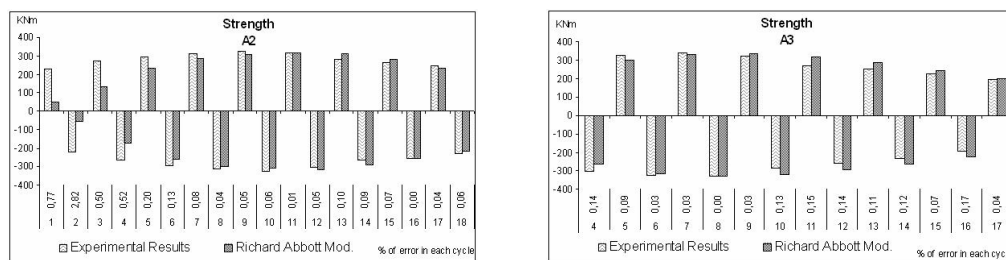
Figure 17. Moment Resistance in Each Cycle for Joints 3 and 4.

The test number 5 is a flush end plate joint directly bolted to a stiff support (no column), thus resulting in a stiffer joint, mostly governed by the endplate. The corresponding hysteretic curves can be observed in Figure 18. Because of their geometrical properties, test numbers 6 and 7 were much more influenced by pinching. Test EP4 had a mode 1 failure (according to the EC3) and the EP2 test had a mode 2 failure, governed by failure of the bolts. For both joints, no stiffness or strength degradation were observed, as can be seen in Figure 18 and from the parameters of Tables 9 and 10. Energy dissipation is also lower, as is shown in Figure 19, thus indicating inadequate seismic behaviour. The model is in good agreement with the experimental results, except for the final part of the EP2 test, because of its sudden failure.
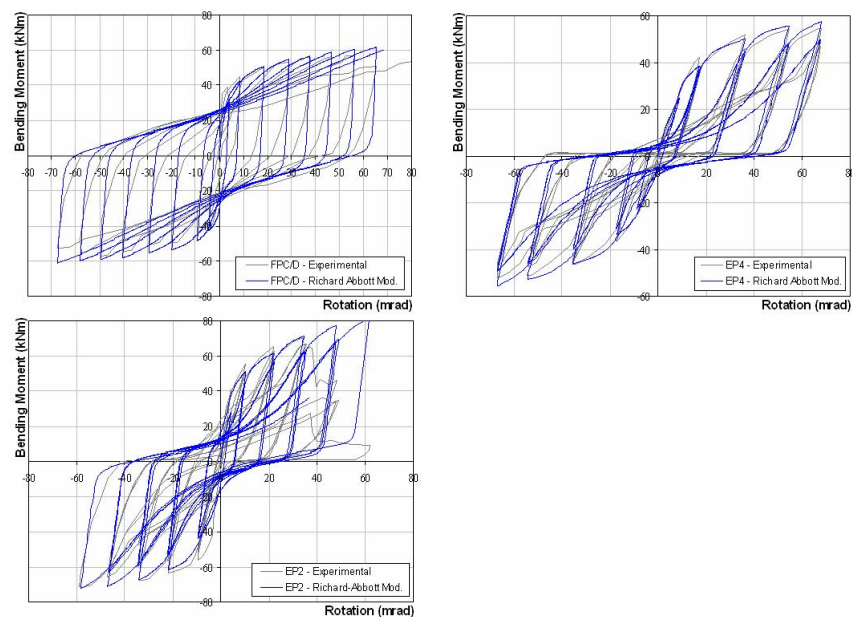
Figure 18. Hysteretic Curves for Joints 5, 6 and 7.
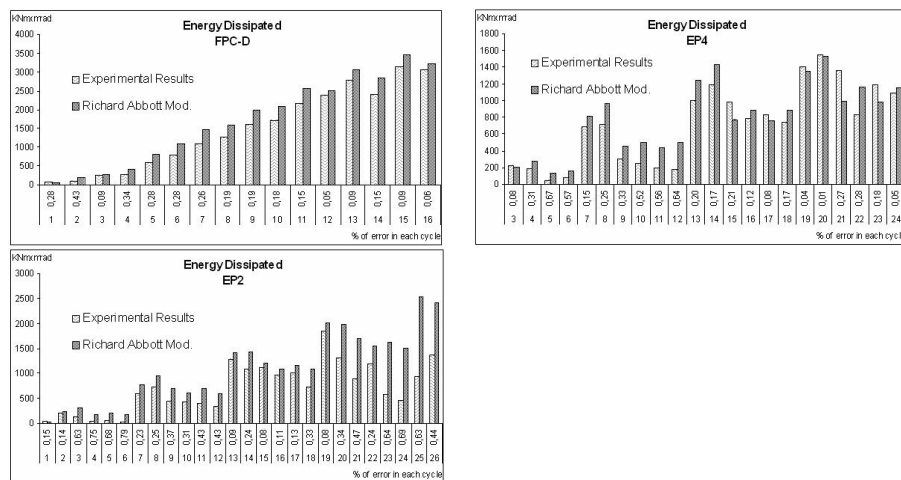
Figure 19. Energy Dissipated in Each Cycle for Joints 5, 6 and 7.
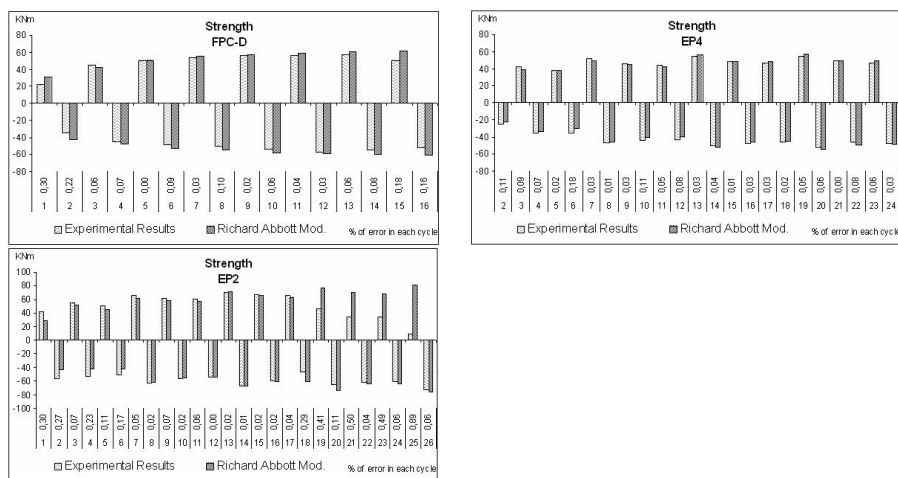
Figure 20. Moment Resistance in Each Cycle for Joints 5, 6 and 7.

The hysteretic behaviour for the top and seat cleat joints (8 to 11) is represented in Figure 21. Figures 22 and 23 depict the energy dissipation and the moment resistance, cycle by cycle. For the first test, the agreement of the experimental and numerical curves is not so good. The parameters adopted in the numerical model are also indicated in Tables 9 and 10. Joint 11 presents significant pinching, in contrast with the first three cases.
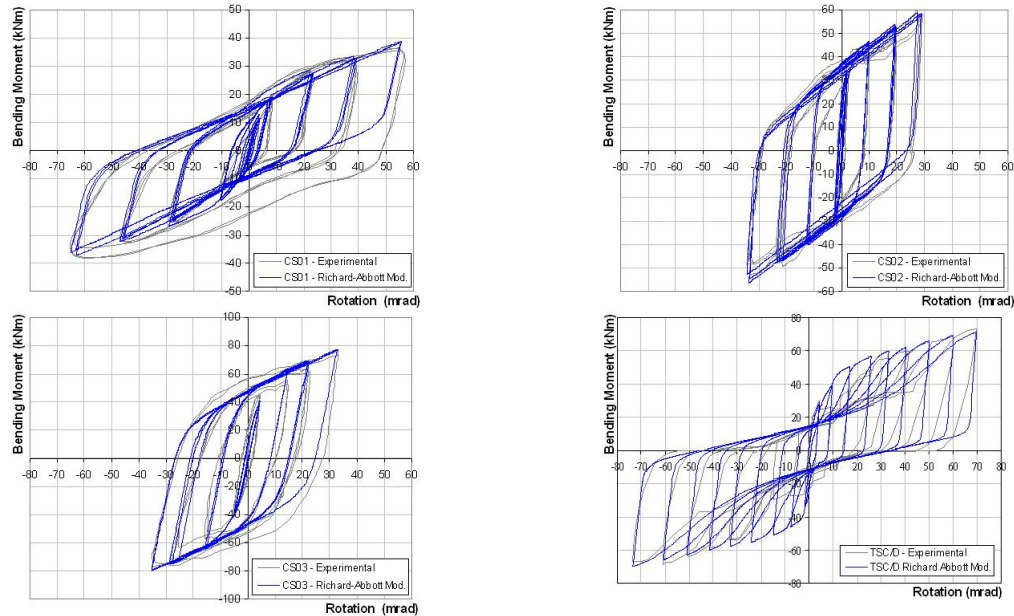
Figure 21. Hysteretic Curves for Joints 8, 9, 10 and 11.
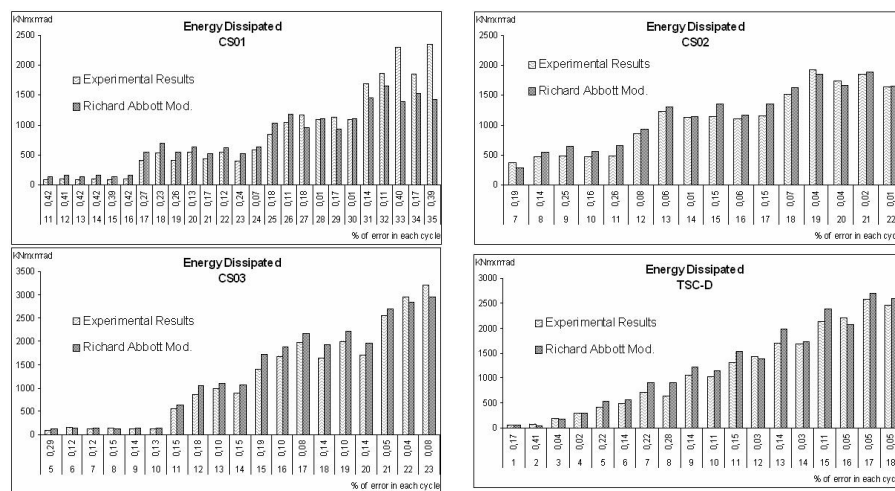
Figure 22. Energy Dissipated in Each Cycle for Joints 8, 9, 10 and 11.
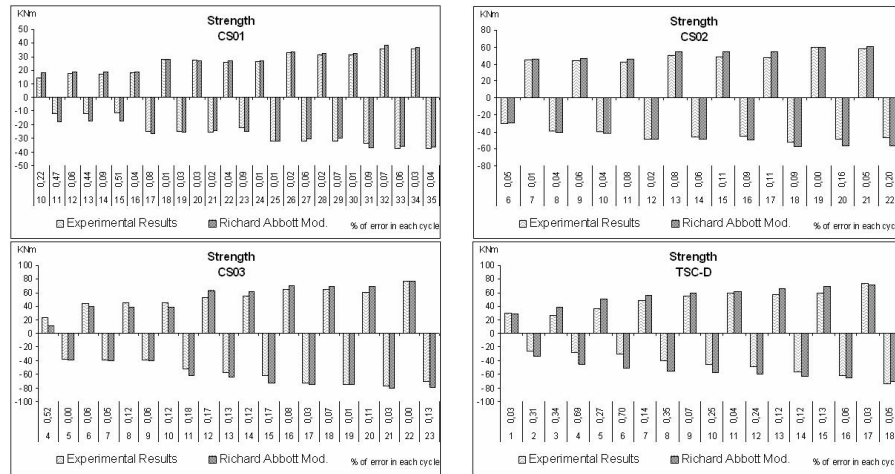
Figure 23. Moment Resistance in Each Cycle
for Joints 8, 9, 10 and 11.

Finally, for the last two tests, Figure 24 compares the experimental and the numerical curves. These tests have a better hysteretic behaviour than the flush end-plate joints, more stable and with more energy dissipation capacity. A good agreement between both curves was also obtained, as it is shown in Figures 25 and 26, for dissipated energy and strength, respectively. The parameters of the numerical model are presented in Tables 9 and 10.
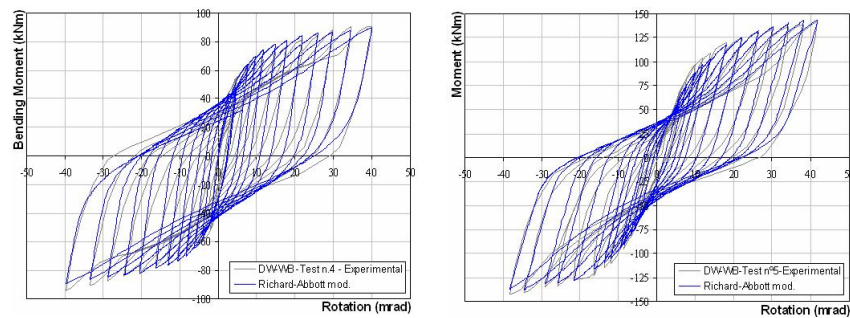
Figure 24. Hysteretic Curves for Joints 12 and 14.
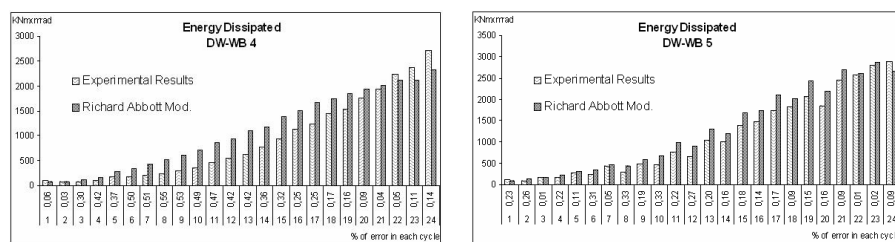
Figure 25. Energy Dissipated in Each Cycle for Joints 12 and 13.
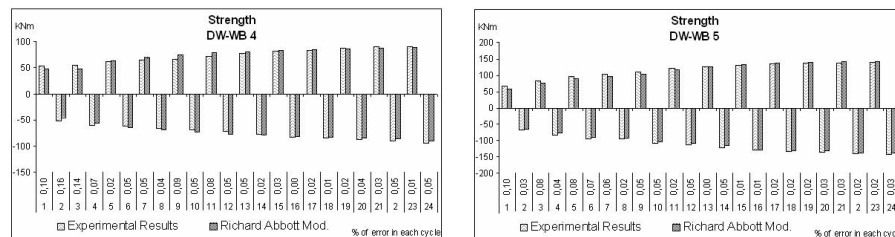
Figure 26. Moment Resistance in Each Cycle for Joints 12 and 13.

Tables 9 and 10 present the joint parameters for the ascending and descending branches, individually adjusted for each test.

Table 9. Joint Parameters for All Tests for the Ascending Branches

| Test Nº	1	2	3	4	5	6	7	8	9	10	11	12	13
K_a KNm/rad	78000	35000	63751	79370	19000	10210	4550	4300	20000	9800	12500	32263	16254
M_a KNm	80	120	400	400	50	70	60	25	38	52	55	75	142
K_{pa} KNm/rad	800	1000	1	1	300	300	100	300	900	900	300	900	1000
n_a	1	1	1	1	1	1	1	1	2	2	1	1	1
K_{ap} KNm/rad	78000	35000	0	0	19000	10210	4550	0	0	0	12500	32263	16254
M_{ap} KNm	55	80	0	0	25	15	5	0	0	0	15	50	50
K_{pap} KNm/rad	800	1000	0	0	300	200	100	0	0	0	300	900	1000
n_{ap}	1	1	0	0	1	1	1	0	0	0	1	1	1
t_{1a}	15	1	0	0	10	15	20	0	0	0	20	15	15
t_{2a}	0.3	0.3	0	0	0.3	0.3	0.3	0	0	0	0.3	0.3	0.3
C_a	1	1	0	0	1	1	1	0	0	0	1	1	1
i_{Ka}	60	10	40	40	0	0	0	0	0	0	30	30	10
i_{Ma}	0.02	0	0.03	0.05	0.03	0	0	0	0.03	0.04	0	0	0
H_a	0	0.02	0	0	0	0	0	0	0	0	0	0	0
E_{maxa} rad	0.1	0.1	0.1	0.1	0.1	0.1	0.1	0.1	0.1	0.1	0.1	0.1	0.1

Table 10. Joint Parameters for All Tests for the Ascending Branches

Test Nº	1	2	3	4	5	6	7	8	9	10	11	12	13
K_d KNm/rad	97500	35000	63751	79370	30500	10210	3550	4300	20000	9800	20100	32263	16254
M_d KNm	80	130	400	400	50	65	50	21	30	52	50	75	142
K_{pd} KNm/rad	800	1000	1	1	300	300	150	300	900	900	300	900	1000
n_d	1	1	1	1	1	1	1	1	2	2	1	1	1
K_{dp} KNm/rad	97500	35000	0	0	30500	10210	3550	4300	2000	0	20100	32263	16254
M_{dp} KNm	50	80	0	0	20	10	5	10	30	0	10	50	50
K_{pdp} KNm/rad	800	1000	0	0	300	300	100	300	900	0	300	900	1000
n_{dp}	1	1	0	0	1	1	1	1	2	0	1	1	1
t_{1d}	10	1	0	0	10	15	20	0	0	0	20	15	15
t_{2d}	0.3	0.3	0	0	0.3	0.3	0.3	0	0	0	0.3	0.3	0.3
C_d	1	1	0	0	1	1	1	0	0	0	1	1	1
i_{Kd}	60	10	30	30	0	0	0	0	0	0	0	30	10
i_{Md}	0.2	0	0.03	0.05	0.03	0	0	0	0.03	0.04	0	0	0
H_d	0	0.2	0	0	0	0	0	0	0	0	0	0	0
K_d KNm/rad	0.1	0.1	0.1	0.1	0.1	0.1	0.1	0.1	0.1	0.1	0.1	0.1	0.1

4.3   Discussion

Tables 9 and 10 highlight a significant dispersion of the various parameters for the different joint typologies. Some of these parameters are directly related to the static monotonic response of the joint: K_a and K_d (initial stiffness), M_a and M_d (moment resistance), K_{pa} and K_{pd} (post limit stiffness), n_a and n_d (shape parameter). They are obtainable from the direct application of the component method (Eurocode 3 [18]), as illustrated in Table 11 for the three selected flush end-plate joints.

Table 11. Monotonic Moment-rotation Parameters for the Flush End-plate Tests

Joint	Author	EC3 (COP®)		EC3 (Broderick)		Experimental		Failure Mode (T-stub)
		K_{ini} KNm/rad	M_{jrd} KNm	K_{ini} KNm/rad	M_{jrd} KNm	K_{ini} KNm/rad	M_{jrd} KNm	
FPC-D	Bernuzzi	19926	50.5	-	-	19000	55	Predicted – 2
EP2	Broderick	11282	49.2	11480	56.4	10210	67.7	Predicted – 2 Observed – 2
EP4	Broderick	11388	54.6	11480	49.2	3550	51.9	Predicted – 2 Observed – 1

Of greater complexity remains the establishment of the values of the remaining model parameters. Table 12 summarizes the ranges of variation for each typology.

Table 12. Variation of the Model Parameters for All Typologies

Joint Typ.	EEP		FEP	TS		WC		EEP		FEP	TS		WC
	U	S		WC	-			U	S		WC	-	
n_a	1	1	1	1-2	1-2	1	n_d	1	1	1	1-2	1	1
K_a/K_{ap}	1	?	1	?	?	1	K_d/K_{dp}	1	?	1	1-∞	1	1
M_a/M_{ap}	1.45-1.5	?	2-12	?	3.7	1.5-2.84	M_d/M_{dp}	1.6-1.625	?	2.5-10	1-∞	5	2.84
K_{pa}/K_{pap}	1	?	1-1.5	?	1	1	K_{pd}/K_{pdp}	1	?	1-1.5	1-14.3	1	1
n_a/n_{ap}	1	?	1	?	?	1	n_d/n_{dp}	1	?	1	?	1	1
t_{1a}	1-15	0	10-20	0	20	15	t_{1d}	1-10	0	10-20	0	20	15
t_{2a}	0.3	0	0.3	0	0.3	0.3	t_{2d}	0.3	0	0.3	0	0.3	0.3
C_a	1	0	1	0	1	1	C_d	1	0	1	0	1	1
i_{Ka}	10-60	40	0	0	30	10-30	i_{Kd}	10-60	30	0	0	0	10
i_{Ma}	0-0.02	0.03-0.05	0-0.03	0-0.04	0	0	i_{Md}	0-0.2	0.03-0.05	0-0.03	0-0.04	0	0
H_a	0-0.02	0	0	0	0	0	H_d	0-0.2	0	0	0	0	0

Table 13 illustrates, for each joint, the normalised values of moment resistance and initial stiffness. It is easily recognized that, apart from the two stiffened extended end-plate joints, all other joints are partial strength connections. Furthermore, the accumulated error, both in terms of total dissipated energy or average moment resistance is quite good.

Table 13. Main Properties of the Joint Behaviour

Test Number	Critical component at joint failure	Total dissipated energy error (%)		Average moment resistance error (%)	$\dfrac{[M_{j,rd}]_{joint}}{[M_{pl,rd}]_{beam}}$	$\dfrac{[K_{j,init.}]_{joint}}{\left[\dfrac{8EI_b}{d_b}\right]_{beam}}$	$\left[\dfrac{N_{sd}}{N_{pl,rd}}\right]_{column}$
1	End plate in bending	17		5	0.42	0.167	0
2	End plate in bending and web column in shear	15		4	0.76	0.075	0
3	Column flange and beam local buckling	11		31	1.54	0.110	0
4		5		21	1.57	0.137	0
5	End plate in bending	14		9	0.41	0.041	0
6	End plate in bending	11		5	0.36	0.010	0
7	End plate in bending and bolt tension	23	(*)	17	0.81	0.054	0
8	Large distortion of the top and seat angles	7		19	0.25	0.015	0.29
9		5		8	0.39	0.025	0.29
10		7		21	0.53	0.033	0.29
11	Large distortion of the top and seat angles	8		22	0.53	0.027	0
12	Yielding of the angle material	18		5	0.27	0.032	0
13		11		4	0.42	0.016	0

(*) Until cycle 17, because after that bolt failure occurred

5.   CONCLUSIONS

This paper presents the numerical implementation of a hysteretic model able to simulate the cyclic behaviour of a generic steel joint. It is incorporated in the structural analysis software SeismoStruct (Seismosoft [41]) as a joint element, thus allowing realistic non-linear static and dynamic structural analyses. The model was applied to thirteen experimental tests from six independent sources, showing a very good agreement with the experimental results, even when using different cyclic loading strategies. Despite the small sample size, a clear trend was observed for the required model parameters for end-plate and top and seat beam-to-column joints (Table 12).

The practical application of the model naturally requires confidence in the determination of the required parameters. The experimental tests used in this paper allow to identify lower and upper limits, but no reliability estimates of the parameters. Further tests are required to reach this stage, such as the experimental programme currently being carried out at the University of Coimbra to establish the cyclic behaviour and the corresponding cyclic parameters for double-symmetric extended end-plate beam-to-column joints. Nevertheless, some statements can be made:

i) For a double-symmetrical joint (recommended for seismic response), the 15 ascending parameters are the same as the 15 descending parameters.

ii) The parameters that result from static monotonic behaviour (K_a, M_a, K_{pa}, K_d, M_d, K_{pd}) can nowadays be obtained with sufficient accuracy from the application of the component method (EC3-1-8, 2005) for the range of joint typologies addressed in this paper.

iii) For joints without pinching and stiffness deterioration, such as an extended end-plate with stiffened column web in the tensile and compressive areas, only 6 parameters are needed. From these parameters, the first three can be obtained using the component method and the fourth is normally 1 or 2. The last one it is always the same, equal to 0.1 rad. The parameter related to the strength damage (i_{Ma}), can be established as an average value on the basis of a sufficient number of tests.

The influence of pinching is crucial in the establishment of the model parameters. For the end-plate joints, this is clearly noticeable and it is necessary to establish whether pinching is likely to occur. In the near future, a pragmatic way is to choose standardised steel joints, with stable hysteretic behaviour. For this case, good levels of confidence can be assumed for the choice of the model parameters. Finally, parametric studies should be carried out to assess the sensitivity of the joint response to the choice of parameters.

ACKNOWLEDGEMENTS

REFERENCES

[1]   Abolmaali, A., Kukreti, A.R. and Razavi, H., "Hysteresis Behaviour of Semi-rigid Double Web Angle Steel Connections", Journal of Constructional Steel Research, 2003, Vol. 59, pp. 1057-1082.

[2]   Adey, B.T., Grondin, G.Y. and Cheng, J.J.R., "Extended End Plate Moment Connections Under Cyclic Loading", Journal of Constructional Steel Research, 1998, Vol. 46, No. 1-3.

[3]   ATC24 procedure – Applied Technology Council (ATC), "Guidelines for Seismic Testing of Components of Steel Structures", ATC24, Redwood City, CA, 1992.

[4]   Bernuzzi, C., Zandonini, R. and Zanon, P., "Experimental Analysis and Modelling of Semi-rigid Steel Joints Under Cyclic Reversal Loading", Journal of Constructional Steel Research, 1996, Vol. 38, No. 2, pp. 95-123.

[5]   Broderick, B.M. and Thomson, A.W., "The Response of Flush Joints Under Earthquake Loading", Journal of Constructional Steel Research, 2002, Vol. 58, pp. 1161-1175.

[6]   Bursi, O.S. and Ferrario, F., "Computational Models for the Low-cycle Fatigue Behaviour of Composite Members and Joints", In Progress in Civil and Structural Engineering Computing, In Topping B.H.V. (ed.), Saxe_Coburg Publications, 2003, Stirling, Scotland, pp. 119-148.

[7]   Bursi, O.S. and Ferrario, F. and Fontanari, V., "Non-linear Analysis of the Low-cycle Fracture Behaviour of Isolated Tee Stub Connections", Computers & Structures, 2002, Vol. 80, pp. 2333-2360.

[8]   Calado, L., "Comportamento Sísmico de Ligações Viga-coluna. Caracterização Baseada na Experimentação", In IV Congresso de Construção Metálica e Mista, 2003, Cmm Press, Lisboa, pp. 645-656.

[9]   Chen, S.J., Yeh, C.H. and Chu, J.M., "Ductile Steel Beam-to-column Connections for Seismic Resistance", Journal of Structural Engineering, November 1996, Vol. 122, No. 11, pp. 1292-1299.

[10]   De Martino, A., Faella, C. and Mazzolani, F.M., "Simulation of Beam-to-column Joint Behaviour Under Cyclic Loads", Construzioni Metalliche, 1984, Vol. 6, pp. 346-356.

[11]   Della Corte, G., De Matteis, G. and Landolfo, R., "Influence of Connection Modelling on Seismic Response of Moment Resisting Steel Frames", In: Mazzolani FM (ed.). Moment Resistant Connections of Steel Buildings Frames in Seismic Areas, E. & F.N. Spon,

London, 2000.

[12]   Delphi 7, Borland Software Corporation, 2002.

[13]   Dubina, D., Ciutina, A.L. and Stratan, A., Cyclic Tests of Double-Sided Beam-to Column Joints", Journal of Structural Engineering, February 2001, Vol. 127, No. 2, pp. 129-136.

[14]   Dubina, D., Ciutina, A.L. and Stratan, A., "Cyclic Testes on Bolted Steel and Composite Double-sided beam-to-column joints", Steel and Composite Structures, 2002, Vol. 2, No. 2, pp. 147-160.

[15]   Dunai, L., Kovács, N. and Calado, L., "Analysis of Bolted End-plate Joints : Cyclic Test and Standard Approach", In Proceedings of the V International Workshop in Connections in Steel Structures, 2004, Amsterdam, pp. 191-200, June 3-4.

[16]   Elnashai, A.S. and Elgazouli, A.Y., "Seismic Behaviour of Semi-rigid Steel Frames", Journal of Constructional Steel Research, 1994, Vol. 29, pp. 149-174.

[17]   Elnashai, A.S., Elgazouli, A.Y. and Denesh-Ashtiani, F.A., "Response of Semirigid Steel Frames to Cyclic and Earthquake Loads, Journal of Structural Engineering, August 1998, Vol. 124, No. 8, pp. 857-867.

[18]   EN 1993-1-8, Eurocode 3, "Design of Steel Structures – Part 1.8: Design of Joints", Commission of the European Communities, Brussels, 2005.

[19]   Filippou, F.C., Popov, E.P. and Bertero, V.V., "Effect of Bond Deterioration on Hysteretic Behaviour of Reinforced Concrete Joints", Report Nº UCB/EERC-83/19, Earthquake Engineering Research Center, University of California, Berkeley, 1983.

[20]   Grecea, D., Stratan, A., Ciutina, A. and Dubina, D., "Rotational Capacity of MR Beam-to-column Joints Under Cyclic Loading", In Proceedings of the V International Workshop in Connections in Steel Structures, June 3-4 2004, Amsterdam, pp. 141-154.

[21]   Jaspart, J.P., "General Report : Session on Connections", Journal of Constructional Steel Research, 2000, Vol. 55, pp. 69-89.

[22]   Korol, R.M., Ghobarah, A. and Osman, A., "Extended End-plate Connections Under Cyclic Loading : Behaviour and Design", Journal of Constructional Steel Research, 1990, Vol. 16, pp. 253-280.

[23]   Kukreti ,A.R., Abolmaali, A.S., "Moment-rotation Hysteresis Behaviour of Top and Seat Angle Steel Frame Connections", Journal of Structural Engineering, ASCE, August 1999, Vol. 125, No. 8, pp. 810-820.

[24]   Leon, R.T., Hajjar, J.F. and Gustafsun, M.A., "Seismic Response of Composite Moment-resisteng Connections. I : Performance", Journal of Structural Engineering, August 1998, Vol. 124, No. 8, pp. 868-876.

[25]   Leon, R.T., Hajjar, J.F. and Gustafsun, M.A., "Seismic Response of Composite Moment-resisting Connections. II: Behaviour", Journal of Structural Engineering, August 1998, Vol. 124, No. 8, pp. 877-885.

[26]   Leon, R.T, Hu, J.W. and Schrauben, C., "Rotational Capacity and Demand in Top-seat Angle Connections Subjected to Seismic Loading", In Proceedings of the V International Workshop in Connections in Steel Structures, June 3-4 2004, Amsterdam, pp. 201-209.

[27]   Lu, L.W., Ricles, J.M., Mao, C. and Fisher, J.W., "Critical Issues in Achieving Ductile Behaviour of Welded Moment Connections", Journal of Constructional Steel Research, 2000, Vol. 55, pp. 325-341.

[28]   Mazzolani, F.M., "Mathematical Model for Semi-rigid Joints under Cyclic Loads", In R. Bjorhovde et al. (eds) Connections in Steel Structurs: Behaviour, Strength and Design, Elsevier Applied Science Publishers, London, 1988, pp. 112-120.

[29]   Mele, E., Calado, L. and De Luca, A., "Cyclic Behaviour of Beam-to-column Welded Connections", Advanced in Steel Structures - ICASS'99, Vol. I, In Shen ZY et al. (eds.), 1999, pp. 323-330.

[30]   Nogueiro, P., Simões da Silva, L. and Bento, R., "Influence of Joint Slippage on the Cyclic Response of Steel Frames", paper 66, in Topping, B.H.V. (ed.), Proceedings of 9th International Conference on Civil and Structural Engineering Computing, 2003, Civil-Comp Press, Stirling, United Kingdom.

[31]   Pradhan, A.M. and Bouwkamp, J.G., "Structural Performance Aspects on Cyclic Behaviour of the Composite Beam-column Joints", In Behaviour of Steel Structures in Seismic Areas – STESSA'94, 1994, In F.M. Mazzolani and V. Gioncu (eds.), E& FN SPON, London, pp. 221-230.

[32]   Plumier, A., "Recommended Testing Procedure for Evaluating Earthquake Resistance of Structural Elements", European Convention for Constructional Steelwork, Technical Committee 13, 1983, Brussels, Belgium.

[33]   Plumier, A. and Schleich, J.B., "Seismic Resistance of Steel and Composite Frame Structures, Journal of Constructional Steel Research, 1993, Vol. 27, pp. 159-176.

[34]   Popov, E.P., "Panel Zone Flexibility in Seismic Moment Joints", Journal of Constructional Steel Research, 1987, Vol. 8, pp. 91-118.

[35]   Popov, E.P. and Bertero, V.V., "Cyclic Loading of Steel Beams and Connections", Journal Struct. Div., ASCE, 1973, Vol. 99, No. 6, pp. 1189-1204.

[36]   Popov, E.P. and Pinkey, R.B., "Cyclic Loading of Steel Beams and Connections Subjected to Inelastic Strain Reversals, Bull N.º 3, Nov. 1968, American Iron And Steel Institute, Washington, D.C.

[37]   Popov, E.P. and Petersson, H., "Cyclic Metal Plasticity; Experiments and Theory", J. Engng Mech. Div., ASCE, December 1978, Vol. 104, Nº EM6, Proc. Paper 14257, pp. 1371-87.

[38]   Ramberg, W. and Osgood, W.R., "Description of Stress-strain Curves by Three Parameters", Monograph N.º 4, Publicazione Italsider, Nuova Italsider, Genova, 1943.

[39]   Richard, R.M. and Abbott, B.J., "Versatile Elasto-Plastic Stress-Strain Formula:, Journal of the Engineering Mechanics Division, ASCE, 1975, Vol. 101, EM4, pp. 511-515.

[40]   SAC Joint Venture, "Protocol for Fabrication, Inspection, Tenting and Documentation of Beam-column Connection Tests and Other Experimental Specimens", Rep. No. SAC/BD-97/02, Sacramento, Calif., 1997.

[41]   SeismoStruct., "Computer Program for Static and Dynamic Nonlinear Analysis of Framed Structures [online], 2004, Available from URL: http://www.seismosoft.com

[42]   Shen, J. and Astaneh-Asl, A., "Hysteretic Behaviour of Bolted-angle Connections", Journal of Constructional Steel Research, 1999, Vol. 51, pp. 201-218.

[43]   Simões, R., Simões da Silva, L. and Cruz, P., "Cyclic Behaviour of End-plate Beam-to-column Composite Joints", International Journal of Steel and Composite Structures, 2001, Vol. 1, No. 3, pp. 355-376.

[44]   Stajadinovic, B., Goel, S.C., Lee, K.H., Margarian, A.G. and Choi, J.H., "Parametric Tests on Unreinforced Steel Moment Connections", Journal of Structural Engineering, 2000, Vol. 126, No. 1, pp. 40-49, January.

[45]   Summer, E.A. and Murray, T.M., "Behaviour of Extended End-plate Moment Connections Subjected to Cyclic Loading", Journal of Structural Engineering, April 2002, Vol. 128, No. 4, pp. 501-508.

[46]   Tsai, K.C., Wu, S. and Popov, E.P., "Experimental Performance of Seismic Steel Beam-column Moment Joints", Journal of Structural Engineering, June 1995, Vol. 121, No. 6, pp. 925-931.

[47]   Yorgun, C. and Bayramoglu, G., "Cyclic Tests for Welded-plate Sections with End-plate Connections", Journal of Constructional Steel Research, 2001, Vol. 57, pp. 1309-1320.

[48]   Yu, Q.S.K. and Uang, C.M., "Effects of Near-fault Loading and Lateral Bracing on the Behaviour of RBS Moment Connections", International Journal of Steel and Composite Structures, 2001, Vol. 1, No. 1, pp. 145-158.

DESIGN OPTIMIZATION OF STEEL MOMENT FRAMES UNDER EXTREME EARTHQUAKE LOADING

Yanglin Gong

Department of Civil Engineering, Lakehead University, Thunder Bay, Ontario, Canada, P7B 5E1
Tel.: +1-807-343-8412; fax: +1-807-343-8928.
(Corresponding author: E-mail : yanglin.gong@lakeheadu.ca)

ABSTRACT: The paper presents a design optimization method for steel moment frames under extreme earthquake loading. Seismic responses of the structures are evaluated using a nonlinear pushover analysis procedure. Minimum structural cost and uniform heightwise ductility demand are identified as the design objectives. Roof and interstory drifts are taken as design constraints. Strong-column weak-beam requirement is treated as additional constraints for special moment frames. The sensitivities of inelastic displacements are employed to explicitly formulate the objective functions and constraints in terms of member sizing variables. A dual method is then used to search for an optimal design solution. The proposed design methodology is illustrated for a nine-story moment frame example.

Keywords: structural optimization; seismic design; steel moment frames; pushover analysis; ductility; design sensitivity analysis

1.   INTRODUCTION

For the seismic design of building frameworks, modern seismic provisions, such as NEHRP [1] and NBCC [2], generally employ a seismic force reduction factor to reduce elastic spectral demand to the design level to account for the ductility of structures. Structures with more ductility are designed for lower forces than less ductile structures, as ductile structures are considered capable of resisting demands that are significantly greater than their elastic strength limit. The advantage of using reduced force for design is that this force is suitable for use with an elastic structural analysis. Obviously, this design procedure is unable to evaluate the true strength of structures at the ultimate limit state. If a structure's reserve strength beyond the design level is significantly less than that implicitly assumed, the performance of the structure is unlikely to be satisfactory during severe earthquake hazards. Furthermore, inelastic displacements cannot be calculated from the results of an elastic analysis. As an approximation, seismic provisions usually use displacement amplification factors to predict the maximum inelastic displacements from the elastic displacements corresponding to the reduced seismic force. However, it was found that the values of the force reduction and displacement amplification factors adopted by modern seismic provisions, such as NEHRP [1] and NBC [2], were often far from agreement with reality [3].

Steel moment frames designed based on modern seismic provisions are deemed to deform far into inelastic region during severe earthquake hazards. They are designed using a large force reduction factor since they are regarded as being among the most ductile systems. Steel moment frames are anticipated to develop their ductility through the development of yielding in beam-column assemblies at the connections. This yielding may take the form of plastic hinge in the beams and in the columns, plastic shear deformation in panel zones, or through a combination of these mechanisms. Thus an inelastic analysis to evaluate the seismic demands on steel moment frames is essential in order to assess the true structural performance.

A major challenge in designing steel moment frames is to provide a similar ductility demand in all stories such that weak or soft story can be avoided when the structure undergoes tremendous plastification or at the incipience of collapse. Structures with inappropriate heightwise distribution

of strength and stiffness usually exhibit large deformation concentration at a soft or weak story, which might lead to collapse of the buildings. Chopra [4] studied the ductility demands for several shear buildings, which were designed conforming to the 1997 Uniform Building Code, and found that in most of cases the ductility demand in the first story was several times greater than that of all the other stories. Without using an inelastic analysis, the objective of designing building frames for a uniform ductility demand will not likely be accomplished.

Seismic design approaches based on inelastic structural analyses are greatly needed for further development of modern seismic provisions. This is reflected by the adoption of two nonlinear analysis procedures (i.e., pushover analysis and response-history dynamic analysis) by FEMA-356 [5] as major tools to evaluate seismic demands for building rehabilitations. Among these two nonlinear procedures, pushover analysis is often seen to be the more attractive method due to its relative simplicity. A pushover analysis is basically a step-by-step plastic analysis for which lateral loads of invariant relative magnitude are applied to a building structure and progressively increased until a target roof displacement or a design base shear is reached. Pushover analysis can determine the ultimate strength as well as trace the sequence of yielding events of structures with satisfactory accuracy when it is used for predicting seismic responses of low-rise to mid-rise buildings where the influence of higher modes is insignificant. Extensive research works on pushover analysis were conducted by Krawinkler and Seneviratna [6], Hasan et al. [7], Elnashai [8], among others.

Structural design is traditionally accomplished by a trial-and-error procedure, which is laborious task and cannot guarantee an optimal design. Particularly, seismic design using a pushover analysis procedure is very computationally intensive due to the inelastic nature of the analysis method. Structural optimization [9, 10], which concerns obtaining the optimal design solution for a given structure while satisfying code- and designer-specified restrictions, provides a computer-based tool that may replace conventional design approaches with a systematic design process.

The research associated with structural optimization for earthquake loading using nonlinear analysis techniques is growing recently. Ganzeri et al. [11] employed a pushover analysis to design reinforced concrete portal frames in the context of performance-based seismic design. Chan and Zou [12] proposed an optimization algorithm for reinforced concrete structures. They decomposed the design process into two single-criterion phases. The first phase was an elastic design optimization in which the cost of concrete is minimized subject to elastic displacement constraints due to a minor earthquake. The second phase was minimizing the cost of steel reinforcement subject to constraints on inelastic displacements evaluated using a pushover analysis procedure. Liu et al. [13] and Xu et al. [14] adopted a pushover analysis to predict seismic responses for a multiobjective performance-based design of steel moment frames. Though not directly concerning seismic design, other structural optimization studies involving nonlinear analysis can be found in works by Haftka [15], and Foley and Schinler [16].

In this study, a design optimization algorithm is developed for planar steel moment frames under extreme earthquake hazards. Structural design is defined herein as a process of proportioning sectional size of steel members to satisfy performance criteria under the assumption that the geometric layout of moment frames is predefined and fixed throughout the design process. The design objectives are minimum structural cost and uniform ductility demand. Drift constraints, strong-column weak-beam and member sizing requirements are imposed to the design problem. A recently developed pushover analysis technique by Hasan et al. [7] is employed to predict the seismic demands for steel moment frames. A nine-story rigid moment frame is adopted as a design example to illustrate the applicability and effectiveness of the developed design methodology.

In a companion study by the author [17] on design optimization of steel moment frames, minimum structural cost was taken as the explicit design objective while another objective of uniform ductility was achieved indirectly by manipulating interstory drift constraints. Since no ductility objective function was used explicitly, the design method did not appear to guarantee that the obtained design was always a uniform ductility design. This paper, therefore, is a further development of the previous study [17].

2. PUSHOVER ANALYSIS UNDER EARTHQUAKE LOADING

The adopted pushover analysis procedure is an elastic-plastic hinge method. The composite finite element (see Figure 1), which consists of two potential plastic-hinges at the ends of an elastic beam-column, was developed for nonlinear analysis of planar steel moment frames. The corresponding stiffness matrix $\mathbf{K}$ for the composite element is found as, [7],

$$\mathbf{K} = \mathbf{S}\,\mathbf{C}_s + \mathbf{G}\,\mathbf{C}_g \tag{1}$$

where: $\mathbf{S}$ is the standard stiffness matrix for an elastic frame member [18]; $\mathbf{C}_s$ is a correction matrix expressed in terms of plasticity-factors p that characterize the degradation of flexural stiffness due to post-elastic deformation [7]; $\mathbf{G}$ is the standard geometric stiffness matrix [18]; $\mathbf{C}_g$ is the corresponding correction matrix formulated as a function of plasticity-factors p [7]. The plasticity-factor p of the plastic hinge at each member end is defined as,

$$p = \frac{1}{1 + 3EI/R^p L} \tag{2}$$

where R^p is the instantaneous rotational stiffness of the potential plastic hinge there, and L and EI are the length and elastic flexural stiffness of the member, respectively. For a fully elastic section $R^p = \infty$ and $p = 1$, for a fully plastic section $R^p = 0$ and $p = 0$, while for a partially plastic section $0 < p < 1$.
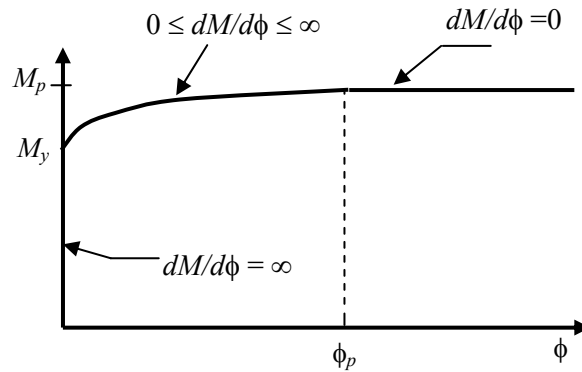
Figure 1. Composite Planar Beam-column Element

2.1 Single Stress Yield Condition

The moment-rotation (M-ϕ) relation that characterises the nonlinear variation in the post-elastic rotational stiffness R^p of a plastic-hinge section under increasing moment (see Figure 2) is taken to be, [7],

$$M(\phi) = M_y + \sqrt{\left(M_p - M_y\right)^2 - \left[\left(M_p - M_y\right)\left(\phi_p - \phi\right)/\phi_p\right]^2} \tag{3}$$
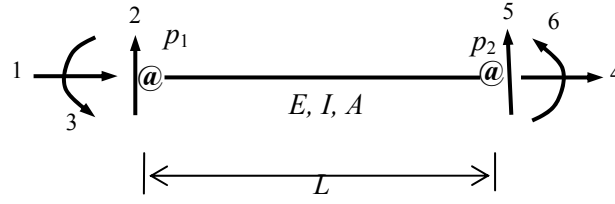
Symbol **@** represents a plastic hinge

Figure 2. Post-elastic Moment-rotation Relation for Plastic Hinges

where $M_y = S\sigma_{ye}$ and $M_p = Z\sigma_{ye}$ are the known first-yield and fully-plastic moment capacities of the member section, respectively (S and Z are the elastic and plastic section moduli, respectively, and σ_{ye} is the expected yield stress of steel material.), and ϕ is the extent of post-elastic rotation occurring somewhere between first yielding ($\phi=0$) and full plastification ($\phi=\phi_p$) of the cross-section. From Eq. (3), the post-elastic moment varies in the range $M_y \leq M(\phi) \leq M_p$ as the plastic rotation varies in the range $0 \leq \phi \leq \phi_p$, as shown in Figure 2. Upon differentiating Eq. (3) with respect to ϕ, the post-elastic rotational stiffness of the section is found as,

$$R^p = \frac{dM(\phi)}{d\phi} = \frac{(M_p - M_y)^2 (\phi_p - \phi)}{\phi_P^2 \sqrt{(M_p - M_y)^2 - \left[(M_p - M_y)(\phi_p - \phi)/\phi_p\right]^2}} \quad (0 < \phi \leq \phi_p) \tag{4}$$

The incremental load-step method [18] is adopted to conduct the pushover analysis. The first step load is taken arbitrarily small so that the structure remains elastic. The structural global stiffness matrix is initially formed from member stiffness matrices defined by Eq. (1) by setting all plasticity-factors equal to unity ($p=1$) in matrices $\mathbf{C}_s$ and $\mathbf{C}_g$. After each incremental load, the structural tangent stiffness matrix is updated for member stiffness matrices modified by plasticity-factors p found from Eq. (2).

2.2   Combined Stress Yield Condition

The Section 2.1 is extended to the combined bending moment M and axial force N for members of planar frameworks. The reduction in the moment capacity of a member cross-section due to the presence of axial force can be account for through the following interaction equation, [19],

$$\frac{1}{f_s} \leq \frac{M}{M_p} + \left[\frac{N}{N_p}\right]^a \leq 1 \tag{5}$$

where A is the cross-section area and $N_p = A\sigma_{ye}$ is the fully-plastic axial force capacity; $f_s = M_p/M_y = Z/S$ is the section shape factor. The exponent a depends on the section shape (e.g., $a = 2$ for a rectangular section).

For this study, $a=1$ was used for the sake of illustration. Note that a linear interaction curve is conservative and applicable for both tensile and compressive axial forces [20]. The two bounds of Eq. (5) define the plasticity zone are shown in Figure 3. Here, assuming that the ratio M/N remains invariant in the post-elastic response range for the combined stress case when both $M \neq 0$ and $N \neq 0$, identical satisfaction of the lower bound of Eq. (5) at generic point O_y in Figure 3 corresponds to first-yield behavior occurring at the reduced yield moment level $M_y^r = M_p/\xi f_s$ (where

$\xi = M_y/M_y^r = M_p/M_p^r$ and $\xi > 1$), while identical satisfaction of the upper bound of Eq. (5) at related point O_p in Figure 3 corresponds to fully-plastic behavior occurring at the reduced plastic moment level $M_p^r = M_p/\xi = f_s M_y^r$. Upon replacing M_y and M_p with the reduced moments M_y^r and M_p^r, Eqs. (3) and (4) then respectively define post-elastic moment-rotation and flexural-stiffness relations that account for the influence of axial force on bending moment capacity of member sections, and the post-elastic analysis can proceed exactly as for the single stress yield condition in Section 2.1.
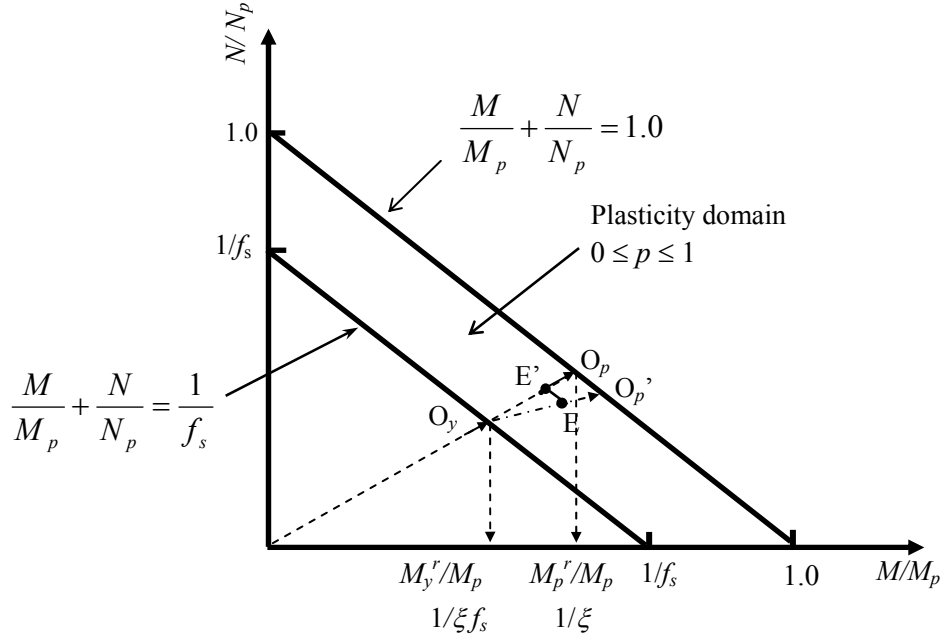
Figure 3. Combined Action of Bending Moment and Axial Force

The assumption that the ratio M/N remains constant in the post-elastic response range in Figure 3 is not always the case in reality. For example, sectional forces may follow the line O_y--O_p' in Figure 3, which results in a negative argument for the square root term in Eq. (5). To overcome such a computational difficulty, an equivalent moment concept is introduced by projecting the real bending moment to line O_y--O_p (e.g., bending moment at point E in Figure 3 is projected to point E' by drawing a line parallel to the yielding boundary through the moment point). Then, M in Eq. (5) is replaced by an equivalent moment M_{eq} found from the similarity of triangles shown in Figure 3; i.e., assuming $a=1$ for Eq. (5):

$$\frac{M_y^r}{M_{eq}} = \frac{1/f_s}{\zeta} \qquad \therefore \quad M_{eq} = M_y^r \zeta f_s \tag{6}$$

where $\zeta = (N/N_p + M/M_p)$. In the above transformation, M_{eq} has the same sense as the original bending moment.

The pushover analysis is performed for constant gravity loads and monotonically increasing lateral inertial loads. Seismic demands are equal to the structural responses at the load step when the base shear force is equal to the design base shear, which is determined according to an inelastic design spectrum. The design base shear can be evaluated as:

$$V_b = \frac{S_a}{g} W \tag{7}$$

where: S_a (in the unit of g) is the spectral response acceleration corresponding to a specified extreme earthquake hazard, e.g., a 2% probability of exceedance in 50-year earthquake event; g is the gravitational acceleration; and W is the seismic weight of the framework. Without loss of generality, the spectral response acceleration S_a curve for this study is taken as, [4],

$$S_a = \begin{cases} S_s & T \leq T_0 \\ \dfrac{S_1}{T} & T > T_0 \end{cases} \tag{8}$$

where: T is the elastic fundamental period of the structure in seconds; T_0 is the period at which the constant acceleration and constant velocity regions of the response spectrum intersect for the design earthquake; and S_s and S_1 are corresponding short-period and one-second-period response acceleration parameters, respectively. The design spectrum has already accounted for target ductility.

The design base shear V_b is applied to the structure according the load pattern defined by, [5],

$$\mathbf{P}_l = V_b \begin{Bmatrix} C_{v,1} \\ C_{v,2} \\ ... \\ C_{v,n_s} \end{Bmatrix} = V_b \cdot \mathbf{C}_v \tag{9}$$

where: $\mathbf{P}_l$ is the vector of lateral inertial loads applied at the n_s stories of the structure; $\mathbf{C}_v$ is the vector of lateral inertia load distribution factors $C_{v,s}$ ($s = 1, \ldots, n_s$), which is determined from, [5],

$$C_{v,s} = \frac{P_s}{V_b} = \frac{G_s H_s^\lambda}{\displaystyle\sum_{t=1}^{n_s} G_t H_t^\lambda} \tag{10}$$

where: P_s is the lateral inertial load applied at story level s; G_s and G_t are the portions of the building seismic weight at story levels s and t, respectively; H_s and H_t are the vertical distances (or heights) from the base of the building to story levels s and t, respectively; n_s is the number of stories; and λ is an exponent whose value depends on the fundamental period of the structure.

The elastic fundamental period of the structure T is found as, [4],

$$T = 2\pi \left[\frac{\displaystyle\sum_{s=1}^{n_s} \left(m_s v_s^2 \right)}{\displaystyle\sum_{s=1}^{n_s} \left(V_1 C_{v,s} v_s \right)} \right]^{1/2} \tag{11}$$

where: m_s is the seismic mass of story s; V_1 is a base shear force taken to be sufficiently small to ensure that the resulting lateral displacement v_s of story level s corresponds to elastic behaviour of the structure.

The overall vector $\mathbf{P}$ of nodal loads accounting for both lateral inertial and gravity loading is given by,

$$\mathbf{P} = \mathbf{D}\,\mathbf{P}_l + \mathbf{P}_g \tag{12}$$

where $\mathbf{D}$ is a Boolean matrix, and $\mathbf{P}_g$ is the vector of nodal gravity loads for the structure (see examples of $\mathbf{P}$, $\mathbf{D}$, $\mathbf{P}_l$, and $\mathbf{P}_g$ in Appendix).

The pushover analysis use centerline dimensions to model all frame members. Rigid beam-to-column connections are assumed. Panel zone deformation is neglected. More detailed descriptions on the pushover analysis were given by Hasan et al. [7] and Gong [21].

3. OPTIMAL DESIGN PROBLEM FORMULATION

3.1 Objective Criteria

Two design objectives concerning structural cost and uniform ductility demand are identified for this study.

Minimum structural cost is perhaps the most favorable design objective and is commonly adopted by many optimization problems. Some attempts (e.g.,Wen and Kang [22]) have been made to develop a general building cost function. Unfortunately, a complete description of the real cost of a building before its construction is often nearly impossible because many factors that affect the cost are unpredictable and not precisely defined. As the mathematical formulation of a meaningful cost function in a truly broad context is virtually impossible to achieve for a structural framing system considered in isolation, as herein, the cost of the members of the structure is alone taken to define the cost objective function for this study, while structural fabrication and erection costs are implicitly considered in the design process through a member grouping technique, illustrated by the design example in Section 6. Assuming that the cost of a member is proportional to its material weight, the least-cost design can be interpreted as the least-weight design of the structure, and the cost objective function f_1 (also called the weight objective) to be minimized is formulated as:

$$f_1(\mathbf{x}) = \frac{1}{W_{max}} \sum_{j=1}^{n_e} \rho L_j A_j \tag{13}$$

where: $\mathbf{x}$ is the generic representation of the vector of design variables; ρ is the material mass density; n_e is the number of members; L_j and A_j are the length and cross-section area of the jth member, respectively. The function f_1 is normalized by the maximum possible weight of the frame W_{max}, which is calculated as $W_{max} = \sum \rho L_j A_j^U$, where A_j^U is the upper-bound cross section area for member j ($j=1,2,...n$) and taken from AISC Manual [23] for this study. The normalization facilitates the numerical realization of the design formulation since the value of f_1 always varies in the range $0 \le f_1 \le 1$ whatever size the structure is and whatever unit is used for computing the structural weight. Furthermore, the magnitude of f_1 value is at the same order as that of objective function f_2, which is introduced in the following.

It has been observed in many collapsed structures that deformation concentration took place at a soft (or weak) story under severe earthquake loading, which directly led to building failure. To avoid the weak or soft story failure, it is necessary to design the structure such that the ductility demands in all the stories are similar. In other words, a uniform heightwise ductility demand is a desirable objective for seismic design [4]. To this end, since a building exhibiting a uniform plastic interstory drift distribution experiences minimum plastic deformation concentration, the uniform ductility design objective can be interpreted as pursuing a uniform heightwise plastic interstory

drift distribution. Therefore, this design objective can be formulated as to minimize the following function f_2 as, [14]:

$$f_2(\mathbf{x}) = \left[\frac{1}{n_s}\sum_{s=1}^{n_s-1}\left(\frac{v_s(\mathbf{x})/H_s}{\Delta(\mathbf{x})/H}-1\right)^2\right]^{1/2} \tag{14}$$

where H_s and H are the distances from the building ground level to story s and the roof, respectively, while $v_s(\mathbf{x})$ and $\Delta(\mathbf{x})$ are the lateral plastic deflections of story s and the building roof under the considered earthquake hazard, respectively. In effect, f_2 defines the coefficient of variation of the story drift distribution, since v_s/H_s and Δ/H represent the plastic story drift ratio and the building mean drift ratio, respectively. By definition, the value of $f_2(\mathbf{x})$ is not less than zero, and only for the extreme case of a perfectly uniform interstory drift distribution is $f_2(\mathbf{x})=0$.

3.2   Design Variables

The cross section sizes of the members are taken to be design variables for this study. Four cross-sectional properties, i.e., the area A, moment of inertia I, elastic modulus S (associated with first yield) and plastic modulus Z (associated with full plasticity) are required in pushover analysis. For a specified type and nominal depth of commercially available standard steel sections, these four properties can be related together through functional relationships which are expressed as:

$$I = C_1 A^2 + C_2 A + C_3 \tag{15}$$

$$S = C_4 A + C_5 \tag{16}$$

$$Z = f_s S \tag{17}$$

$$Z = C_6 (1/A)^{C7} \tag{18}$$

where C_1 to C_7 are constants determined by regression analysis [21]. For examples, the values of C_1 to C_7 for some commercial W sections of specified nominal depths [23] are listed in Table 1. Having such relationships, the cross section area A can be taken as the only design sizing variable, thereby reducing the number of design variables significantly. Equations (15) to (17) play an important role in the design automation since pushover analysis results are very sensitive to the sectional properties I, S and Z, which therefore need to be estimated as accurately as possible during the design process. Equation (18) is used to formulate strong-column weak-beam constraints in terms of reciprocal variables (see Subsection 3.4).

Table 1. Section Properties Relationships

Section	$I = C_1 A^2 + C_2 A + C_3$			$S = C_4 A + C_5$		$Z = C_6 (1/A)^{C7}$	
Type	C_1	C_2	C_3	C_4	C_5	C_6	C_7
W14	0.14	22922	−25781536	5.95	−25.64	82.39	−1.05
W30	0.12	115380	−536216897	11.42	−55.77	77.76	−1.12

Note: unit of millimeter is used for all properties.

3.3   Design Constraints

According to the roles they play in determining design variables, design constraints can be classified as being primary or secondary. Those that play major roles in the design selection are referred to as primary constraints, while those that are not expected to significantly participate in the design selection are labeled as secondary constraints. For this study, the following three types of constraints are considered:

(1) Drift constraints, which are primary design constraints for steel moment frames in high seismic zones [24].
(2) Strong column/weak-beam constraints, which are mandatory requirement for special moment frames [25].
(3) Side constraints. The lower and upper limits imposed on the values of the design variables.

The member strength requirements are secondary for the seismic design in high seismic zones. Foutch and Yun [24] concluded that the drift limitation always governs in high seismic zones for new steel moment frame buildings. For the sake of simplicity, the member strength requirements are not included in the design formulation in this study. However, they can be easily incorporated into the side constraints if necessary (Chan et al. [26]).

3.3.1   Drift constraints

Moderate drift or lateral deflection of a building may cause human discomfort, and minor damage of nonstructural components, such as cracking of partitions or cladding and the leakage of pipes. Large inelastic drift due to an extreme earthquake can cause the failure of mechanical, electrical and plumbing systems, or cause suspended ceilings and equipment to fall, thereby posing threats to human life. Thus, it is essential to control the drift of building frameworks under seismic loading.

There are two kinds of lateral drifts to be considered in design practice. One is the overall building drift (roof drift). The other is the interstory drift, defined as the drift difference between two adjacent floors. The overall building drift represents the average lateral translation. For this study, a roof drift constraint is imposed in the design formulation, i.e.,

$$\Delta(\mathbf{x}) \leq \overline{\Delta} \tag{19}$$

where $\overline{\Delta}$ is allowable roof drift, which is taken as the target displacement under the considered earthquake hazard. A target displacement is the maximum roof lateral deflection likely to be experienced by the structure during the design earthquake.

Interstory drift can be related to the plastic rotation demand imposed on individual beam-column connection assemblies, and is therefore an excellent predictor of the performance of beams, columns and connections [27]. Design standards normally requires limitation on interstory drift, which are expressed as,

$$\delta_s(\mathbf{x}) \leq \overline{\delta} \quad (s = 1, \cdots n_s) \tag{20}$$

where: δ_s is the interstory drift of story s (i.e., $\delta_s = v_s - v_{s-1}$, the difference between the drift v_s at story s and the drift v_{s-1} at story s-1); $\overline{\delta}$ is the allowable interstory drift. δ/h is called interstory drift ratio, where h is the height of the corresponding story. The allowable interstory drift $\overline{\delta}$ is determined accounting for the desired structural performance and interstory drift capacity [27].

3.3.2 *Strong-column weak-beam constraints*

In earthquake engineering, one of the design goals is to provide the structure with good energy dissipation capacity. In this regard, the 'Strong-Column Weak-Beam' (SC/WB) concept is introduced in seismic provisions as a means to help meet this objective for moment frames. The SC/WB concept is implemented through the following constraint applied at beam-to-column connections, [25]:

$$r_{cb} = \frac{\sum M_{pc}^*}{\sum M_{pb}^*} > 1.0 \qquad (21)$$

where: r_{cb} is the so-called column-beam moment ratio; $\sum M_{pc}^*$ is the sum of the moment capacities in the column above and below the joint, calculated as $\sum M_{pc}^* = \sum[(Z)(\sigma_y - N/A)]$ (where N is the axial compressive force for the column and σ_y is the design yield strength.); $\sum M_{pb}^*$ is the sum of moment capacities in the beams at the joint, calculated as $\sum M_{pb}^* = \sum[1.1(Z)(\sigma_{ye}) + M_v]$ (where the factor of 1.1 is introduced to recognize the potential over-strength of beams due to other considerations; M_v is the additional moment due to shear amplification from the location of the plastic hinge to the column centerline. M_v is zero for this study since centerline dimensions are used in the structural model and plastic hinges are assumed to occur at the ends of members); and subscripts b and c refer to beams and columns at the connection under consideration.

The SC/WB provision is mandatory only for special moment frames in AISC Seismic Provisions [25]. It is noted that axial compressive force in columns is taken into account in calculating $\sum M_{pc}^*$ while axial tensile force is ignored when using Eq. (21). No reason is given in its companion commentary for this discrimination between tensile and compressive forces [25].

3.4 Design Formulation

Generally speaking, it is desirable to use commercially available standard sections to proportion steel frameworks. To this end, the design process is carried out in two phases. Phase I treats the design as a continuous variable design problem. Phase II utilizes a dynamic rounding-off strategy to find the discrete commercial section for each design variable based on the phase I results. Each phase further includes two stages. The objective of Stage One is to search for a least-weight design, while the objective of Stage Two is to search for a uniform ductility design. A detailed step-by-step description of design procedure is given in Section 5.

From the foregoing, the optimization model is formulated as:

$$\text{Minimize} \quad f_1(\mathbf{x}) = \frac{1}{W_{\max}} \sum_{j=1}^{n_e} \rho L_j A_j \quad \text{at Stage One} \qquad (22)$$

or

$$\text{Minimize} \quad f_2(\mathbf{x}) = \left[\frac{1}{n_s} \sum_{s=1}^{n_s - 1} \left(\frac{v(\mathbf{x})/H_s}{\Delta(\mathbf{x})/H} - 1 \right)^2 \right]^{1/2} \quad \text{at Stage Two} \qquad (23)$$

$$\text{Subject to:} \quad \Delta(\mathbf{x}) \le \overline{\Delta} \qquad (24)$$

$$\delta_s(\mathbf{x}) \leq \bar{\delta} \quad (s = 1, \cdots n_s) \tag{25}$$

$$A_j^L \leq A_j \leq A_j^U \quad (j = 1, 2, \cdots, n_e) \tag{26}$$

and SC/WB constraints for special moment frames:

$$-\sum_c \left[Z \cdot \left(\sigma_y - \frac{N}{A} \right) \right]_c + \sum_b (1.1 \cdot Z \cdot \sigma_{ye})_b \leq 0 \tag{27}$$

Design constraints, Eqs. (24) to (27), are the same for both Stages One and Two. Equations (26) are side constraints, where sizing limitations are taken as the lower and upper bounds A^L and A^U on the cross-sectional areas A of commercially available sections (see design example in Section 6). Equation (27) for the constraints, which are imposed to the specified joints, is derived from Eq. (21), where subscripts c and b refer to column and beam at the specified joint, respectively.

The idea of the two-stage design strategy is inspired by the finding that a uniform ductility design can be obtained with a structural weight being only slightly greater than that of a pure minimum-weight design in a pilot study conducted by the author [21]. In Stage One, a minimum-weight design is obtained subject to drift and side constraints (and SC/WB constraints for special moment frames). In Stage Two, an optimal design with an improved ductility distribution over the minimum-weight design is obtained. This two-stage strategy eliminates the necessity of combining the two design objectives into one (a practice often involves arduous numerical efforts in determining the combination factors for the multi-objective optimization [14, 21]).

The dynamic rounding-off strategy (also called pseudo-discrete section selection strategy by Chan *et al.* [26]) employed in Phase II to find discrete sections is a modification of the simple rounding-up method that rounds up all section sizes found from the continuous optimization solution to their nearest available discrete section sizes. While the simple rounding-up method is direct and easy to implement, it sometimes results in a significant stiffness redistribution for the structure that can make the design solution infeasible [28]. Also, it overlooks the fact that it is often unnecessary to increase all the variables to their nearest upper discrete values as some of them could be just as well decreased to their nearest lower discrete values. Instead of assigning all design variables to their nearest upper discrete values at one time, the dynamic rounding-off method rounds up only one or a few variables at a time. Then, the selected variable(s) are fixed at their assigned discrete value and the design is optimized again for the reduced set of remaining variables. This process is repeated until all variables have been selected and assigned discrete values.

To enable computer solution of the design optimization problem, it is necessary to use an approximation technique to formulate Eqs. (23) to (25) explicitly in terms of design variables. High quality approximations can be obtained by adopting the reciprocal variables, [29],

$$x_j = \frac{1}{A_j} \tag{28}$$

and then employing first-order Taylor series to reformulate Eqs. (22) to (27) as the explicit design problem,

Minimize $\quad f_1(\mathbf{x}) = \dfrac{1}{W_{max}} \displaystyle\sum_{j=1}^{n_e} \dfrac{\rho L_j}{x_j} \quad$ at Stage One $\tag{29}$

or

Minimize $f_2(\mathbf{x}) = \left[f_2(\mathbf{x})\right]^0 + \sum_{j=1}^{n_e} \left[\dfrac{df_2(\mathbf{x})}{dx_j}\right]^0 \left(x_j - x_j^0\right)$ at Stage Two   (30)

Subject to: $\left[\Delta(\mathbf{x})\right]^0 + \sum_{j=1}^{n_e} \left[\dfrac{d\Delta(\mathbf{x})}{dx_j}\right]^0 \left(x_j - x_j^0\right) \leq \overline{\Delta}$ (31)

$\left[\delta_s(\mathbf{x})\right]^0 + \sum_{j=1}^{n_e} \left[\dfrac{d\delta_s(\mathbf{x})}{dx_j}\right]^0 \left(x_j - x_j^0\right) \leq \overline{\delta}$ $(s = 1, \cdots n_s)$ (32)

$x_j^L \leq x_j \leq x_j^U$ $(j = 1, 2, \cdots, n_e)$ (33)

and SC/WB constraints for special moment frames:

$\sum_{c} c_c x_c + \sum_{b} c_b x_b - g_{cb}^U \leq 0$ (34)

where: superscript ' ^{0} ' represents values for the current design; x_j^L and x_j^U are lower and upper bounds on the reciprocal area x_j, respectively, where $x_j^L = 1/A_j^U$ and $x_j^U = 1/A_j^L$; df_2/dx_j, $d\Delta/dx_j$, and $d\delta/dx_j$ are the sensitivities of objective function f_2, roof drift Δ and interstory drift δ with respect to the design variable x_j, respectively. The formulations of these sensitivities are presented in Section 4.

The SC/WB equation of constraints, Eq. (34), is derived as described in the following. Firstly, Z is approximated by a first-order Taylor series formulated at the current design point x^0 by applying Eq. (18), i.e.,

$Z = Z^0 + \left(\dfrac{dZ}{dx}\right)^0 \left(x - x^0\right)$ (35)

where

$\dfrac{dZ}{dx} = C_6 C_7 \left(\dfrac{1}{A}\right)^{C_7 - 1} = C_6 C_7 x^{C_7 - 1}$ (36)

Equation (34) is obtained by substituting Eq. (35) into Eq. (27) and then by defining the following coefficients:

$c_c = -\left(\dfrac{dZ}{dx}\right)_c^0 \left(\sigma_y - \dfrac{N}{A}\right)_c$ (37)

$c_b = 1.1 \left(\dfrac{dZ}{dx}\right)_b^0 \left(\sigma_{ye}\right)_b$ (38)

$$g_{cb}^U = \sum_c \left[Z^0 - \left(\frac{dZ}{dx}\right)^0 x^0 \right]_c \left(\sigma_y - \frac{N}{A} \right)_c - \sum_b 1.1 \left[Z^0 - \left(\frac{dZ}{dx}\right)^0 x^0 \right]_b \left(\sigma_{ye} \right)_b \qquad (39)$$

The optimization model Eqs. (29) to (34) is solved iteratively by using numerical optimization techniques. Each iteration begins with a pushover analysis of the current design to compute the values of objective function (i.e., f_2^0 in Eq. (30)) and constraints (i.e., Δ^0 and δ_s^0 in Eqs. (31) and (32)) along with sensitivities (i.e., $(df_2/dx_j)^0$, $(d\Delta/dx_j)^0$ and $(d\delta_s/dx_j)^0$ in Eqs. (30) to (32)). Then a minimization algorithm called Dual method [30] is employed to solve Eqs. (29) to (34) for an improved design, which is further taken as the current design for the next iteration.

4.   SENSITIVITY ANALYSIS

Gong et al. [31, 32] derived sensitivity analysis formulations for the pushover analysis procedure described in Section 2. For the completeness of this paper, the sensitivity formulations are given briefly in the following.

The equilibrium equations for a pushover analysis can be stated as,

$$\mathbf{F}(\mathbf{u}, \mathbf{A}) = \mathbf{P}(\mathbf{A}) \qquad (40)$$

where: $\mathbf{F}(\mathbf{u}, \mathbf{A})$ is the overall internal nodal force vector; $\mathbf{P}(\mathbf{A})$ is the overall externally applied nodal load vector in Eq. (12); $\mathbf{u}$ is the vector of nodal displacements; $\mathbf{A}$ is the vector of design variables which are taken as the cross sectional areas of the members.

Differentiating Eq. (40) with respect to design variable A_j gives

$$\mathbf{K}^t \frac{d\mathbf{u}}{dA_j} = \frac{d\mathbf{P}}{dA_j} - \frac{\partial \mathbf{F}}{\partial A_j} \qquad (41)$$

where $\mathbf{K}^t = \partial\mathbf{F}/\partial\mathbf{u}$ is the global tangential stiffness matrix. $d\mathbf{P}/dA_j$ is the sensitivity of the nodal load vector with respect to design variable A_j. For this study, $d\mathbf{P}/dA_j$ reflects the influence of structural modifications on earthquake loading.

Consider a particular displacement μ_l for a given framework, which is related to the overall vector of nodal displacements $\mathbf{u}$ as,

$$\mu_l = \mathbf{b}_l^T \mathbf{u} \qquad (42)$$

where $\mathbf{b}_l$ is a Boolean vector (consisting of 0 and 1) that depends on the nature of displacement μ_l. For instance, if $\mu_l = v_1$ is the lateral drift of a story, the vector $\mathbf{b}_l$ is obtained by setting the component entries corresponding to degrees of freedom v_1 to unity while setting the rest of the entries to zero; namely, $\mathbf{b}_l^T = \{1, 0, 0, \dots, 0\}$ assuming that v_1 corresponds to degree of freedom 1.

The sensitivity of displacement μ_l with respect to changes in design variable A_j is then found as, from Eqs. (42) and (41),

$$\frac{d\mu_l}{dA_j} = \mathbf{b}_l^T \frac{d\mathbf{u}}{dA_j} = \mathbf{U}_l^T \left[\frac{d\mathbf{P}}{dA_j} - \frac{\partial \mathbf{F}}{\partial A_j} \right] \tag{43}$$

where $\mathbf{U}_l^T = \mathbf{b}_l^T \mathbf{K}^{t-1}$ or $\mathbf{U}_l = \mathbf{K}^{t-1} \mathbf{b}_l$.

The major effort in nonlinear sensitivity analysis is the evaluation of the partial derivatives of internal nodal forces, i.e., the term $\partial \mathbf{F}/\partial A_j$ in Eq. (43). Since the pushover analysis uses the incremental-load method, the vector of internal nodal forces is equal to

$$\mathbf{F} = \sum_m \Delta \mathbf{F}^{(m)} \tag{44}$$

where m is the load-step index and $\Delta \mathbf{F}^{(m)}$ represents the increment of internal nodal forces at load step m. Differentiating Eq. (44) with respect to design variable A_j gives,

$$\frac{\partial \mathbf{F}}{\partial A_j} = \sum_m \frac{\partial \Delta \mathbf{F}^{(m)}}{\partial A_j} = \sum_m \frac{\partial \left[\sum_{k=1}^{n_e} \left(\mathbf{T}_k^T \mathbf{K}_k^{(m)} \mathbf{T}_k \cdot \Delta \mathbf{u}^{(m)} \right) \right]}{\partial A_j} = \sum_m \left[\sum_{k=1}^{n_e} \left(\mathbf{T}_k^T \frac{\partial \mathbf{K}_k^{(m)}}{\partial A_j} \mathbf{T}_k \Delta \mathbf{u}^{(m)} \right) \right] \tag{45}$$

where: $\mathbf{T}_k$ is the direction-cosine matrix for member k; $\Delta \mathbf{u}$ is the vector of incremental nodal displacements; $\mathbf{K}_k$ is the stiffness matrix for element k; and from Eq. (1),

$$\frac{\partial \mathbf{K}_k^{(m)}}{\partial A_j} = \frac{\partial \mathbf{S}_k}{\partial A_j} \mathbf{C}_{sk}^{(m)} + \mathbf{S}_k \frac{\partial \mathbf{C}_{sk}^{(m)}}{\partial A_j} + \frac{\partial \mathbf{G}_k^{(m)}}{\partial A_j} \mathbf{C}_{gk}^{(m)} + \mathbf{G}_k^{(m)} \frac{\partial \mathbf{C}_{gk}^{(m)}}{\partial A_j} \tag{46}$$

where: $\partial \mathbf{C}_{sk}/\partial A_j$ and $\partial \mathbf{C}_{gk}/\partial A_j$ are the derivatives of correction matrices $\mathbf{C}_{sk}$ and $\mathbf{C}_{gk}$, respectively [32]; $\partial \mathbf{S}_k/\partial A_j$ and $\partial \mathbf{G}_k/\partial A_j$ are the derivative of elastic stiffness matrix $\mathbf{S}_k$ and geometric stiffness matrix $\mathbf{G}_k$, respectively.

By assuming $\partial \mathbf{K}_k^{(m)}/\partial A_j = 0$ if $k \neq j$ [32] and expanding Eq. (46) in terms of plasticity factors, the sensitivity of displacement μ_l is then derived from Eqs. (43) and (44) as

$$\frac{d\mu_l}{dA_j} = \mathbf{U}_l^T \frac{d\mathbf{P}}{dA_j} - \mathbf{U}_l^T \sum_m \left\{ \mathbf{T}_j^T \left[\frac{\mathbf{S}_j \mathbf{C}_{sj}^{(m)}}{A_j} + \sum_{n=1}^2 \left(\mathbf{S}_j \frac{\partial \mathbf{C}_{sj}^{(m)}}{\partial p_{jn}^{(m-1)}} + \mathbf{G}_j^{(m)} \frac{\partial \mathbf{C}_{gj}^{(m)}}{\partial p_{jn}^{(m-1)}} \right) \right] \bullet \right.$$
$$\left. \left(\frac{\left(p_{jn}^{(m-1)} - 1 \right) p_{jn}^{(m-1)}}{A_j} + \frac{\left(1 - p_{jn}^{(m-1)} \right)^2 L_j}{3EI_j} \frac{\partial R_{jn}^{p(m-1)}}{\partial A_j} \right) \right] \mathbf{T}_j \Delta \mathbf{u}^{(m)} \right\} \tag{47}$$

where: p_{jn} is the plasticity-factor in Eq. (2) for element j at end n ($n=1$ or 2); $\partial R_{jn}^{P}/\partial A_j$ is the derivative of rotational stiffness of the plastic hinge for element j at end n; and superscript $(m-1)$ is load step index. See [32] for detailed derivation of Eq. (47).

Equation (47) reduces to the well-known static elastic displacement sensitivity formulation when $p_{jn}=1$, $m=1$, and $d\mathbf{P}/dA_j=0$; i.e.,

$$\frac{d\mu_l}{dA_j} = -\frac{1}{A_j} \mathbf{U}_l^T \left(\mathbf{T}_j^T \mathbf{K}_j \mathbf{T}_j \right) \mathbf{u} \tag{48}$$

The sensitivity of overall nodal load vector, $d\mathbf{P}/dA_j$ in Eq. (47), is found from Eq. (12) as,

$$\frac{d\mathbf{P}}{dA_j} = \mathbf{D} \frac{d\mathbf{P}_l}{dA_j} + \frac{d\mathbf{P}_g}{dA_j} = \mathbf{D} \frac{d\mathbf{P}_l}{dA_j} \tag{49}$$

where $d\mathbf{P}_g/dA_j=0$ since the $\mathbf{P}_g$ load vector is constant for pushover analysis, and $d\mathbf{P}_l/dA_j$ is found by differentiating Eq. (9) with respect to the design variable A_j, to get,

$$\frac{d\mathbf{P}_l}{dA_j} = \frac{dV_b}{dA_j} \mathbf{C}_v \tag{50}$$

where dV_b/dA_j is the sensitivity of the design base shear which, from Eqs. (7) and (8), is found as,

$$\frac{dV_b}{dA_j} = \frac{W}{g} \frac{\partial S_a}{\partial T} \frac{dT}{dA_j} = \begin{cases} 0 & T \le T_0 \\ -\frac{W}{g} \frac{S_1}{T^2} \frac{dT}{dA_j} & T > T_0 \end{cases} \tag{51}$$

in which, from Eq. (11),

$$\frac{dT}{dA_j} = \sum_{s=1}^{n_s} \frac{\partial T}{\partial v_s} \frac{dv_s}{dA_j} = \sum_{s=1}^{n_s} \frac{2\pi^2}{T \sum_{t=1}^{n_s} \left(V_1 C_{v,t} v_t \right)} \left(2 m_s v_s - \frac{T^2 V_1 C_{v,s}}{4\pi^2} \right) \frac{dv_s}{dA_j} \tag{52}$$

In Eq. (52): $C_{v,t}$ is the inertia load distribution factor at story level t (see Eq. (10)); v_t is story drift under the action of base shear V_1 at story level t; and dv_s/dA_j is the static elastic sensitivity of story drift v_s, since V_1 is a constant, and is found from Eq. (48).

Then, the sensitivity of objective function f_2 is found as:

$$\frac{df_2}{dA_j} = \sum_{s=1}^{n_s-1} \left(\frac{\partial f_2}{\partial v_s} \frac{dv_s}{dA_j} \right) + \frac{\partial f_2}{\partial \Delta} \frac{d\Delta}{dA_j} \tag{53}$$

where:

$$\frac{\partial f_2}{\partial v_s} = \frac{1/H_s}{n_s f_2 (\Delta/H)} \left(\frac{v_s/H_s}{\Delta/H} - 1 \right) \tag{54}$$

and

$$\frac{\partial f_2}{\partial \Delta} = \frac{1}{n_s f_2} \sum_{s=1}^{n_s-1} \left(\frac{v_s/H_s}{\Delta/H} - 1 \right) \left(-\frac{v_s/H_s}{\Delta^2/H} \right) \tag{55}$$

Finally, the sensitivity of a general structural response R_s with respect to reciprocal variable x_j can be restored from

$$\frac{dR_s}{dx_j} = \frac{dR_s}{dA_j}\frac{dA_j}{dx_j} = -A_j^2\frac{dR_s}{dA_j} \qquad (56)$$

where a general structural response R_s can be drift v_s or Δ, or period T, or design base shear V_b, or objective function f_2, etc.

5.   OPTIMAL DESIGN PROCEDURE

In summary, the overall design procedure is described step-by-step in the following:

(1) Input geometry of the structure, such as bay size and story height, etc. Input design spectrum (Eq. (8)), constraint limits (i.e., $\overline{\Delta}$ and $\overline{\delta}$), seismic weights (W and G_s), and the number of design variables n_e. Set design iteration index $i=0$.

(2) Assume initial member sizes $\mathbf{x}_i$. Recover section properties from the section databank (AISC Manual [23] is adopted for this study).

(3) Set design phase index $PI=1$ (i.e., continuous optimization)
(3.1)   Stage One
    (3.1.1)   Set design iteration index $i=i+1$. Calculate f_1 value for current design.
    (3.1.2)   Apply base shear V_1 to the structure with no gravitational loads, and conduct elastic analysis to compute the period T by Eq. (11), the acceleration response S_a by Eq. (8), and the design base shear V_b by Eq. (7).
    (3.1.3)   Perform pushover analysis to evaluate the structural responses under design base shear V_b.
    (3.1.4)   Calculate sensitivities $d\Delta/dx_j$ and $d\delta_s/dx_j$ using Eq. (47).
    (3.1.5)   Formulate design optimization problem, Eqs. (29), (31) to (34).
    (3.1.6)   Apply the Dual method [21] to search for an improved design, $\mathbf{x}_{i+1}$.
    (3.1.7)   Check the convergence criteria for the design point $\mathbf{x}_{i+1}$. If $\mathbf{x}_{i+1}$ is not convergent, update section properties according to Eqs. (15) to (18), and go back to step 3.1.1. If $\mathbf{x}_{i+1}$ is found to be convergent (e.g., the difference of structural weight between two consecutive cycles is less than 0.3%), terminate Stage One and proceed to Stage Two at step 3.2.
(3.2)   Stage Two
    (3.2.1)   Repeat Step 3.1.1 to 3.1.3.
    (3.2.2)   Calculate f_2 value for current design. Check the convergence criteria (e.g., the improvement of f_2 value for three consecutive cycles is less than 1%). If $\mathbf{x}_i$ is not convergent, go to step 3.2.3. If $\mathbf{x}_{i+1}$ is found to be convergent, terminate Stage Two and proceed to Phase II at step 4.
    (3.2.3)   Calculate sensitivities df_2/dx_j, $d\Delta/dx_j$ and $d\delta_s/dx_j$.
    (3.2.4)   Formulate design optimization problem, Eqs. (30) to (34).
    (3.2.5)   Apply the Dual method to search for an improved design, $\mathbf{x}_{i+1}$.
    (3.2.6)   Go to step 3.2.1

(4)   Set design phase index $PI=2$ (i.e., discrete optimization).
(4.1)   Select one or a few variables to be assigned to their nearest upper discrete sizes, and

compute the number of design variables remaining to be assigned a discrete size.

(4.2)   If no design variable remains to be assigned to a discrete size, stop the discrete optimization and go to step 5; otherwise, proceed to step 4.3.

(4.3)   Update sectional properties for discrete-size sections (i.e., the design variables that have already been assigned a discrete size) from the section databank; update properties of continuous-size sections (i.e., the design variables that remain to be assigned a discrete size) through Eqs. (15) to (18).

(4.4)   Perform Stage One and Stage Two optimization (i.e., redo steps 3.1 and 3.2) for the remaining continuous variables.

(4.5)   Go to step 4.1.

(5)   Perform pushover analysis for the obtained optimal design. Output the results of the design optimization (i.e., optimal discrete section sizes A_j, structural weight f_1, coefficient of variation of the inelastic story drift distribution f_2, member-end plasticity factors p, inter-story drifts δ_s, internal member forces, etc.).

6.   DESIGN EXAMPLE

A nine-story rigid moment frame in Figure 4, which was studied by Hasan et al. [7], is adopted as the design example. All five bays are 9.14 m wide (centerline dimensions) and all stories are each 3.96 m high except the first story is 5.5 meters high. The lumped seismic weights for the frame are 4942 kN for the first floor level, 4857 kN for each of the second to eighth floor levels, and 5231 kN for the roof level. Constant gravity loads of 32 kN/m are applied to the beams in the first to eighth floor levels, while 29 kN/m are applied to the roof beams.

The frame consists of 99 members. Through member grouping, the number of design variables is reduced to 19, designated as A_1 to A_{19} in Figure 4. Member grouping is a technique to simulate construction practice in addition to reduce the number of design variables. For example, member grouping is used to mimic tier columns, as shown by column section A_2 in Figure 4. It is a common practice to design all the beams on the same floor level using one cross section, as illustrated by A_{12} in Figure 4. Therefore, this member grouping technique can take cost effective practices into account. On the other hand, member grouping, which can reduce the number of design variables significantly, makes the design optimization algorithm more efficient. Member grouping does not affect all the equations except Eqs. (13) and (56) where a few symbols need to be redefined.   For Eq. (13), n_e is redefined as the number of design variables and L_j the sum of the length of each individual member whose cross section is grouped as design variable j. For Eq. (56), dR_s/dx_j is the sum of the sensitivities of R_s with respect to each individual member whose cross section is design variable j.

During the design process, it is required to employ Eqs. (15) to (18) to express section properties I_j, S_j and Z_j in terms of A_j for each of the $j=1,2, \ldots, 19$ section variables. To this end, it is predetermined that the column design variables A_1 through A_{10} are chosen from among available W14 sections, while beams A_{11} to A_{13}, A_{14} to A_{16}, and A_{17} to A_{19} are chosen from among W36, W30, and W24 sections [23], respectively. While providing considerable *a-priori* knowledge to the design automation algorithm, such predetermination is entirely consistent with conventional design practice where a designer generally knows which type of section and approximate nominal depth is used for a certain type of frame member. For instance, it is well known that W14 sections are commonly used sections for columns, while W24 to W36 sections are often used for beams. If a reasonable section is not able to be chosen from among the predetermined sections to meet the

design requirements, the predetermined sections are upgraded to a larger available nominal depth and the member design process is repeated.
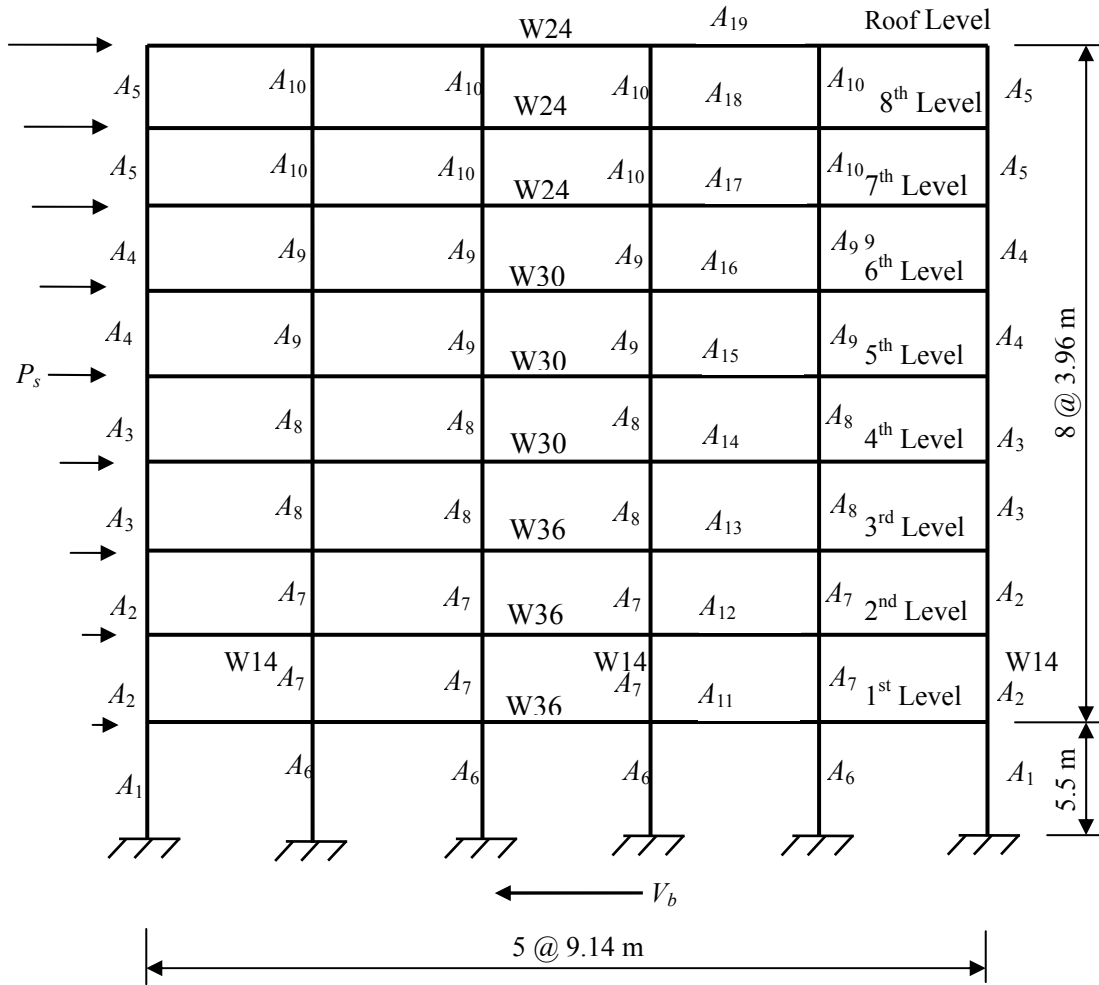
Figure 4. Nine-story Moment Frame

For this study, the initial design point is taken to be defined by the maximum available commercial section sizes for the design variables, i.e., A_1^0 to A_{10}^0 are defined by a W14×808 section, while A_{11}^0 to A_{13}^0, A_{14}^0 to A_{16}^0, and A_{17}^0 to A_{19}^0 are defined by W36×848, W30×477, W24×492 sections, respectively (see Table 2). The maximum weight of the structure is W_{max}=6268 kN, which, in turn, is used to normalize the weight objective function f_1. The lower bounds of design variables are also given in Table 2.

Table 2. Bounds on Member Sizes

Section Shapes	Lower/Upper Section Size	Cross-Section Area A_i (mm²)
W14	W14×22	4190
	W14×808	152900
W24	W24×55	10450
	W24×492	92900
W30	W30×90	17030
	W30×477	90320
W36	W36×135	25610
	W36×848	160640

All the columns use ASTM A572-Grade 50 steel (The nominal yield strength is σ_y=345 MPa and the expected yield strength is $\sigma_{ye} = R_y \sigma_y = 1.1 \times 345 = 380$ MPa, [25]), while all the beams use A36 steel ($\sigma_y = 248$ MPa and $\sigma_{ye} = 1.5 \times 248 = 372$ MPa).

Design spectrum Eq. (8) is assumed to be as shown in Figure 5. It is expected the obtained design will have $T > T_0$; i.e., the design base shear V_b will change during the design process. The lateral force pattern is determined by Eq. (10) where λ is arbitrarily taken to be 2. The direction of lateral forces is given in Figure 4. The allowable roof drift is taken as the target displacement, which is approximate 0.05 of the building height [6]. Allowable inter-story drift $\bar{\delta}$ is taken to be $0.062h$ [27], where h is the height of the story under consideration.
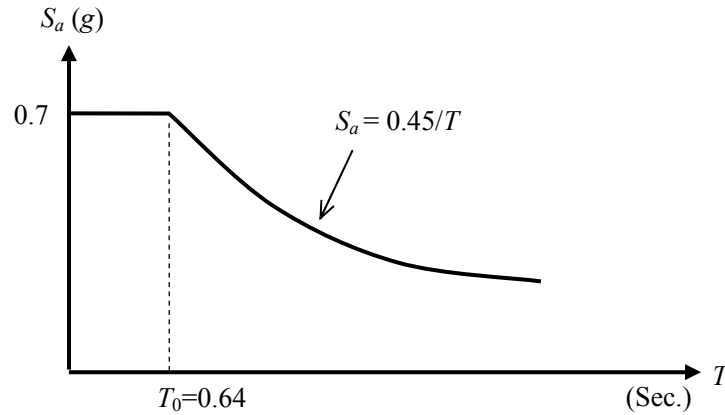

Figure 5. Inelastic Acceleration Response Spectrum

For pushover analysis, each beam member is modeled by four beam elements (i.e., single stress yield condition), while each column is represented by a single beam-column element (i.e., combined stress yield condition). Using one element to model a column will not produce unacceptable error in this study since axial forces in columns of a moment frame are normally far below 40% of the Euler's buckling load [33].

Two runs (i.e., Runs A and B in Table 3) without and with imposing SC/WB constraints to the moment frame are executed to search for optimal solutions (given in Table 3), which are referred to as Designs A and B, respectively. Note that all the commercial standard sections in Table 3 are the type of compact for developing plastic hinges.

Design A, without SC/WB constraints imposed, has a normalized value of the weight objective f_1=0.258 (i.e., the weight of the optimal discrete-section frame is $f_1 \times W_{max}$ = 0.258×6268 = 1616 kN) and a value of f_2=0.03 (i.e., the coefficient of variation of story drift). The elastic period of Design A is 2.26 seconds. The plastic state of Design A under the design base shear V_b=8790 kN is found to be as shown in Figure 6, where ovals represent plastic hinges at member ends and the digit inside ovals represents the percentage of plastification (expressed as $100(1-p)$, where p is defined by Eq. (2)). As indicated by Figure 6, the first, second, fourth, sixth, and eighth stories have only marginal strength safety against formation of story mechanism, since almost all the columns in these stories have nearly full plastic hinges at both ends. It is noted that these relatively weak stories are where columns splice, i.e., the places where the section size of the columns is reduced abruptly (the first story is seen as a special place where the columns splice). This phenomenon of having relatively weak story in Design A does not conflict with the second design objective, because concentration of interstory drift does not exist based on the pushover analysis results. This phenomenon also illustrates that it is impossible to eliminate story mechanism absolutely under extreme earthquake hazards if SC/WB constraints are not imposed to the design problem.

Table 3. Discrete Design Results of the Nine-story Moment Frame

Design runs	A: No SC/WB	B: With SC/WB
Design variables	Designation A_j (mm^2)	Designation A_j (mm^2)
$j= 1$	W14×311 58970	W14×342 65160
2	W14×233 44190	W14×283 53740
3	W14×193 36640	W14×283 53740
4	W14×176 33420	W14×233 44190
5	W14×145 27550	W14×211 40000
6	W14×455 86450	W14×500 94830
7	W14×342 65160	W14×398 75480
8	W14×311 58970	W14×370 70320
9	W14×257 48770	W14×311 58970
10	W14×145 27550	W14×283 53740
11	W36×170 32250	W36×170 32250
12	W36×150 28510	W36×150 28510
13	W36×150 28510	W36×135 25610
14	W30×148 28064	W30×173 32770
15	W30×148 28064	W30×148 28064
16	W30×124 23550	W30×108 20450
17	W24×117 22190	W24×103 19550
18	W24×68 12960	W24×94 17870
19	W24×55 10450	W24×62 11740
Weight (kN)	1616	1846

Design B, with SC/WB constraints imposed, has f_1=0.294 (i.e., the weight of the optimal design is $f_1 \times W_{max}$ = 0.294×6268 = 1846 kN) and f_2=0.04. The elastic period of Design B is 2.14 seconds. The plastic state of Design B under V_b=9288 kN is found to be as shown in Figure 7. For this example, SC/WB constraints lead to a heavier optimal design. It is seen from Figure 7 that no soft or weak story exists in Design B. It is noted that the SC/WB constraints cannot prevent individual columns

from yielding even moment ratios r_{cb} at almost all connections are greater than or equal to unity (see Figure 8, where the moment ratios r_{cb} at connections are shown inside ovals. Note that the discrimination between axial tension and compression forces in computing column moment capacity in Eq. (21)). However, it is evident from Figure 7 that beam yielding dominates when the SC/WB constraints are imposed. In reality, a yielding pattern such as that in Figure 7 will most likely eliminate any soft or weak story collapse.

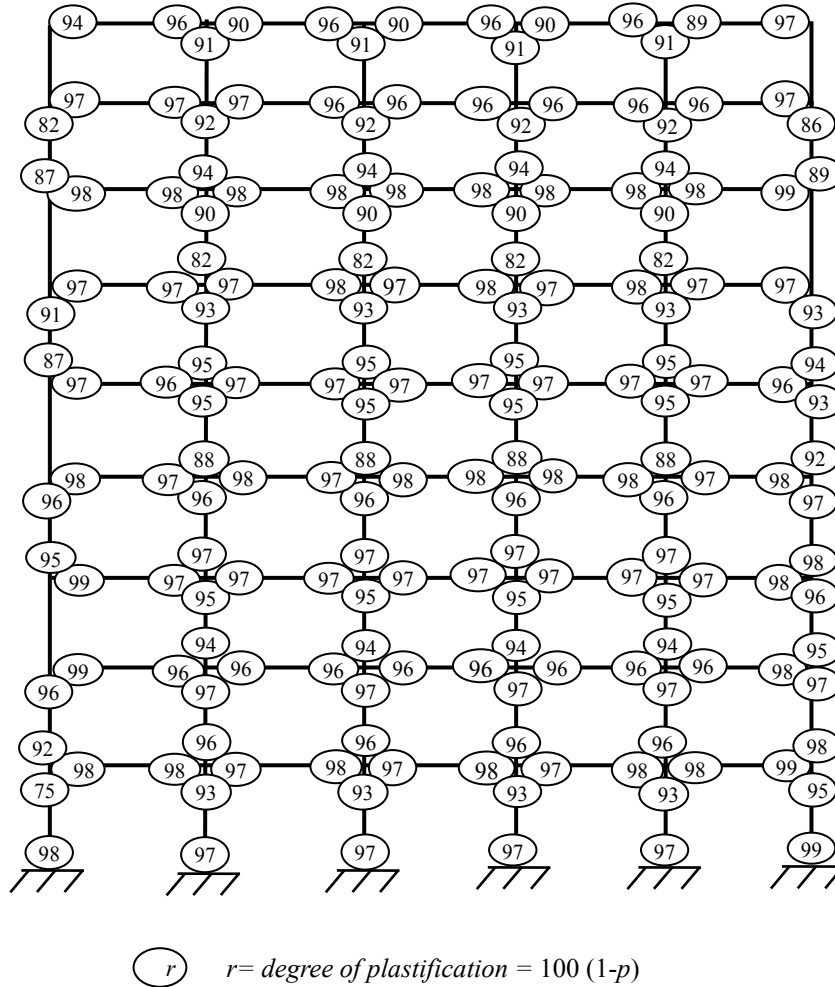$\bigcirc r \quad r= degree\ of\ plastification = 100\ (1\text{-}p)$

Figure 6. Structural Plastification of Design A

The plastic interstory drifts of Designs A and B are given in Table 4. These drift distributions are deemed to be nearly uniform and satisfactory for design. It is generally unlikely to obtain an optimal design with f_2=0 due to the following reasons: 1) the cross sections are discrete variables; 2) the errors in computing sensitivity information are unavoidable [32]; 3) the plastic deflections are extremely sensitive to the change of sectional size (a plastic deflection is usually two orders of magnitude more sensitive than an elastic deflection [31]). For Run A, f_2 =0.03 is the best found by the design algorithm, while for Run B f_2 =0.04 is the optimal. Note that having a smaller f_2 value does not mean Design A is a better solution than Design B. Designs A and B are the optimal solutions under two different sets of constraints (one has SC/WB constraints and the other has not) respectively, thus, it cannot be said that Design A possess a more uniform ductility response than Design B.

Table 4. Interstory Drift Distributions of the Nine-story Moment Frame

Design runs	A: No SC/WB	B: With SC/WB
Story level	Drift ratio	Drift ratio
1	0.040	0.042
2	0.045	0.045
3	0.033	0.047
4	0.054	0.045
5	0.040	0.042
6	0.043	0.055
7	0.037	0.055
8	0.046	0.046
9	0.033	0.033
f_2	0.03	0.04

For member plastification taken as a measure of damage, it is observed from Figures 6 and 7 that damage is somewhat uniformly distributed over all stories of the structures where the frames undergo nearly uniform interstory drift (i.e., as desired, there is no significant concentration of plastic deformation). This phenomenon illustrates the close correlation between the inelastic interstory drift and the structural plastic state. The corresponding pushover capacity curves for Designs A and B are drawn in Figure 9. The global ductility demands can be determined from these curves, which should not exceed the target ductility limit.
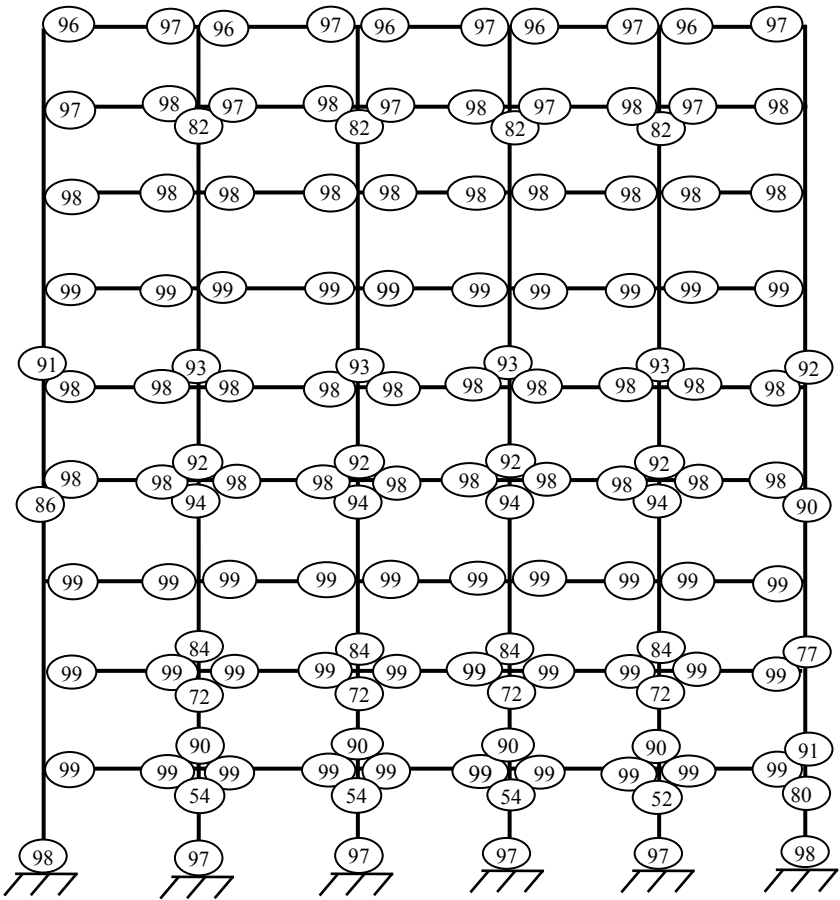

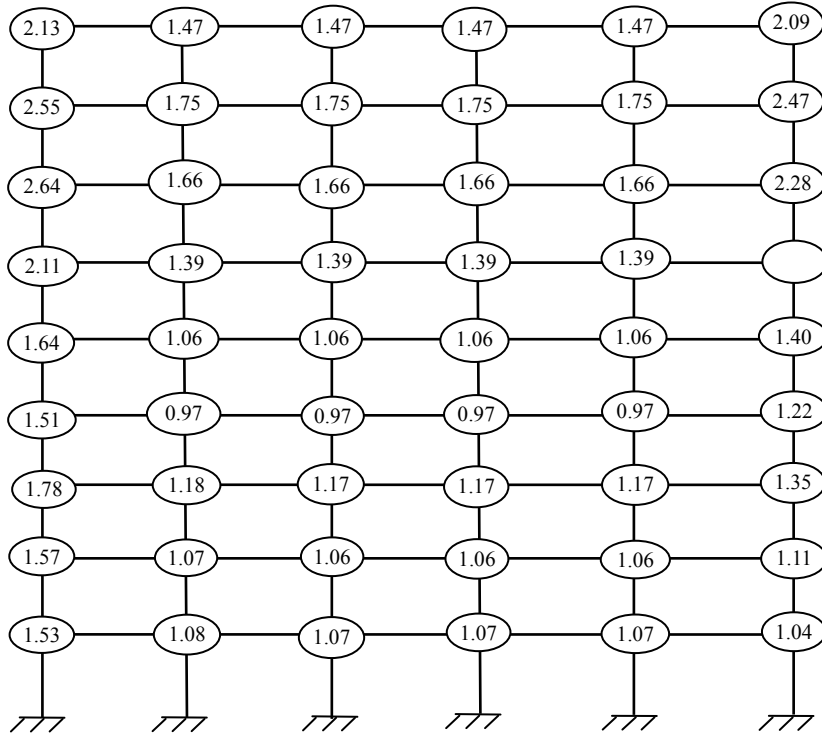Figure 7. Structural Plastification of Design B

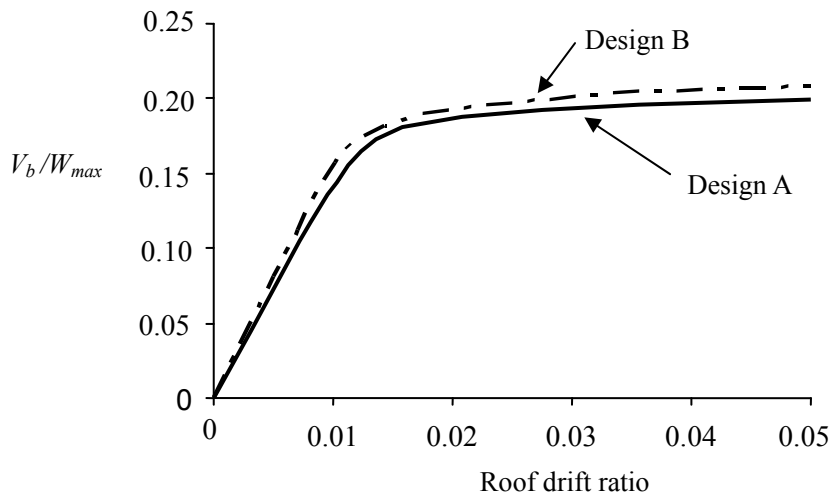Figure 8. Column-beam Moment Ratios at Connections of Design B

Figure 9. Pushover Capacity Curves for Optimal Designs

Design histories of the normalized structural weights for Runs A and B are illustrated in Figure 10. Phase I (i.e., continuous optimization) ends at iterations 28 and 36 for Runs A and B, respectively. In the early stage of the design history (the first 12 iterations for Run A and the first 15 iterations for Run B), the structural weight decreases rapidly since the design points are in the elastic or in the insignificant inelastic range under the design base shear (note that design base shear is a function of the period, which in turn is a function of the design variables). The convergence becomes much slower in the latter stage of the design history, as the weight of the structure decreases and the structure undergoes significant plastification while the inelastic drifts approach active. This slow convergence results from the fact that inelastic displacements are extremely sensitive to the changes in sectional sizes [32]. Therefore, it is necessary to maintain small changes in sectional sizes from

one design iteration to the next. For strategies to minimize f_2 and more details of numerical realization of the design algorithm, see [21].
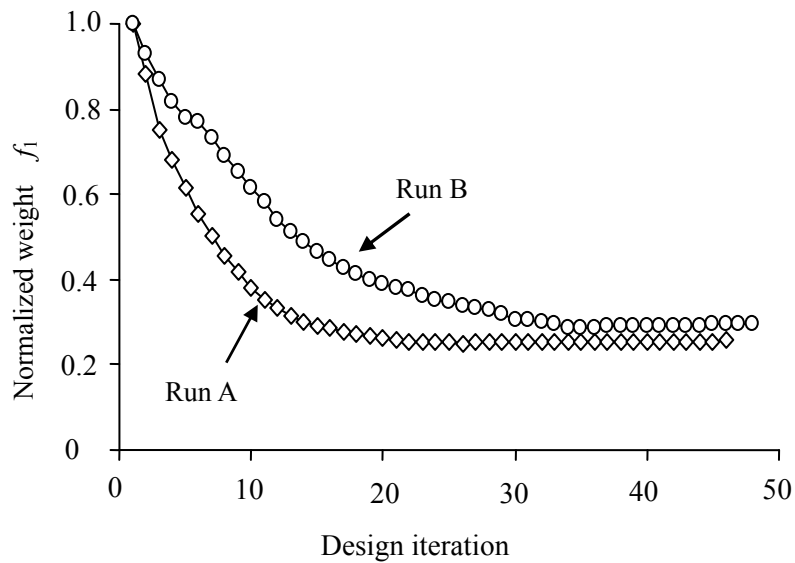

Figure 10. Design Histories of Normalized Structural Weight

7.   DISCUSSIONS AND CONCLUSIONS

This paper presented a design optimization algorithm for steel moment frames under extreme earthquake loading. A pushover analysis procedure was used to evaluate seismic responses. Minimum structural cost and uniform ductility demand were taken as the design criteria. A two-stage design strategy was proposed to conduct the multi-objective optimization. In the first stage, a minimum-weight design was obtained subject to drift and side constraints (and SC/WB constraints for special moment frames). In the second stage, an optimal design with an improved ductility distribution over the minimum-weight design was obtained. This two-stage strategy eliminates the necessity of combining the two design objectives into one. The applicability and practicability of the developed optimization method was demonstrated for the design of a nine-story moment frame.

The heightwise ductility demand of a building framework is mainly dependent upon the heightwise distribution of structural stiffness (and strength) and the profile of the applied lateral inertia earthquake loads (the selection of appropriate lateral load profile is equally important to achieve the uniform ductility demand objective. However, it is beyond the scope of this paper and not discussed herein). Therefore, the proposed design formulation seeks an optimal lateral stiffness distribution for moment frames with a weight as small as possible.

It is observed from the design example that moment frames with a nearly uniform interstory drift distribution have somewhat uniform plastification over the structure height under the extreme earthquake loading. Specifically, the benefit of the SC/WB concept is that the columns are designed strong enough such that flexural yielding in beams generally dominates at multiple levels of the framework, thereby achieving a reduced likelihood of a soft or weak story and a higher level of energy dissipation. However, it is evident that SC/WB concept cannot prevent column ends from forming plastic hinges.

While pushover analysis is widely accepted as a nonlinear procedure to evaluate seismic demands, it is not shortcoming free. The pros and cons of pushover analysis have been well discussed by Krawinkler et al. [6] and Elnashai [8]. Future endeavors are desirable in two lines for applying pushover analysis in seismic design: 1) the improvement of pushover analysis in its capability of predicting seismic demands for a general structure as consistently as possible with dynamic response analysis (a pilot study in this direction can be found in [34]); and 2) the adoption of advanced analysis techniques [33] to the domain of seismic design.

8.   APPENDIX: ILLUSTRATION OF EQUATION (12): $\mathbf{P} = \mathbf{D}\, \mathbf{P}_l + \mathbf{P}_g$

Consider the planar two-story moment framework shown in Figure 11. The framework has six nodes and, since each node has three degrees of freedom, the overall (gravity + lateral) nodal load vector $\mathbf{P}$ and nodal gravity load vector $\mathbf{P}_g$ each have dimension = 18×1. From Figure 11, the vector of nodal lateral loads applied at the two story levels $\mathbf{P}_l=\{P_1, P_2\}^T$ has dimension= 2×1, where loads P_1 and P_2 correspond to the 7th and 13th degrees of freedom of the structure. Therefore, the Boolean matrix $\mathbf{D}$ has dimension = 18×2 and is of the form:

$$\mathbf{D} = \begin{Bmatrix} 0 & 0 & 0 & 0 & 0 & 0 & 1 & 0 & 0 & 0 & 0 & 0 & 0 & 0 & 0 & 0 & 0 & 0 \\ 0 & 0 & 0 & 0 & 0 & 0 & 0 & 0 & 0 & 0 & 0 & 0 & 1 & 0 & 0 & 0 & 0 & 0 \end{Bmatrix}^T$$
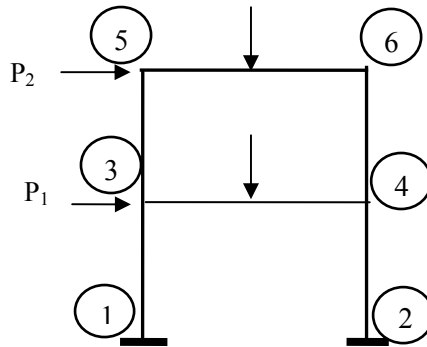

Figure 11. Two-story Moment Frame

REFERENCES

[1]   BSSC, "NEHRP Recommended Provisions for Seismic Regulations for New Buildings and Other Structures (FEMA 450)", Building Seismic Safety Council, Washington DC, 2004.

[2]   NRC, "National Building Code of Canada 1995", Associate Committee on National Building Code, National Research Council, Ottawa.

[3]   Bruneau, M., Uang, C.M. and Whittaker, A., "Ductile Design of Steel Structures", McGraw-Hill, 389, 1998.

[4]   Chopra, A.K., "Dynamics of Structures: Theory and Applications to Earthquake Engineering", Prentice Hall, 726, 2001.

[5]   Federal Emergency Management Agency, FEMA-356, "Prestandard and Commentary for the Seismic Rehabilitation of Buildings", ASCE, Reston, Virginia, 2000.

[6]   Krawinkler, H. and Seneviratna, G.D.P.K., "Pros and Cons of a Pushover Analysis of Seismic Performance Evaluation", Eng. Struct., 1998, Vol. 20, pp. 452-464.

[7]   Hasan, R., Xu, L. and Grierson, D.E., "Pushover Analysis for Performance-based Seismic Design", Comp. Struct., 2002, Vol. 80, No. 31, pp. 2483-2493.

[8]   Elnashai, A.S., "Do We Really Need Inelastic Dynamic Analysis", J. Earthquake Eng., 2002, Vol. 6, Special Issue 1, pp. 123-130.

[9]   Kirsch, U., "Structural Optimization: Fundamentals and Applications", Springer-Verlag, 1993.

[10]   ASCE, "Recent Advances in Optimal Structural Design", Edited by Scout B., ASCE, 2002.

[11]   Ganzeri, S., Pantelides, C.P. and Reaveley, L.D., "Performance-based Design Using Structural Optimization", Earthquake Eng. Struct. Dyn., 2002, Vol. 29, pp. 1677-1690.

[12]   Chan, C-M. and Zou, X-K., "Elastic and Inelastic Drift Performance Optimization for Reinforced Concrete Buildings Under Earthquake Loads", Earthquake Eng. Struct. Dyn., 2004, Vol. 33, pp. 929-950.

[13]   Liu, M., Burns, S.A. and Wen, Y.K., "Multiobjective Optimization for Performance-based Seismic Design of Steel Moment Frame Structures", Earthquake Eng. Struct. Dyn., 2005, Vol. 34, pp. 289-306.

[14]   Xu. L, Gong, Y. and Grierson, D.E., "Seismic Design Optimization of Steel Building Frameworks", J. Struct. Eng., ASCE, 2006, Vol. 132, No. 2, pp. 277-286.

[15]   Haftka, R.T., "Integrated Nonlinear Structural Analysis and Design", AIAA Journal, 1989, Vol. 27, No. 11, pp. 1622-1627.

[16]   Foley, C.M. and Schinler, D., "Automated Design of Steel Frames Using Advanced Analysis and Object-oriented Evolutionary Computation", J. Struct. Eng., 2003, Vol. 129, No. 5, pp. 648-660.

[17]   Gong, Y., "Optimal Stiffness Distribution of Steel Moment Frames Under Extreme Earthquake Loading", Advances in Structural Engineering, 2005, Vol. 8, No. 6, pp. 573-584.

[18]   McGuire, W., Gallagher, R.H. and Ziemian, R.D., "Matrix Structural Analysis", 2nd ed., John Wiley & Sons, 2000.

[19]   Cohn, M.Z., "Analysis and Design of Inelastic Structures – Volume 2: Problems, University of Waterloo Press, Ontario, Canada, 1972.

[20]   CSA, "S16-01: Limit States Design of Steel Structures", Canadian Standards Association, Ontario, Canada, 2001.

[21]   Gong, Y., "Performance-based Design of Steel Building Frameworks Under Seismic Loading", PhD Thesis, University of Waterloo, Canada.

[22]   Wen, Y.K. and Kang, Y.J., "Design Criteria Based on Minimum Expected Life-cycle Cost", Structural Engineering World Wide, Paper No: T132-2, Elsevier Science, 1998.

[23]   AISC, "Manual of Steel Construction, Load & Resistance Factor Design", Vol. I, 2nd ed., AISC, 1994.

[24]   Foutch, D.A. and Yun, S.Y., "Modeling of Steel Moment Frames for Seismic Loads", J. Construct. Steel Research, 2002, Vol. 58, pp. 529-564.

[25]   AISC, "Seismic Provisions for Structural Steel Buildings", American Institute of Steel Construction, 2002.

[26]   Chan, C-M., Grierson, D.E. and Sherbourne, A.N., "Automatic Optimal Design of Tall Steel Building Frameworks", J. Struct. Eng., 1995, Vol. 121, No. 5, pp. 838-847.

[27]   Federal Emergency Management Agency, "Recommended Seismic Design Criteria for New Steel Moment-frame Buildings", FEMA-350, SAC Joint Venture, 2000.

[28]   Arora, J.S., "Methods for Discrete Variable Structural Optimization, Recent Advances in Optimal Structural Design, Edited by Scout B, ASCE, 2002.

[29]   Schmit, L.A. and Farshi, B., "Some Approximation Concepts for Structural Synthesis", AIAA Journal, 1974, Vol. 12, No. 5, pp. 692-699.

[30]   Fleury, C., "Structural Weight Optimization by Dual Methods of Convex Programming", Int. J. Numer. Meth. Engng., 1979, Vol. 14, pp. 1761-1783.

[31]   Gong, Y., Xu, L. and Grierson, D.E., "Performance-based Design Sensitivity Analysis of Steel Moment Frameworks Under Seismic Loading", Int. J. Numer. Meth. Engng., 2005, Vol. 63, pp. 1229-1249.

[32]   Gong, Y., Xu, L. and Grierson, D.E., "Sensitivity Analysis of Steel Moment Frames Accounting for Geometric and Material Nonlinearity", Comp. & Struct., 2006, Vol. 84, No. 7, pp. 462-475.

[33]   Chan, S.L., "Non-linear Behaviour and Design of Steel Structures", J. Construct. Steel Research, 2001, Vol. 57, pp. 1217-1231.

[34]   Grierson, D.E., Gong, Y. and Xu, L., Optimal Performance-based Seismic Design Using Modal Pushover Analysis", J. Earthquake Eng., 2006, Vol. 10, No. 1, pp. 73-96.

SIMPLIFIED APPROACH TO EVALUATION OF STEEL BEAM-COLUMN FIRE RESISTANCE

M. Maślak

Assistant Professor, Department of Civil Engineering,
Cracow University of Technology, 31-155 Cracow, Warszawska 24, Poland
(Corresponding author: E-mail: mmaslak@pk.edu.pl)

ABSTRACT: The approach, presented in this paper, allows a designer to assess the value of steel member fire resistance if unlimited thermal deformations are restrained. The beam analysed in the example is subject to bending in persistent design situation; whereas, under the influence of fire temperature, additional compression force occurs. The fire resistance of structural element depends on the degree of restraints. Large flexural stiffness of columns which bound the beam leads to the relatively small value of beam fire resistance. Alternatively, if their stiffness is lower (deformability is greater) the reduction of member fire resistance in relation to the beam with fully unrestrained thermal deformations is also softer. Results obtained in the presented analysis should be interpreted only as an approximation of real values. More accurate solutions can be reckoned only if rheological effects, particularly creep of steel, are taken into account.

Keywords: beam-column; fire; temperature; fire resistance; thermal deformation

1. INTRODUCTION

The fire resistance $t_{fi,d}$ of structural member is the length of time calculated from fire flashover during which it is capable to carry imposed loads under fire conditions. Its reliable prediction is necessary to correctly select member fire protection parameters. Making separate structural analysis is the only way to accurately evaluate its value. However, a designer has to take into consideration the fact that such resistance depends not only on the stress level in member cross-section in the moment of fire flashover but also on the degree of restraints of the member prospective thermal deformations.

In accidental fire situation in structural members a complex state of stress is commonly generated. Always, if unlimited thermal deformations are restrained in any way, thermally induced additional internal forces and moments must occur. For this reason many of structural elements are subject to simultaneous bending and compression, even if only pure bending could be taken into consideration in persistent design situation. The methodology of simplified fire resistance assessment of such a steel member is presented in the paper on the example of uniformly heated, multistory frame primary beam with fully flexible beam-to-column connections (figure 1).

Beam thermal elongation is constrained by column flexural stiffness; consequently, additional thermally induced compression force $N_{c,\Theta}$ is generated. Support deformability on horizontal displacement has the essential influence on beam behaviour during fire. Values $1/K_L$ and $1/K_R$ are adopted as its measure for the left (L) and the right (R) support respectively. It means that for the whole beam we have $1/K = (1/K_L + 1/K_R)$. Assumption that both supports are fully flexible has been accepted for simplicity and clarity of analysis. Study of moment redistribution with participation of additional thermally induced internal forces and moments, although extremely interesting, goes beyond the limits of this article. Member temperature growth is always followed by its adequate stiffness reduction; however, the rate of increase of beam temperature does not have to be the same as of the columns. Therefore, the beam to column stiffness ratio should be modified

in particular fire moments t_{fi}. Nevertheless, if bending moment caused by all imposed loads (without any thermal influences) summed according to accidental load combination rule is not distributed from the beam to adjacent columns, its value does not depend on the beam temperature and remains constant in the whole of fire duration (any load changes generated by evacuation of occupants or furnishings combustion are not taken into consideration).

Additional simplified assumption has been made that the steel temperature Θ_a distribution for particular fire moment t_{fi} is uniform not only in each beam section but also along the whole of its length. In general frame beams adjoin massive reinforced concrete floor slab with a great thermal capacity. For this reason in real fires their top flange temperature is slightly lower than a bottom one. Such a gradient steel temperature distribution gives additional member deflections which can reach very considerable values. The separate, more precise discussion is necessary to study this effect; however, let us draw attention to one important fact: compression force $N_{c,\Theta}$ development in fire is the result of restraints of member thermal deformations; whereas, oppositely directed tension force $N_{t,\Theta}$ is activated as a consequence of simultaneous deflection growth. Paradoxically such a tension force reduces deflection from which it is induced. Theoretically it is even possible that $N_{t,\Theta} > \left| N_{c,\Theta} \right|$.
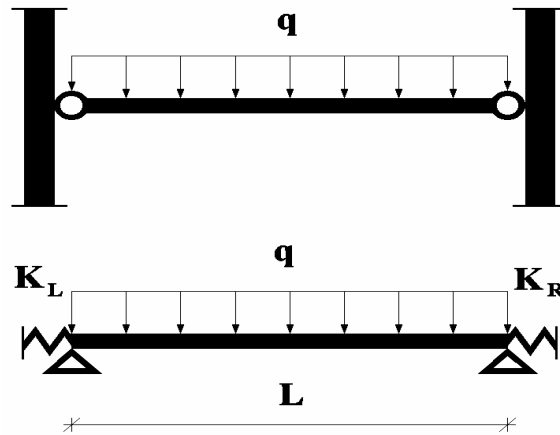

Figure 1. Multistory Frame Primary Beam Analysed in the Paper.

2.   GENERALIZED STABILITY FORMULA

In practical applications formulae relevant to member analysis in ambient temperature can also be applied when fully developed fire is taken into account, providing that reduced values of yield stress $f_{y,\Theta}$ and elasticity modulus E_{Θ} of steel are considered. This typical standard approach seems to be acceptable for the particular fire moments t_{fi} if member temperature $\Theta_a\left(t_{fi}\right)$ can be explicitly determined, because the value of compression force $N_{c,\Theta}$ can be then calculated on the basis of strain equilibrium condition. Both load bearing capacity and stability conditions are checked for particular t_{fi}, until the limit value $t_{fi,d}$, called member fire resistance, is found. Fire resistance limit state is reached if the most unfavourable design load effect $E_{i,d,\Theta}$, determined in accordance with accidental load combination rule, rises to the level of member load bearing capacity reduced in given steel temperature $R_{i,d,\Theta}$, in other words when

$$\rho_{i,\Theta} = E_{i,d,\Theta} \big/ R_{i,d,\Theta} = 1 \, .$$

At present one cannot definitely say that existing stability conditions relevant to beam-column analysis in ambient temperature, proposed by various authors, are verified enough. Complexity of the problem still generates intense and open discussion. The author prefers in this field the application of elastic-plastic stability formula which is based on the concept of moment equivalent $\beta_x M_x$ (Boissonnade et al. [2]), and is written in a form well known from German DIN 18800 and also Polish PN-90/B-03200 standards. The fully developed fire situation will be taken into account if such a formula is generalized (values dependent on steel temperature Θ_a are marked with the bottom index Θ):

$$\rho_{1,\Theta} = \frac{N_{c\Theta}}{\varphi_{x,\Theta} N_{Rc,\Theta}} + \frac{\beta_x M_{x,\Theta}}{\varphi_{L,\Theta} M_{Rx,\Theta}} + \Delta_{x,\Theta} \leq 1 \tag{1}$$

where:

$$\Delta_{x,\Theta} = \frac{N_{c,\Theta}}{N_{Rc,\Theta}} \left(1 - \frac{N_{c,\Theta}}{\varphi_{x,\Theta} N_{Rc,\Theta}} \right) \varphi_{x,\Theta}^2 \left(\overline{\lambda_{x,\Theta}} \right)^2 \approx 1{,}25 \varphi_{x,\Theta} \left(\overline{\lambda_{x,\Theta}} \right)^2 \frac{\beta_x M_{x,\Theta}}{M_{Rx,\Theta}} \frac{N_{c,\Theta}}{N_{Rc,\Theta}} \leq 0{,}1 \tag{2}$$

The left part of Eq. (2) origins from the German standard, whereas its right part from the Polish one.

Simple generalization of standard stability formulae leads to the assessments consistent with the results of numerical modelling (Valente [11], Vila Real et al. [12], Huang et al. [4], Yin et al. [14], Vila Real et al. [13]). They have also received separate confirmation in the experiment (Liu et al. [5]).

Two other inequalities are usually connected with Eq. (1). In case of $\beta_x < 1$ the $M - N_c$ interaction cross-section load bearing capacity $\rho_{2,\Theta}$ limitation can be crucial:

$$\rho_{2,\Theta} = \frac{N_{c,\Theta}}{N_{Rc,\Theta}} + \frac{M_{x,\Theta}}{\varphi_{L,\Theta} M_{Rx,\Theta}} \leq 1 \tag{3}$$

Moreover, the elimination of weak axis buckling ability is extremely important:

$$\rho_{3,\Theta} = \frac{N_{c,\Theta}}{\varphi_{y,\Theta} N_{Rc,\Theta}} \leq 1 \tag{4}$$

Eq. (1), Eq. (3) and Eq. (4) allow to find particular values of beam-column fire resistance, $t_{fi,d,1}$, $t_{fi,d,2}$ and $t_{fi,d,3}$, respectively. The smallest of these three means its conclusive value.

3.   MEMBER LOAD BEARING CAPACITY UNDER FIRE CONDITIONS

Coefficients $k_{y,\Theta}$ and $k_{E,\Theta}$ are commonly used as a measure of relative reduction of yield

stress f_y and elasticity modulus E, respectively. If the rule that partial safety factors remain constant in the whole of fire duration can be accepted, then we have ($\gamma_{cr} = 1{,}33$ is well known from PN-90/B-03200 partial safety factor for critical stresses):

$$f_{d,\Theta} = \frac{f_{y,\Theta}}{\gamma_M} = \frac{k_{y,\Theta} f_y}{\gamma_M} = k_{y,\Theta} f_d \qquad (5)$$

$$E_{d,\Theta} = \frac{E_\Theta}{\gamma_{cr}} = \frac{k_{E,\Theta} E}{\gamma_{cr}} = k_{E,\Theta} E_d \qquad (6)$$

Accurate determination of $k_{y,\Theta}$ and $k_{E,\Theta}$ values is not simple because of a great scatter of existing experimental results. Usually values proposed by EN 1993-1-2 standard are applied (table 1 and figure 2).

Table 1. Reduction Coefficients $k_{y,\Theta}$ and $k_{E,\Theta}$ According to EN 1993-1-2.

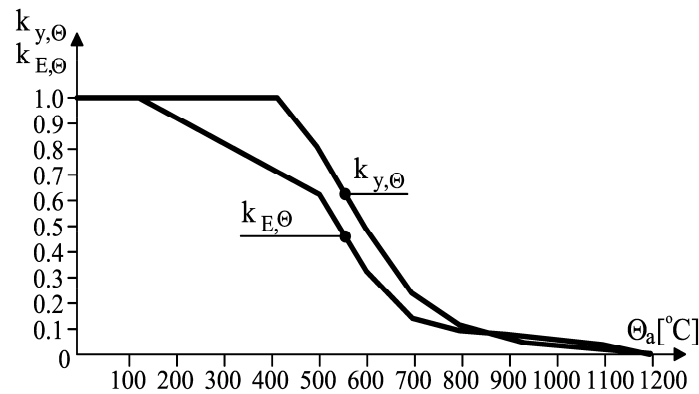| Θ_a [$^o C$]	$k_{y,\Theta}$	$k_{E,\Theta}$
≤ 100	1.00	1.00
200	1.00	0.90
300	1.00	0.80
400	1.00	0.70
500	0.78	0.60
600	0.47	0.31
700	0.23	0.13
800	0.11	0.09
900	0.06	0.0675
1000	0.04	0.045

Figure 2. Relative Reduction of Yield Stress and Elasticity Modulus of Steel Under Fire Conditions According to EN 1993-1-2.

On the other hand, in the Polish PN-90/B-03200 standard function relationships are recommended (figure 3):

$$k_{y,\Theta} = 1{,}022 - 0{,}197 \cdot 10^{-3} \Theta_a - 1{,}590 \cdot 10^{-6} \Theta_a^2 \qquad (7)$$

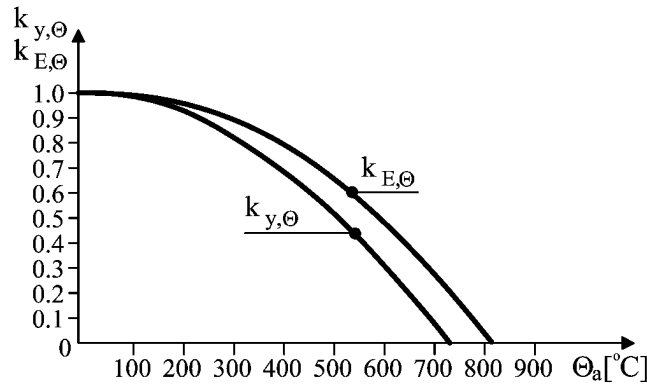$$k_{E,\Theta} = 0{,}987 + 0{,}300 \cdot 10^{-3}\,\Theta_a - 1{,}857 \cdot 10^{-6}\,\Theta_a^2 \tag{8}$$

Figure 3. Dependence between $k_{y,\Theta}$ and $k_{E,\Theta}$ Coefficients and

Steel Temperature Θ_a According to PN-90/B-03200.

In fact, values taken from table 1 are noticeable different than corresponding with them values received by solving Eq. (7) and Eq. (8). However, qualitative difference seems to be even more important. Careful attention should be paid to the fact that, according to EN 1993-1-2, if steel temperature Θ_a increases, elasticity modulus E_Θ decreases more quickly than yield stress $f_{y,\Theta}$; whereas, quite opposite conclusion is the result of application of PN-90/B-03200 rules (Eq. (7) and Eq. (8)).

Decrease of cross-section load bearing capacity in progressive member temperature if pure bending or axial compression occurs is identical to steel yield point reduction:

$$M_{Rx,\Theta} = W_{pl,x} f_{d,\Theta} = W_{pl,x} k_{y,\Theta} f_d = k_{y,\Theta} M_{Rx} \tag{9}$$

$$N_{Rc,\Theta} = A f_{d,\Theta} = A k_{y,\Theta} f_d = k_{y,\Theta} N_{Rc} \tag{10}$$

EN 1993-1-2 allows to adopt $\gamma_M = 1{,}0$ in accidental fire situation. It means that cross-section load bearing capacity can be determined on the stress level relevant to characteristic value of yield point f_y, so larger safety margin may be taken into account.

Global instability factors (both flexural buckling φ_Θ and lateral-torsional buckling $\varphi_{\Theta,L}$) depend on steel temperature in more complicated way. There are at least several commonly known methodologies to find their reliable values. The author recommends to do it by the use of the formula given by J. Murzewski (Murzewski [8]) which is applied in PN-90/B-03200:

$$\varphi_\Theta = \left(1 + \overline{\lambda_\Theta}^{2n}\right)^{-\frac{1}{n}} \tag{11}$$

where $n = 2{,}0; 1{,}6; 1{,}2$ is an imperfection parameter depending on buckling curve type: a, b and c, respectively. Structure of Eq. (11) is different than the form of Ayrton – Perry formula proposed in EN 1993-1-2; nevertheless, its usefulness to design process has been verified and confirmed many times (for instance Muzeau [10]).

According to EN 1993-1-2 in accidental fire situation the definition of non-dimensional slenderness $\overline{\lambda_\Theta}$ is revised (value of $\lambda_p = (\pi/1,15)\sqrt{E/f_d}$ the author suggests to calculate according to PN-90/B-03200, correcting in this way lack of coefficient $\gamma_{cr} = 1,33$ in European recommendations). In fact the acceptance of the concept:

$$\lambda_{p,\Theta} = \pi\sqrt{\frac{E_{d,\Theta}}{f_{d,\Theta}}} = \pi\sqrt{\frac{k_{E,\Theta}E_d}{k_{y,\Theta}f_d}} = \pi\sqrt{\frac{k_{E,\Theta}}{k_{y,\Theta}}}\sqrt{\frac{E}{\gamma_{cr}f_d}} = \frac{\pi\psi}{1,15}\sqrt{\frac{E}{f_d}} = \psi\lambda_p \tag{12}$$

leads to the formula:

$$\overline{\lambda_\Theta} = \frac{\lambda}{\lambda_{p,\Theta}} = \frac{\lambda}{\psi\lambda_p} = \frac{\overline{\lambda}}{\psi} \tag{13}$$

where $\psi = \sqrt{k_{E,\Theta}/k_{y,\Theta}}$.

Substitution of Eq. (13) to Eq. (11) gives:

$$\varphi_\Theta = \left(1 + \overline{\lambda_\Theta}^{-2n}\right)^{-\frac{1}{n}} = \left[1 + \left(\frac{\overline{\lambda}}{\psi}\right)^{2n}\right]^{-\frac{1}{n}} \tag{14}$$

Furthermore, considering the fact that according to EN 1993-1-2 instability factors are recommended to be determined if uniform imperfection parameter $\alpha = 0,65\sqrt{235/f_y}$ is assumed, the author, by analogy, suggests using in Eq. (14) always the c - type buckling curve (in other words $n = 1,2$), independently of the cross-section shape. It means that the value of φ_Θ should be calculated in this way even if the other buckling curve has been taken into consideration in persistent design situation. Consequently, the ratio $m_\Theta(\Theta_a) = \varphi_\Theta/\varphi$ which is the measure of relative reduction of buckling instability factor in fire, is dependent on the type of buckling curve (a, b or c) taken to stability analysis without any thermal effects. Dependence of m_Θ ratio on steel temperature Θ_a is shown in figure 4 (note that values of m_Θ are precisely calculated only for temperatures Θ_a presented in table 1; in case of the intermediate Θ_a values linear interpolation is applied).

In PN-90/B-03200 the alternative methodology to calculate buckling instability factor φ_Θ under fire conditions is proposed. Its value can be found directly from semi-empirical formula:

$$\varphi_\Theta = \left[1 + \left(\frac{1}{\varphi} - 1\right)\frac{E_d}{E_{d,\Theta}}\right]^{-1} = \left[1 + \left(\frac{1}{\varphi} - 1\right)\frac{E}{E_\Theta}\right]^{-1} = \left[1 + \left(\frac{1}{\varphi} - 1\right)\frac{1}{k_{E,\Theta}}\right]^{-1} \tag{15}$$

in which φ is an analogous instability factor but determined without thermal effects, in other

words, for non-dimensional slenderness $\bar{\lambda} = \lambda/\lambda_p$ where $\lambda_p = (\pi/1{,}15)\sqrt{E/f_d}$.
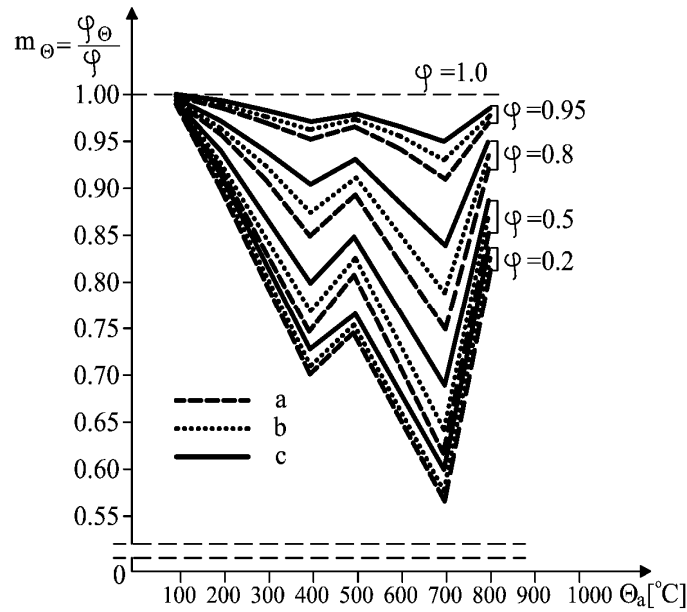

Figure 4. Relative Reduction $m_\Theta = \varphi_\Theta/\varphi$ of Buckling Instability Factor Under Fire Conditions According to EN 1993-1-2 Approach.

However, considering the fact that fire is an accidental design situation, the use of characteristic values of elasticity modulus $E_c = E/\gamma$ and $E_{c,\Theta} = k_{E,\Theta}\,E/\gamma = k_{E,\Theta}E_c$ seems to be more adequate (Maślak [7]). Then:

$$\varphi_{c,\Theta} = \left[1+\left(\frac{1}{\varphi_c}-1\right)\frac{E_c}{E_{c,\Theta}}\right]^{-1} = \left[1+\left(\frac{1}{\varphi_c}-1\right)\frac{E}{E_\Theta}\right]^{-1} = \left[1+\left(\frac{1}{\varphi_c}-1\right)\frac{1}{k_{E,\Theta}}\right]^{-1} \qquad (16)$$

Another partial safety factor for critical stresses γ, necessary to calculate characteristic value E_c, is applied in Eq. (16). Its value has not been shown in PN-90/B-03200, but in author's opinion the American recommendations in which value $\gamma = 1{,}14$ has been adopted may be helpful in this field, because value $\gamma_{cr} = 1{,}33$ is there also assumed. Moreover, careful attention should also be paid to the fact that the factor φ_c has to be now determined in relation to corrected non-dimensional slenderness $\bar{\lambda}_c = \lambda/\lambda_{p,c}$, where:

$$\lambda_{p,c} = \pi\sqrt{\frac{E_c}{f_y}} = \pi\sqrt{\frac{E}{\gamma f_y}} = \frac{\pi}{\sqrt{\gamma}}\sqrt{\frac{E}{f_y}} = \frac{\pi}{\sqrt{\gamma}}\sqrt{\frac{\gamma_{cr}E_d}{\gamma_M f_d}} = \frac{1{,}08}{\sqrt{\gamma_M}}\lambda_p \qquad (17)$$

Let us notice that values $\lambda_{p,c}$ and λ_p are equal each other only if $\gamma_M = 1{,}17$.

The ratio $m_{c,\Theta}(\Theta_a) = \varphi_{c,\Theta}/\varphi_c$ is adopted as the measure of relative reduction of defined in such a way buckling instability factor under fire condition. Dependence between it and steel temperature Θ_a is shown in figure 5.

Eq. (15) and Eq. (16) give slightly more conservative results than Eq. (14). However, the author

must underline the fact that both presented above methodologies to determine buckling instability factor under fire conditions are not compatible. Only values $k_{y,\Theta}$ and $k_{E,\Theta}$ originating from Eq. (7) and Eq. (8) can be substitute to Eq. (15) and Eq. (16) because all formulae in this approach have been calibrated especially for them. On the other hand, application of Eq. (14) leads to correct results only if data from table 1 are taken into consideration (let us notice that according to Eq. (7) and Eq. (8) $k_{y,\Theta} < k_{E,\Theta}$ which means that $\psi > 1$ in Eq. (14) so it is inconsistent with the intuition).
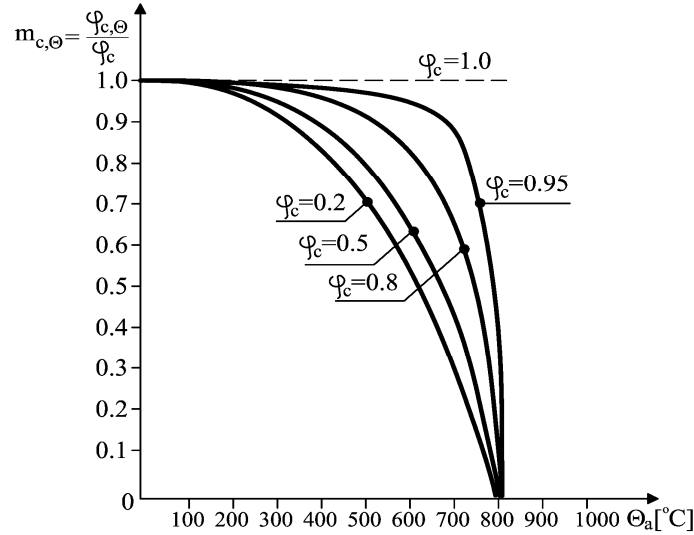

Figure 5. Relative Reduction $m_{c,\Theta} = \varphi_{c,\Theta}/\varphi_c$ of Buckling Instability Factor According to PN-90/B-03200.

Reminding one more approach proposed by J. Murzewski and M. Gwóźdź (Murzewski and Gwóźdź [9]) seems to be advisable in this place. They have postulated the application of elastic-plastic buckling theory. Such an analysis allowed them to generalize a typical formula proposed in PN-90/B-03200 for ambient temperature and persistent design situation:

$$\varphi_\Theta = \left(1 + \overline{\lambda}^{2n_\Theta}\right)^{-\frac{1}{n_\Theta}} \tag{18}$$

where:

$$n_\Theta = n\left(\frac{175}{\Theta_a}\right)^\alpha \tag{19}$$

Parameter n_Θ is here also an imperfection factor; however, it depends now on steel temperature. Values of an exponent α are collected in table 2 for the temperature interval $300\,^{o}C \leq \Theta_a \leq 600\,^{o}C$ and when buckling curves are determined by imperfection parameter n, identically as in typical stability analysis made in ambient temperature.

Table 2. Exponents α for Particular Buckling Curves (Murzewski, J. and Gwóźdź, M.)

Buckling curve	a	b	c
n (according to PN-90/B-03200)	2.0	1.6	1.2
α	0.56	0.44	0.30

The approach entirely similar to Eq. (12) may also be applied to determination of lateral-torsional buckling instability factor $\varphi_{L,\Theta}$. If the member cross-section is bisymmetrical and dependence between Poisson's ratio ν and steel temperature Θ_a can be neglected, then for the floor beam analysed in the example it is possible to show:

$$M_{cr,\Theta} = k_{E,\Theta} M_{cr} \tag{20}$$

which means that:

$$\overline{\lambda_{L,\Theta}} = 1,15 \sqrt{\frac{M_{R,\Theta}}{M_{cr,\Theta}}} = 1,15 \sqrt{\frac{k_{y,\Theta}}{k_{E,\Theta}}} \sqrt{\frac{M_R}{M_{cr}}} = \frac{\overline{\lambda_L}}{\psi} \tag{21}$$

The analysis of more complex examples of member lateral-torsional buckling phenomenon under fire conditions is widely discussed in the literature (for instance Lopes et al. [6]).

4.   THERMALLY INDUCED COMPRESSION FORCE

Beam total elongation δ when, under fire conditions, thermally induced compression force $N_{c,\Theta}$ is generated, depends on deformability of its supports on horizontal displacement $1/K$:

$$\delta = \frac{N_{c,\Theta}}{K} \tag{22}$$

Furthermore, it is the sum of unlimited beam thermal deformation δ_{Θ} (L means its span length, α_{Θ} coefficient of steel thermal expansion, $20^{o}C$ estimated temperature of beam erection):

$$\delta_{\Theta} = \alpha_{\Theta}(\Theta_a - 20)L \tag{23}$$

and mechanical strain δ_m which is the measure of supports reaction:

$$\delta_m = \frac{N_{c,\Theta}L}{E_{\Theta}A} \tag{24}$$

Value of compression force $N_{c,\Theta}$ can be obtained directly from the strain equilibrium condition. Because:

$$\delta_{\Theta} + \delta_m + \delta = 0 \tag{25}$$

hence:

$$N_{c,\Theta} = -\frac{\alpha_{\Theta}(\Theta_a - 20)E_{\Theta}A}{1 + \dfrac{E_{\Theta}A}{KL}} \tag{26}$$

Evaluation of such a thermally induced axial force allows to check the safety conditions given by Eq. (1), Eq. (3) and Eq. (4) and, consequently, to determine the member fire resistance $t_{fi,d}$. However, in most of cases it will be its quite conservative estimation. Let us notice that elastic-plastic buckling of the member as well as yielding of its most efficient cross-section can be considered as a beam-column failure modes only if they are associated with appropriately small member deflections. Such a requirement can be fulfilled under fire conditions when support deformability on horizontal displacement $1/K$ is small enough. Consequently, thermally induced compression force $N_{c,\Theta}$ is sufficient to generate the beam-column global instability very quickly. It should take place just in the beginning of fire, when the member temperature Θ_a is not yet very high and reduction of beam flexural stiffness is relatively little.

On the other hand, elastic-plastic buckling does not have to mean an ultimate beam-column collapse, but only rapid deflection growth accompanying a critical value of compression force. The behaviour of the member at large deflections is quite different from its behaviour at small deflections. Compression force $N_{c,\Theta}$ completely declines and oppositely directed tension force $N_{t,\Theta}$ is generated instead of it, as a result of beam shortening due to increasing deflection. This is the reason why plasticization of its most efficient cross-section does not occur, in spite of the fact that sudden deflection increment always induces simultaneous bending moment growth. Imposed loads are still carried because the beam works like transverse loaded tie-beam. Value of $N_{t,\Theta}$ is equal to the tie-beam tightening. This phenomenon is called a catenary effect (Allam et al. [1]). Such a post-critical beam behaviour during fire makes additional safety reserve; however, adequately large deflections, as a rule not to be tolerated, must be taken into consideration.

Let us assume that the total imposed load q calculated in accordance with accidental load combination rule is uniformly distributed, and y_0 means the tie-beam deflection (sag), then:

$$N_{t,\Theta} = \frac{M_{\max}}{y_0} = \frac{qL^2}{8y_0} \tag{27}$$

in other words:

$$y_0 = \frac{qL^2}{8N_{t,\Theta}} \tag{28}$$

The shape of a sagging tie-beam can be approximately described as a parabola with the length equal to:

$$s = L\left[1 + \frac{8}{3}\left(\frac{y_0}{L}\right)^2\right] = L + \Delta L \tag{29}$$

then its elongation is considered as:

$$\Delta L = \frac{8}{3}\frac{(y_0)^2}{L} \tag{30}$$

The value of tension force $N_{t,\Theta}$ may be determined, analogously like in case of $N_{c,\Theta}$, from strain equilibrium condition:

$$\alpha_\Theta (\Theta_a - 20)L + \frac{N_{t,\Theta}L}{E_\Theta A} + \frac{N_{t,\Theta}}{K} = \frac{8(y_0)^2}{3L} \tag{31}$$

Hence, after transformations, a root of a cubic equation should be found:

$$\left(N_{t,\Theta}\right)^3 \left(\frac{L}{E_\Theta A} + \frac{1}{K}\right) + \left(N_{t,\Theta}\right)^2 \alpha_\Theta (\Theta_a - 20)L - \frac{q^2 L^3}{24} = 0 \tag{32}$$

To sum up, an additional fourth safety condition (apart from Eq. (1), Eq. (3) and Eq. (4)), associated with beam rupture resulting from action of too strong tension force $N_{t,\Theta}$ is defined:

$$\rho_{4,\Theta} = \frac{N_{t,\Theta}}{N_{Rt,\Theta}} = \frac{N_{t,\Theta}}{A f_{d,\Theta}} \le 1 \tag{33}$$

The fact that such an additional beam load bearing capacity reserve exists in reality, even after complete exhaustion of all other possibilities for carrying loads imposed to the member in very high temperature, has also found the confirmation in the experiment (Allam et al. [1]).

The attention must be paid to the fact that both compression force $N_{c,\Theta}$ induced by the restraints of member thermal expansion, and tension one $N_{t,\Theta}$ which is the result of so called catenary effect should also be considered as an additional action applied to the columns bounding a beam analysed in the example. Let us notice that first of them generates the effect of column push out, on the contrary to the second one which is the source of column pull in effect. More precise structural analysis in which such thermally induced column loads are taken into account is given in the literature (Cai et al. [3]).

5.   NUMERICAL EXAMPLE

A numerical example presented below seems to be a good illustration of the methodology of fire resistance $t_{fi,d}$ evaluation developed in this paper.   Let the floor beam from figure 1 have a span length $L = 6,0$ m and cross-section IPE 300 ($h = 300$ mm, $b = 150$ mm, $A = 53,8$ cm^2, $W_{pl} = 2 \cdot 314,0 = 628,0$ cm^3) (see fig. 6). There is permanent load G as well as the only one variable load Q, both uniformly distributed. Their characteristic values are $G_k = 8,0$ kN/m, $Q_k = 12,0$ kN/m, respectively. The beam is made from S235JR steel grade with the following limited yield point values - design $f_d = 215$ MPa, and characteristic $f_k = 235$ MPa. Moreover, the member is protected against lateral-torsional buckling instability, because adjacent reinforced concrete floor slab can be considered as a fully rigid plate. Box type fire protected insulation made from mineral silicate composite plates with 12 mm thickness has been applied. Basic insulation parameters are as follows: density $\rho_p = 870$ kg/m^3, thermal conductivity $\lambda_p = 0,175$ W/(m·K), specific heat $c_p = 1200$ J/(kg·K). According to the specifications given by insulation producer, if

such parameters are chosen the required class of beam fire resistance R60 is warranted.

Beam is heated on three sides as it is presented in figure 6. The section factor value is equal to:
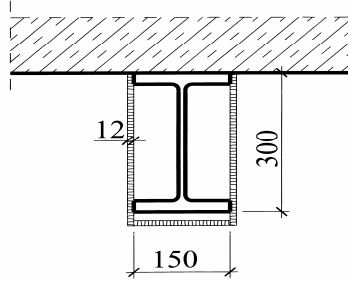$U/A = (2h + b)/A = 139,4 \ \text{m}^{-1}$.

Figure 6. Cross-section of Insulated Floor Beam Analysed in the Example.

Let us assume that $\gamma_G = 1,35$ and $\gamma_Q = 1,5$. The total load applied to the beam and summed in accordance with persistent load combination rule can be carried by the member before fire ignition and flashover occurs, since:

$M_{Sd} = (1,35 \cdot 8,0 + 1,5 \cdot 12,0) \cdot (6,0)^2 / 8 = 129,6 \ \text{kNm}$, $M_{Rd} = 628,0 \cdot 10^{-6} \cdot 215 \cdot 10^3 = 135,0 \ \text{kNm}$,

129,6 kNm < 135,0 kNm.

In accidental fire situation values $\gamma_{GA} = 1,0$ and $\psi_{11} = 0,5$ have been adopted, hence:

$q_{fi} = 1,0 \cdot 8,0 + 0,5 \cdot 12,0 = 14,0 \ \text{kN/m}$.

Cross-section load bearing capacity if pure bending as well as pure axial compression is taken into consideration ($\gamma_M = 1,0$ is assumed) may be calculated as:

$M_{Rx,\Theta} = 628,0 \cdot 10^{-6} \cdot 235 \cdot 10^3 = 147,6 \ \text{kNm}$,

$N_{Rc,\Theta} = 53,8 \cdot 10^{-4} \cdot 235 \cdot 10^3 = 1264,3 \ \text{kN}$.

It is accepted that gas temperature Θ_g increases in fire according to the standard fire curve. Furthermore, uniform member steel temperature Θ_a distribution is assumed, both across each beam cross-section and along the whole of its length. It means that the influence of more intensive top flange cooling process due to adjacent massive reinforced concrete floor slab is neglected. Values of Θ_a in particular fire times t_{fi} have been determined applying EN 1993-1-2 approach. Let us notice that after $t_{fi} = t_{fi,req} = 1\,\text{h}$ fire time period temperature Θ_a reaches value 666,8 ^oC (fig. 7). The basic safety requirement $t_{fi,d} > t_{fi,req}$ leads to the conclusion that the analysed steel beam should loose the ability to carry applied loads in temperatures higher than this one.

Values $k_{y,\Theta}$ and $k_{E,\Theta}$ for particular Θ_a have been adopted from table 1. Buckling instability factor φ_Θ has been calculated according to Eq. (14); moreover, value $\varphi_{L,\Theta} = 1,0$ has been accepted. Finally, compression force $N_{c,\Theta}$ values, taken from Eq. (26) for particular deformability parameters $1/K$, are presented in table 3. In addition, values of $N_{c,\Theta}$ if $\dfrac{1}{K} = 0$ ($K = \infty$) (in other words for fully restrained beam thermal elongation) have been separately shown

in table 4. Let us also notice that infinite deformability $\frac{1}{K} = \infty$, in other words $K = 0$, is an equivalent of the situation that one of beam supports has an ability of unlimited thermal elongation, hence $N_{c,\Theta} = 0$. Values of thermally induced tension force $N_{t,\Theta}$ are reasonable if steel temperatures Θ_a are high enough. For this reason they have been collected in table 5 only for $\Theta_a \geq 700~^{o}C$. Let us underline the fact that data from table 1 have also been applied in these calculations.
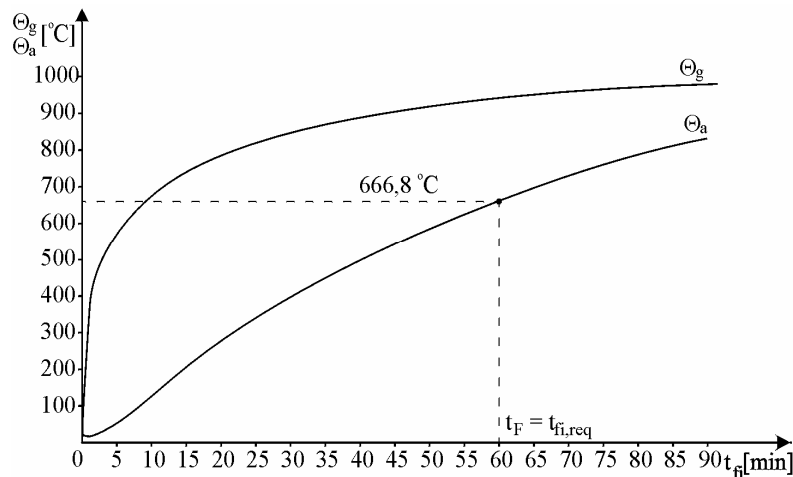

Figure 7. Temperature Growth in Analysed Insulated Floor Beam (According to EN 1993-1-2).

Table 3. Values of $N_{c,\Theta}$ $[kN]$ for particular deformability parameters $1/K$.

$\Theta_a \left[^{o}C \right]$	$K \left[kN/mm \right]$				
	0,2	1	5	10	50
100	1.2	5.7	11.4	54.6	103.9
300	4.0	20.0	39.8	188.8	354.9
400	5.5	27.2	53.9	253.9	473.6
500	6.9	34.3	67.9	316.9	585.1
600	8.3	41.0	80.7	355.3	618.2
700	9.7	47.0	90.4	345.2	533.1
800	11.1	53.0	100.2	350.0	508.5

Table 4. Values of $N_{c,\Theta}$ $[kN]$ if $\frac{1}{K} = 0$ is Adopted.

$\Theta_a \left[^{o}C \right]$	$N_{c,\Theta} \left[kN \right]$
20	0
30	132.3
40	264.6
50	397.0
60	529.3
70	661.6
80	793.9
90	926.3
100	1059.0

If the value of thermally activated force $N_{c,\Theta}$ is known for given member temperature Θ_a determination of specific safety levels is possible - $\rho_{1,\Theta}$ from Eq. (1), similarly $\rho_{2,\Theta}$ basing on Eq. (3) and $\rho_{3,\Theta}$ according to Eq. (4). Moreover, value of $\rho_{4,\Theta}$ can be identified if tension force $N_{t,\Theta}$ is taken from Eq. (33). Study of particular dependences $\rho_{i,\Theta} = \rho_i(\Theta_a)$ obtained from such the calculations and shown in succeeding figures 8, 9, 10 and 11 enables the designer to evaluate one decisive value of beam fire resistance $t_{fi,d}$. It means the smallest Θ_a value for which the level $\rho_i(\Theta_a) = 1,0$ is reached.

Table 5. Values of $N_{t,\Theta}$ $[kN]$ for Particular Deformability Parameters $1/K$.

$\Theta_a \left[{}^oC\right]$	$K\left[kN/mm\right]$				
	0,2	1	5	10	50
700	67,4	105,4	123,4	157,3	165,8
800	66,9	103,2	119,7	148,5	155,1

As it has been said before, in general the steel temperature increases together with fire development not only in analysed floor beam but also in columns bounding it. Then column flexural stiffness monotonically decreases. It means simultaneous growth of beam support deformability on horizontal displacement. For this reason real dependences $\rho_{i,\Theta} = \rho_i(\Theta_a)$ are more complicated than the ones shown in figures 8÷11, if such variability $1/K = 1/K(\Theta_a)$ is taken into account. Nevertheless, for particular fire moment t_{fi} only one definite value of deformability $1/K$ can always be reckoned. It allows to check all safety conditions Eq. (1), Eq. (3), Eq. (4) and Eq. (33) and, finally, to evaluate member fire resistance $t_{fi,d}$ in a conventional manner, described above.
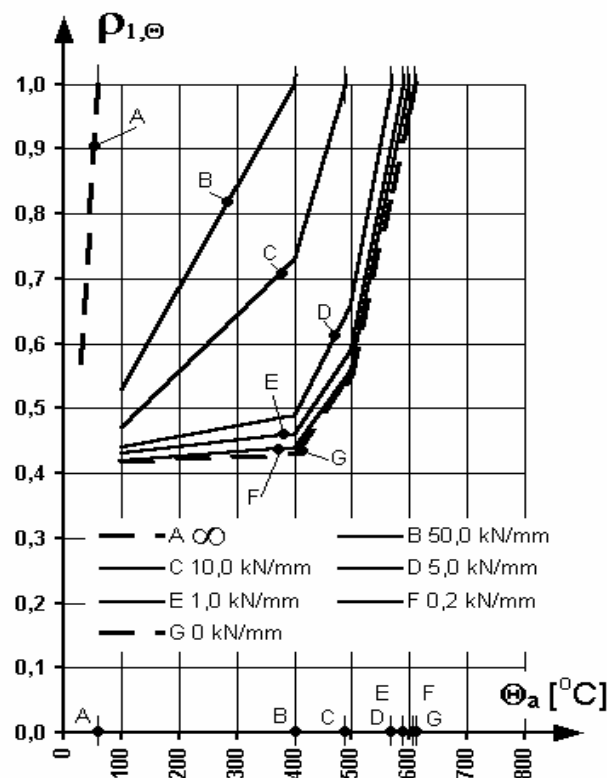

Figure 8. Fire resistance of Beam Analysed in the Example if Elastic-plastic Stability Condition Eq. (1) is Taken Into Account.
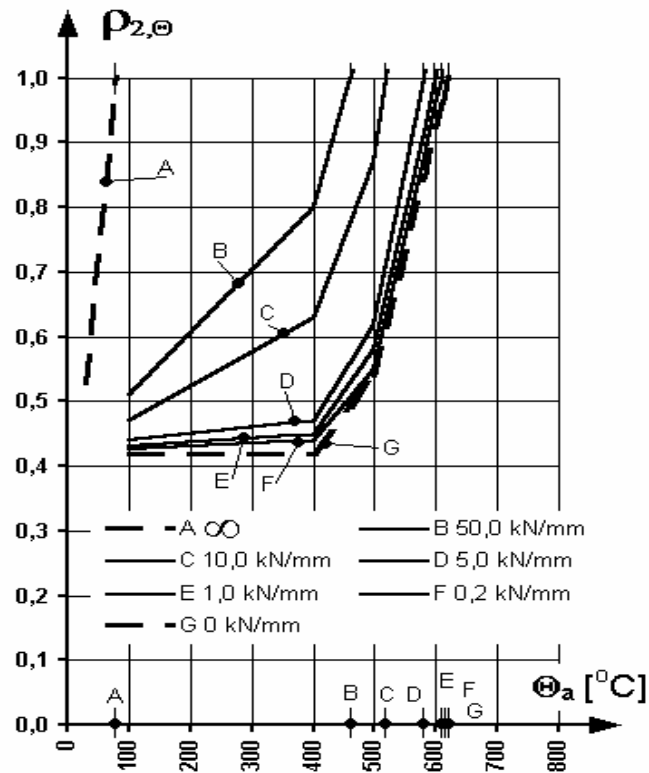
Figure 9. Fire Resistance of Beam Analysed in the Example, Received Basing on $M - N_c$ Interaction Cross-section Load Bearing Capacity Limitation, Eq. (2).
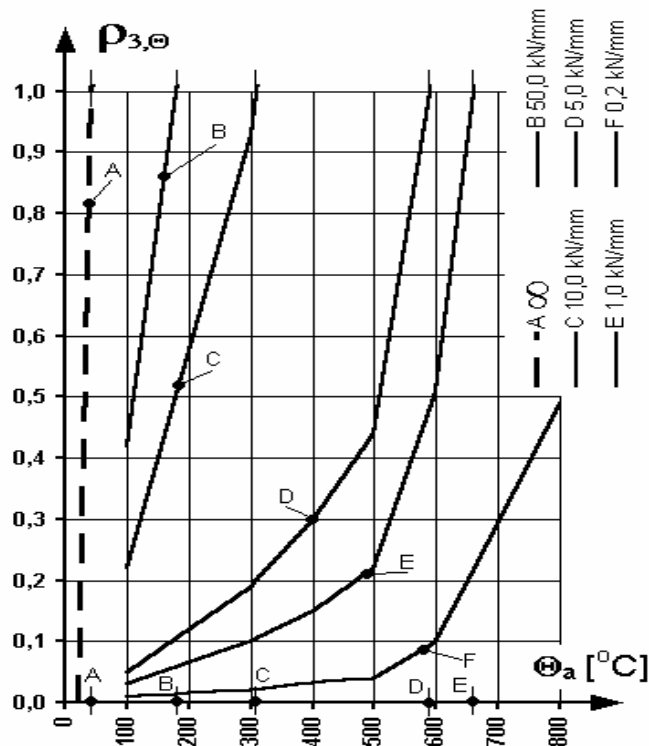

Figure 10. Fire Resistance of the Same Beam Derived Owing to Elimination of Ability of Weak Axis Buckling, Eq. (4).
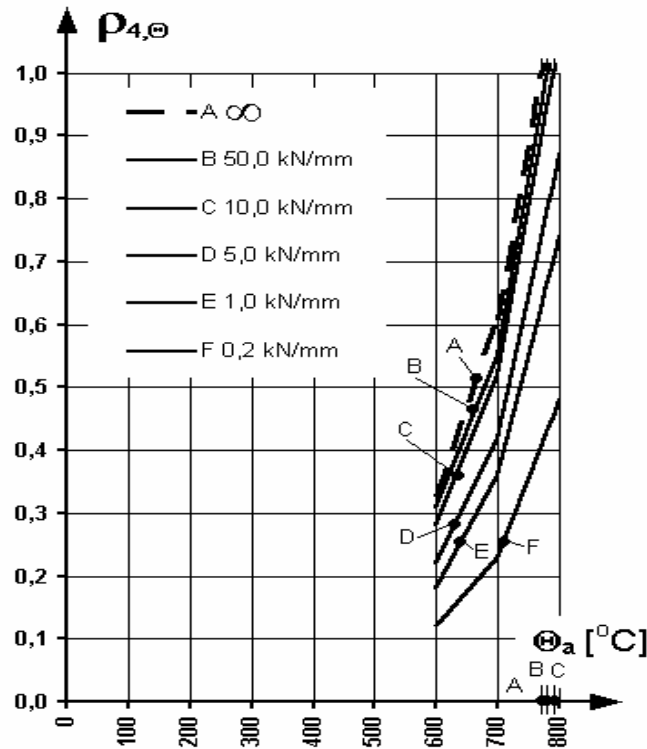
Figure 11. Fire Resistance of the Same Beam which is the Consequence of Attaining of Ultimate Tension Member Capacity, Eq. (33).

6.   CONCLUSIONS

Fire resistance of steel beam with restrained ability of thermal elongation has been assessed in this article as a minimum time value from the four results:
- the first one obtained on the ground of elastic-plastic stability condition (fig. 8),
- the second one received basing on $M - N_c$ interaction cross-section load bearing capacity limitation (fig. 9),
- the third one derived owing to elimination of ability of weak axis buckling (fig. 10),
- the fourth one being the consequence of attaining of ultimate tension member capacity (fig. 11).

Dependence between the restraints degree of the member prospective thermal deformations, and real value of its fire resistance, has been studied above all. Such an influence has been expressed by the parameter of beam support deformability on horizontal displacement $1/K$.

If assumed deformability is small enough $(K \geq 5\,\text{kN/mm})$, compression force $N_{c,\Theta}$ of a considerable value is induced and safety condition Eq. (4) becomes decisive. In case of a great deformability, thermally induced force $N_{c,\Theta}$ is weak enough and condition Eq. (1) is crucial. Safety condition Eq. (3) is always softer than Eq. (1), because an equivalent bending moment equal to $\beta_x M_x = M_x$ results from assumptions accepted in the example. Ultimate tension member capacity is not reached before steel temperatures exceed $760\ ^{\text{o}}C$ (see Eq. (33)). Particular critical steel temperatures $\Theta_{a,cr} = \Theta_a \left(t_{fi,d} \right)$ obtained in the example for various deformability parameters $1/K$ create a large domain, from nearly $40\ ^{\text{o}}C$ for condition Eq. (4) and fully

restrained beam elongation $(K = \infty)$ (broken line A in fig. 10), to about $620 \ ^oC$ if condition Eq. (1) and infinite deformability $(K = 0)$ are taken into account (broken line G in fig. 8).

In conclusion, careful attention should be paid to the fact that such critical temperatures $\Theta_{a,cr}$ are always significantly lower than $\Theta_a\left(t_{fi,req}\right) = 666,8 \ ^oC$. It means that basic safety requirement $t_{fi,d} > t_{fi,req}$ is not fulfilled. These results demonstrate that the designer's belief that she/he will secure (without any additional structural analysis) safe and failure-free member working under fire conditions during at least required time $t_{fi,req}$ (in the above example one hour), if fire develops identically as the standard fire model, and fire protected insulation is chosen directly from producer specifications, is completely unjustified. In particular, beam protected in this way and analysed in the example could be buckled just after a few minutes of fire if flexural stiffness of columns bounding the beam is large enough.

The catenary action of restrained steel beams comes into effect only when the beam deflection has been evidently developed. Consequently, the tension rupture failure mode of such beams takes place always behind the other failure domains (due to instability and yielding of cross-section). Considering the yielding of cross-section is not crucial for fire resistance evaluation of restrained steel beams, it is suggested that the global instability criterion should be used always if the beam deflection needs to be limited. On the other hand, the tension rupture criterion can be used only if such a deflection does not need to be limited.

The study presented above shows absolute necessity to make separate thermal and structural analysis always if the parameters of fire protected insulation are chosen. Firstly, thermal field $\Theta_a\left(t_{fi}\right)$ in every member of load bearing structure should be obtained for particular fire scenario. Secondly, values of all thermally induced internal forces and moments, as well as the possible ways of their redistribution, should be calculated and discussed for given fire moments t_{fi}. Finally, determination of critical temperature $\Theta_{a,cr} = \Theta_a\left(t_{fi,d}\right)$ which is a measure of member fire resistance is necessary, for instance in the simplified way presented in this article. Member fire resistance $t_{fi,d}$ seems to be an appropriate measure giving the designer an opportunity to choose the parameters of fire insulation in optimal and easy way. Simply, its adopted kind will be satisfactory only if critical steel temperature $\Theta_{a,cr}$ is reached in each structural member later than $t_{fi,req}$ occurs.

In the presented example, the analysis of only one single member isolated from the whole of load bearing structure has been quite sufficient to reliably evaluate its fire resistance $t_{fi,d}$. However, in general complexity of possible interactions between all external as well as thermally induced actions leads to the conclusion that such a simple study can be insufficient. For this reason more complete research, basing on the analysis of the whole structure or at least its suitable substructure is recommended to perform always if possible.

Finally, it is necessary to say that all results obtained on the ground of the methodology discussed in this paper can be interpreted only as an approximation of real values. In high temperatures, especially higher than $400 \ ^oC$, creep of steel becomes considerably influential. A more precise analysis in which rheological effects are taken into account requires appropriate computer modelling.

REFERENCES

[1]   Allam, A.M., Burgess, I.W. and Plank, R.J., "Performance-based Simplified Model for a Steel Beam at Large Deflection in Fire", Proceedings of 4th International Conference "Performance-based Codes and Fire Safety Design Methods", 2002, Melbourne, Australia.

[2]   Boissonnade, N., Jaspart, J-P., Muzeau, J-P. and Vilette, M., "New Interaction Formulae for Beam-columns in Eurocode 3: The French-Belgian Approach", Proceedings of 3rd European Conference on Steel Structures "Eurosteel 2002", September 19-20 2002, Coimbra, Portugal.

[3]   Cai, J., Burgess, I.W. and Plank, R.J., "The Effect of Push-out of Perimeter Building Columns of Their Survival in Fire", Proceedings of International Conference "Steel Structures of the 2000's, 2002, Istanbul, Turkey.

[4]   Huang, Z., Burgess, I.W. and Plank, R.J., "3D Modelling of Beam-columns with General Cross-sections in Fire", Proceedings of 3rd International Workshop "Structures in Fire", 2004, Ottawa, Canada.

[5]   Liu, T.C.H., Fahad, M.K. and Davies, J.M., "Experimental Investigation of Behaviour of Axially Restrained Steel Beams in Fire", Journal of Constructional Steel Research, 2002, Vol. 58.

[6]   Lopes, N., Simões da Silva, L., Vila Real, P.M.M. and Piloto, P., "New Proposals for the Design of Steel Beam-columns in Case of Fire Including a New Approach for the Lateral-torsional Buckling, Computer and Structures, 2004, Vol. 82.

[7]   Maślak, M., "Fire Resistance of Steel Beam-columns", Proceedings of 11th International Conference on Metal Structures "Progress in Steel, Composite and Aluminium Structures, 2006, Rzeszów, Poland.

[8]   Murzewski, J., "Columns and Beam-columns", Proceedings of 2nd Regional Colloquium of Steel Structures, 1986, Budapest, Hungary.

[9]   Murzewski, J., Gwóźdź, M., "Resistance of Steel Columns in Fire Temperatures", Proceedings of 37th Scientific Conference, 1991, Krynica, Poland, Vol. 4.

[10] Muzeau, J-P., "Reliability of Steel Columns. Study of the Polish Standard Code", Proceedings of 34th Scientific Conference, 1988, Krynica, Poland, Vol. 3.

[11] Valente, J.C., "Fire Resistance of Steel Columns with Elastically Restrained Axial Elongation and Bending", Journal of Constructional Steel Research, 1999, Vol. 52.

[12] Vila Real, P.M.M., Lopes, N., Simões da Silva, L., Piloto, P. and Franssen, J-M., "Towards a Consistant Safety Format of Steel Beam-columns: Application of the New Interaction Formulae for Ambient Temperature to Elevated Temperatures", Steel & Composite Structures, 2003, Vol. 3, No. 6.

[13] Vila Real, P.M.M., Lopes, N., Simões da Silva, L., Piloto, P. and Franssen, J-M., "Numerical Modelling of Steel Beam-columns in Case of Fire – Comparison with Eurocode 3, Fire Safety Journal, 2004, Vol. 39.

[14] Yin, Y.Z. and Wang, Y.C., "A Numerical Study of Large Deflection Behaviour of Restrained Steel Beams at Elevated Temperatures", Journal of Constructional Steel Research, 2004, Vol. 60.

[15] DIN 18800, Stahlbauten, Bemessung und Konstruktion, Part 1 & 2.

[16] EN 1993-1-2, Eurocode 3: Design of Steel Structures, Part 1-2: General Rules – Structural Fire Design.

[17] PN-90/B-03200, Steel Structures, Design rules.